INVESTIGATION OF FRACTURE TOUGHNESS ON FLATTENED
BRAZILIAN DISC TYPE MOLDED SHOTCRETE SPECIMENS

A THESIS SUBMITTED TO
THE GRADUATE SCHOOL OF NATURAL AND APPLIED SCIENCES
OF
MIDDLE EAST TECHNICAL UNIVERSITY

BY

SELIN YONCACI

IN PARTIAL FULFILLMENT OF THE REQUIREMENTS
FOR
THE DEGREE OF DOCTOR OF PHILOSOPHY
IN
MINING ENGINEERING

SEPTEMBER 2019

Approval of the thesis:

INVESTIGATION OF FRACTURE TOUGHNESS ON FLATTENED BRAZILIAN DISC TYPE MOLDED SHOTCRETE SPECIMENS

submitted by **SELIN YONCACI** in partial fulfillment of the requirements for the degree of **Doctor of Philosophy in Mining Engineering Department, Middle East Technical University** by,

Prof. Dr. Halil Kalıpçılar
Dean, Graduate School of **Natural and Applied Sciences**   _____

Prof. Dr. Celal Karpuz
Head of Department, **Mining Engineering**   _____

Prof. Dr. Levend Tutluoğlu
Supervisor, **Mining Engineering, METU**   _____

Examining Committee Members:

Prof. Dr. Celal Karpuz
Mining Engineering Dept., Middle East Technical University   _____

Prof. Dr. Levend Tutluoğlu
Mining Engineering, METU   _____

Prof. Dr. Bahtiyar Ünver
Mining Engineering Dept., Hacettepe University   _____

Prof. Dr. Hasan Öztürk
Mining Engineering Dept, Middle East Technical University   _____

Assoc. Prof. Dr. Mehmet Ali Hindistan
Mining Engineering Dept., Hacettepe University   _____

Date: 06.09.2019

I hereby declare that all information in this document has been obtained and presented in accordance with academic rules and ethical conduct. I also declare that, as required by these rules and conduct, I have fully cited and referenced all material and results that are not original to this work.

Name, Surname: Selin Yoncacı

Signature:

ABSTRACT

INVESTIGATION OF FRACTURE TOUGHNESS ON FLATTENED BRAZILIAN DISC TYPE MOLDED SHOTCRETE SPECIMENS

Yoncacı, Selin
Doctor of Philosophy, Mining Engineering
Supervisor: Prof. Dr. Levend Tutluoğlu

September 2019, 167 pages

Monitoring behavior of cracks generated by various reasons in shotcrete/concrete is of crucial importance for the stability of structures in various industries. Despite the need of understanding the crack initiation and propagation mechanisms profoundly, fracture mechanics related studies for shotcrete are limited so far. This topic has not attracted the attention it deserves in structural applications such as tunneling.

Beam type specimen geometries are commonly used in fracture mechanics testing of shotcrete/concrete mixtures, since building columns, beams, and tunnel linings are under bending loads in general. However, compressive loads in structures can indirectly induce tensile splitting, that's why, Brazilian type splitting tests are common in checking the structural state of columns, beams, and the linings. A different geometry, Flattened Brazilian Disc geometry (FBD), is used here for the first time for fracture testing of the shotcrete samples.

Targeted FBD sample diameters were up to 200 mm. Preparing samples with regular coring and grinding process were not practical due to irregularities formed during machining of samples. Innovative technologies were used to prepare FBD samples with different dimensions 3D printer technology was used to shape the sample molds to the desired geometries. As the molds were printed with a 3D printer, the sample

preparation process was improved. The diameter and the loading angle controlling the length of the flattened end was accurately adjusted for each size group.

Shotcrete mixture poured to the molds was prepared carefully to maintain the granular and binding characteristic as the sample size increased. Aggregate size was around 0-5 mm in the mixture. Water/cement ratio was selected as 0.40.

A total of 16 molds were used to obtain the samples with diameters range from 75 mm to 200 mm. Loading angles varied between 20-30 degrees, corresponding to flattened end lengths of $2L$= 15.6-43.5 mm.

A total of 80 valid mode I fracture tests were conducted. Some test results were discarded, since a clear load drop or a theoretically desired central splitting of samples were not observed. It was assured that there were five valid tests for each diameter group and each loading angle group regarding a specific diameter.

With the help of a proposed equation from a previous numerical modeling work, the initial crack length (a_{cn}) at the onset of stable fracturing was calculated. This was compared to the experimentally observed a_{ce} during the slow pace loading of FBD specimens. The previous theoretical formula was validated and proved to be applicable for the shotcrete FBD testing.

It was found that mode I fracture toughness, K_{Ic}, increased with increasing specimen diameter. It was found 0.96 MPa√m for the lowest diameter group of 75 mm with 30° loading angle, and it was 1.50 MPa√m for the largest diameter group of 200 mm with a loading angle of 20°.

In general, K_{Ic} is found to decrease with increasing loading angle. This situation is attributed to the boundary influence issue, since the flattened end length L increases compared to the specimen size. Compressively loaded ends and adjacent stress free boundary get too close to the crack front, which is supposed to be under pure mode I loading state. High stress gradients cause a complex loading state instead.

Increase of K_{Ic} with size and decreasing loading angle showed clues of a second degree polynomial tendency to a size- and geometry-independent ideal specimen for pure mode I fracture toughness testing of shotcrete with FBD geometry. FBD testing work here provided important results and proved its high potential to develop an ideal testing geometry to measure pure mode I fracture toughness of shotcrete/concrete materials.

ÖZ

KALIPLI DÜZLEŞTİRİLMİŞ BRAZİLYAN DİSK TİPİ PÜSKÜRTME BETON NUMUNELERİNDE KIRILMA TOKLUĞUNUN İNCELENMESİ

Yoncacı, Selin
Doktora, Maden Mühendisliği
Tez Danışmanı: Prof. Dr. Levend Tutluoğlu

Eylül 2019, 167 sayfa

Püskürtme beton ve/veya betonlarda çeşitli nedenlerden kaynaklanan çatlakların incelenmesi çeşitli endüstrilerdeki yapıların kararlılığı için çok önemlidir. Çatlak başlangıcı ve ilerlemesi konularının derinlemesine incelenmesi gerekliliğine rağmen, püskürtme beton konusundaki kırılma mekaniği ile ilgili çalışmalar şu ana kadar sınırlı kalmıştır. Bu duruma rağmen beton numuneleri üzerinde yapılmış olan çatlak mekaniği araştırmaları bugüne kadar sınırlı kalmış olup bu konu, tüneller gibi yapısal uygulamalarda hak ettiği ilgiyi çekmemiştir.

Yapı sütunların, kirişlerin ve tünel kaplamalarının genel olarak eğilme yükü altında olmaları nedeniyle, kiriş tipi numune geometrisi, püskürtme beton ve/veya beton numunelerinde yapılan çatlak mekaniği testlerinde yaygın olarak kullanılmaktadır. Bununla birlikte, yapılardaki basınç yükleri indirek olarak yarmada çekme bölünmesine neden olabilmekte, bu nedenle, Brazilyan tipi yarma testleri sütunların, kirişlerin ve kaplamaların yapısal durumunu kontrol etme konusunda daha yaygındır. Farklı bir geometri olan Düzleştirilmiş Brazilyan Disk (FBD) geometrisi kırılma mekaniği testlerinde ilk kez bu çalışmada kullanılmıştır.

Hedeflenen en büyük FBD geometrisine sahip numune çapı 200 mm'dir. Numunelerin hazırlanması sırasında oluşan sıkıntılar nedeniyle karot alma ve düzeltme işlemleri

numunelerin hazırlanması için uygun olmamıştır. Farklı boyutlarda FBD numuneleri hazırlamak için yenilikçi teknolojiler kullanılmış, 3B yazıcı teknolojisi ile numune kalıpları hazırlanmıştır. 3B yazıcıdan elde edilen kalıplar sayesinde numune hazırlama süreci iyileştirilmiştir. Düzleştirilmiş kenarın boyutunu kontrol eden çap ve yükleme açısı her boyut grubu için kalıplar sayesinde ideal şekilde ayarlanmıştır.

Kalıplara dökülen püskürtme beton karışımı, numune boyutu arttıkça granül ve bağlayıcı karakteristiğini korumak için dikkatlice hazırlanmıştır. Bu nedelen karışımdaki agrega boyutları yaklaşık olarak 0-5 mm, su/çimento oranı ise 0,40 olarak seçilmiştir.

Çapları 75 mm ile 200 mm arasında değişen numuneleri elde etmek için toplamda 16 kalıp kullanılmıştır. Kalıpların yükleme açıları 20-30 derece arasında değişmekte olup, düzleştirilmiş kenarların boyutları ise 2L = 15.6-43.5 mm arasında değişmektedir.

Toplamda 80 geçerli mod I kırılma testi gerçekleştirilmiştir. Net bir yük düşüşü veya teorik olarak istenilen şekilde numunenin tam merkezinden ikiye bölünmesinin gözlenmediği durumlardaki test sonuçları çıkartılmıştır. Her bir çap grubu ve her bir yükleme açısı grubu için beş geçerli test yapılmasına önem verilmiştir.

Daha önceden yapılmış olan sayısal modelleme çalışmasında önerilen denklemler yardımıyla, stabil kırılma anındaki başlangıç çatlak uzunluğu (a_{cn}) hesaplanmıştır. Bu değer, FBD örneklerinin yavaş hızda deneye tabii tutulması esnasında deneysel olarak gözlemlenen a_{ce} ile karşılaştırılmıştır. Önceki çalışmalarda sadece teorik olarak bulunan formüllerin geçerliliği deneyler yardımıyla kanıtlanarak, bu formüllerin FBD geometrisine sahip püskürtme beton numuneleri için uygulanabilir olduğu kanıtlanmıştır.

Mod I kırılma tokluğunun (K_{Ic}) artan numune çapı ile arttığı bulunmuştur. Mod I kırılma tokluğu değeri 30° yükleme açısına sahip 75 mm'lik en düşük çaplı grup için 0.96 MPa√m, 20°'lik yükleme açısına sahip 200 mm'lik en büyük çap grubu için 1.50 MPa√m bulunmuştur.

Genel olarak, K_{Ic} değerinin artan yükleme açısı ile azaldığı tespit edilmiştir. Düzleştirilmiş kenar uzunluğu L, numune boyutuna kıyasla arttığından, bu durum sınır etkisi sorunu yaratmaktadır. Yüke maruz kalan bu kenarlar ve etrafındaki gerilmesiz sınır, saf mod I yükleme durumunda olduğu varsayılan çatlak üzerine çok yaklaşır. Bu durumda oluşan yüksek gerilmeler karmaşık bir yükleme durumuna neden olur.

K_{Ic} değerinin boyut ve azalan yükleme açısı ile artması, saf mod I kırılma tokluğu testi uygulanan FBD geometrisine sahip püskürtme beton için ikinci derece polinom trendi göstermiştir. Burada sunulan FBD test çalışmaları önemli sonuçlar vermiş olup, FBD geometrisinin püskürtme beton ve/veya beton numunelerinin saf mod I kırılma tokluğunu ölçmek için ideal bir test geometrisi olabileceğini kanıtlamıştır.

Anahtar Kelimeler: Mod I Çatlak Tokluğu, Düzleştirilmiş Brazilyan Disk Yöntemi, Kalıplı Püskürtme Beton, Kırılma Testleri, Boyut Etkisi

To my family

ACKNOWLEDGEMENTS

TABLE OF CONTENTS

LIST OF TABLES

LIST OF FIGURES

FIGURES

xxiii

LIST OF ABBREVIATIONS

ABBREVIATIONS

3D	:	Three-dimensional
BD	:	Brazilian disc
BDT	:	Brazilian disc test
CB	:	Chevron bend
CCNBD	:	Cracked chevron notched Brazilian disc
CNSCB	:	Chevron notched semi-circular bending
CSTBD	:	Cracked straight through Brazilian disc
DC	:	Diametric compression
EPFM	:	Elastic Plastic Fracture Mechanics
FBD	:	Flattened Brazilian disc
FPZ	:	Fracture process zone
HCFBD	:	Hole-cracked flattened Brazilian disc
ISRM	:	International Society for Rock Mechanics and Rock Engineering
LEFM	:	Linear Elastic Fracture Mechanics
MR	:	Modified ring
OPC	:	Ordinary Portland cement
SCB	:	Semi-circular bending
SECRBB	:	Straight edge cracked round bar bend
SIF	:	Stress intensity factor
SR	:	Short rod
TCMA	:	Turkish Cement Manufacturers Association
UCS	:	Uniaxial compressive strength

LIST OF SYMBOLS

SYMBOLS

a	:	half of crack length
a_{ce}	:	experimentally found initial crack length
a_{cn}	:	numerically calculated initial crack length
a_{cn}/R	:	dimensionless crack length
B	:	empirical constant related with the dimension
d_e	:	distance of crack tip to central load application point
d_{max}	:	maximum aggregate grain size
D	:	disc diameter
$\boldsymbol{D}$	:	characteristic dimension of the specimen
D_o	:	empirical coefficient showing the transition between brittle and non-brittle behavior
E	:	Young's Modulus (or Modulus of Elasticity)
ft	:	tensile strength of concrete
G	:	energy release rate
G_c	:	critical energy release rate
H	:	height of the specimen
K	:	stress intensity factor
K_c	:	fracture toughness
K_I	:	mode I stress intensity factor
K_{Ic}	:	mode I fracture toughness
K_{II}	:	mode II stress intensity factor
K_{III}	:	mode III stress intensity factor
L	:	half of flattened length
$2L$	:	flattened length
M	:	mass

P	:	applied concentrated load
P_{min}	:	minimum local load
R	:	disc radius
t	:	disc thickness
t/R	:	thickness/ratio
t_d	:	curing time
t_m	:	wall thickness of the mold
w	:	specimen width
Y	:	dimension and geometry dependent constant
Y_I	:	mode I dimensionless stress intensity factor
Y_{Imax}	:	maximum mode I dimensionless stress intensity factor
υ	:	Poisson's ratio
σ	:	applied stress
σ_c	:	Uniaxial Compressive Strength
σ_{axial}	:	axial stress
ε_{axial}	:	axial strain
$\varepsilon_{lateral}$	:	lateral strain
σ_t	:	tensile strength
α	:	loading angle
τ	:	shear stress
r	:	radius of specimen
θ	:	crack propagation angle
μ	:	shear modulus
ρ	:	density
σ_N	:	nominal strength at failure
β	:	brittleness number
$\Delta\sigma_a$	:	applied stress/flattened area
ΔP	:	$P_{max}-P_{min}$

CHAPTER 1

INTRODUCTION

Underground support systems are frequently used in mining and construction projects aiming to improve stability and maintaining the strength of surrounding rock. According to the specified purpose of the project, these support systems are commonly classified as permanent and temporary. One of the most commonly applied temporary support systems in underground openings and tunnels is shotcrete. Shotcrete is generally prepared on site and applied at the moment of preparation. This feature of shotcrete limits the number of detailed laboratory studies in this field. Understanding the mechanical behavior of shotcrete is crucial due to its common usage in the underground mining operations for the exploitation of deep mineral deposits and coal reserves (Widijanto, et al. 2010) (Lemay, Jolin and Gagne, 2014) (Drover and Villaescusa, 2015). Fracturing mechanisms and fracture toughness of individual support units can be significant, especially for deep mines and tunnels in squeezing ground. The number of underground mining operations will continue to increase and the on-going development of infrastructure projects makes the investigation of the mechanical properties of shotcrete an essential research field in rock mechanics.

1.1. General Remarks

The available literature in this field focuses on the determination of basic mechanical properties of shotcrete by performing laboratory testing of specimens. However, one of the most important weaknesses of shotcrete are cracks (Lackner and Mang, 2001). For this reason, it will be useful to investigate the fracture mechanism of shotcrete and to understand the crack behavior completely. This behavior is usually studied within the scope of construction projects. However, the crack behavior of shotcrete has not

been widely investigated in the field of mining where shotcrete is frequently used as a support system.

1.2. Statement of the Problem

Research on shotcrete is still in progress covering various concepts and applications in both mining and civil engineering fields. Although certain topics, such as rebound time and mechanical strength are prioritized, the investigation of fracture characteristics of shotcrete to understand its mechanical behavior should be considered as one of the primary research area in this field due to its relation to crack formation.

The parameters of fracture mechanics for shotcrete, which is an important part of underground support systems, have not been studied entirely before. For brittle materials, the essential failure mode is Mode I because the primary weakness of these materials is their tension behavior. So it is particularly useful to find the Mode I fracture toughness value for shotcrete. In this study, Flattened Brazilian Disc (FBD) method, one of the most applicable methods for mode I evaluation, was used for the first time. In addition, the optimum specimen geometry suitable for the FBD method was studied for the first time on shotcrete samples.

There are some suggested methods for calculating the Mode I fracture toughness suggested by International Society for Rock Mechanics and Rock Engineering (ISRM). Although these methods are suitable for rock material, they are not very suitable or sufficient for the application of shotcrete. The procedures of sample preparation in the ISRM suggested methods and alternative methods in literature are mostly classified as laborious and difficult process. Prepared samples of these suggested methods cannot even be said to be absolutely appropriate, also it is known that most of the invalid experiments are caused by minor problems in sample preparation. These situations force users to search for easy and user-friendly methods.

In previous analyses conducted by using FBD method, the specimen dimensions were always limited. The method, analyzed in a wide range by numerical analysis, is unable

to capture this wide range in laboratory experiments and cannot validate the numerical results. However, it is very important to analyze samples of different sizes to prove the suitability and validity of the numerical analysis results.

Size effect has been frequently investigated by well-known methods in fracture related studies, especially in research about concrete. Laboratory tests involving concrete/shotcrete casting processes are considerably labor-intensive compared to tests conducted on rock specimen. Studies on the size effect in the rock specimen are commonly limited by the diameter of the available laboratory type core drill in case blocks are used for sample preparation. Therefore, innovative approaches are becoming increasingly important in mechanical laboratory experiments.

1.3. Objectives of the Study

It is essential to ensure the quality and performance of material used for supporting systems in mining and tunneling activities by a confirmation meeting the requirements. In recent years, the mining industry has become a major user of shotcrete for underground applications. Support systems are an important area of shotcrete application in underground mining systems. Therefore, one of the most important issues of underground support systems is the accurate estimation of mechanical and fractural properties of the material used.

The overall aim of the study is to assess the fracture behaviour and determine Mode I fracture toughness of shotcrete and this assessment are conducted with the Flattened Brazilian Disc (FBD) type shotcrete specimen. The main objective of this study is not only investigating the size effects on FBD type shotcrete specimen with different dimensions but also determining the optimum specimen dimensions for Mode I fracture toughness.

The objective of this thesis is to investigate the fracture behavior and size effect in FBD type shotcrete specimen by several fracture toughness related laboratory tests. The laboratory tests on shotcrete specimen with different dimensions can be considered as challenging to conduct on-site due to sample preparation. A main

contribution is to find the optimum dimension of shotcrete specimen for researchers by investigating the difference of fracture behavior between samples having different dimensions. One of the objectives of the study is to keep the range of sample sizes as wide as possible and to obtain samples having larger dimension than those used in the literature.

In addition, the potential of 3D printing technology for the production of specimen molds used in concrete specimen preparation on laboratory scale was also considered as an objective of the study. Because the sample preparation process of methods used to find Mode I fracture toughness is labor-intensive and time consuming. As technology advances, the utilization of available hardware becomes crucial and it is of key importance to adapt them to laboratory scale studies. In this study, it is aimed to show the adaptability of 3D printing to concrete specimen preparation for experiments by following easy-to-use procedures. One of the objectives of this study is to propose an alternative method of sample preparation for challenging mechanical experiments about fracture mechanics.

1.4. Research Methodology

The shotcrete samples were prepared using the same mix design with same ingredients and the equipment used was operated under the same laboratory condition (temperature and moisture). The optimum ingredients were selected and tested for the ideal mixture. For the shotcrete mix design, fine aggregate and high strength cement were selected in order to be able to observe the pure behavior of cracks during experiments. These materials were considered as preferable for the shotcrete mixtures related to the practical usage of shotcrete in the field.

As the interaction between aggregate and cement paste is known to have an impact on the crack propagation properties, fine aggregate (0-5 mm) was used throughout the experimental studies. The maximum aggregate size was determined based on the sample having smallest thickness as any anomalies due to the size of the aggregates were tried to be prevented.

Since methods of Mode I fracture toughness suggested by ISRM are generally for core type rock specimens, the shape of shotcrete specimens for conventional mechanical testing were also selected as core type instead of beam type which is a frequently used geometry for shotcrete fracture studies. This thesis study represents the field applications in a more realistic way by means of the specimen shape and mixture properties. With these mechanical experimental works the mix design of shotcrete were validated and the optimum curing time for fracture tests were determined.

In previous studies, suggested formulas have been proposed by modeling with similar FBD type geometries. However, for laboratory studies the sample sizes remained limited. In this study, the samples with the desired geometry were prepared by using 3D printing technology, 3D printed specimen molds, so that the suitability and applicability of the formulas found in the previous studies were also examined. An innovative and user-friendly method for preparing specimen is developed for laboratory tests of shotcrete by utilizing 3D printing technology. 3D printed molds were manufactured for fracture tests, so samples with different dimensions could be used in the experiments. This enabled the preparation and testing of samples at different dimensions as well as the efficiency of sample preparation process was improved.

FBD geometry was selected as the main geometry for the 3D printed molds. Once the FBD experimental studies were completed, the most ideal geometry was investigated. The assumptions and proposed equations made by previous researchers have been validated with the help of the actual results obtained from these laboratory analyses. In order to investigate the size effect, the fracture experiments were conducted on samples having diameters vary between 75-200 mm and loading angles vary between 20-30 degrees.

1.5. Rationale of the Study

It is necessary to examine the fracture properties of all composite materials used in underground openings (shotcrete, concrete, etc.) for safe and efficient operations in

the mining and civil engineering industry. Besides, fracture tests of core specimens as suggested by ISRM are commonly not easy and straightforward to perform as they are aiming to represent field conditions. Therefore, in this study, the general point of view is to find the fracture toughness values of specimen having conventional shotcrete mix design and to investigate the existence of size effect as well as boundary influence issue.

There are various aspects that distinguish this study from previous studies. The most important perspective is the manufacture of a sample mold with 3D printing technology. In this way, the sample sizes restricted due to the diameter of the core drill can be adjusted as desired.

Since the compressive strength of shotcrete samples is very high compared to their tensile strength, it is generally calculated by using some proportional assumptions rather than testing for it. In this study, all tensile strength values were calculated by conducted experiments.

In addition, the formulas to be verified in this study were already validated by using rock samples having similar dimensions. However, in this study, these formulas were tested in shotcrete samples of different sizes in a wider ranges and the formulas were proved to be completely based on geometry. Thus, it has been found that the formulas are not relevant with the material content and are also suitable and valid for shotcrete samples with different mix design.

1.6. Outline of the Thesis

This thesis study consists of seven chapters. In Chapter 1, aim and objective of the study is explained along with the problem statement. After that, in Chapter 2, some of the basics of fracture mechanics are summarized in order to emphasize the main research problem. Chapter 3 continues with the properties of shotcrete and its ingredients. Shotcrete mix design and the 3D printed molds are also discussed in this chapter. Testing for conventional mechanical properties of shotcrete are given in Chapter 4, whereas all of the mode I fracture toughness testing studies and their results

are explained with the help of graphs and tables in Chapter 5, which comprise the main vein of this thesis study. In Chapter 6, all experimental results are interpreted and evaluated in terms of fundamental statistical approaches such as linear regression analysis. The last conclusion chapter, Chapter 7, covers the results of the study as well as recommendations for possible future studies.

CHAPTER 2

BASICS OF FRACTURE MECHANICS

The fracture behavior of materials has been an important concept for fundamental engineering sciences, such as construction and mining. Cracks and fractures can be caused by material-related defects, unexpected loads, and other understood/ incomprehensible reasons. In order to avoid the occurrence of the same situations again, the causes of this condition and reasons lying behind the fracture mechanism should be investigated in detail. The discipline that examines these causes and mechanism is generally defined as fracture mechanics.

2.1. History of Fracture Mechanics

The first examination of the fracture events began with the works of Leonardo da Vinci (1894) and Galileo Galilei (1638) in the renaissance era. The schematic view of fracture perspective developed by Cotterell in his detailed paper about history of fracture mechanics can be seen in Figure 2.1 (Cotterell, 2002).

The schematic view of fracture perspective has begun with the illustration of iron wire strength tests of Leonardo da Vinci (da Vinci, 1894) and continued with the illustration of beam fracture performed by Galileo Galilei (Galilei, 1638).

Cotterell (2002), who mentioned David Kirkaldy's (Kirkaldy, 1864) experiments on steel as one of the important events in the 19th century, stated that Griffith's studies also hold on a very important place in fracture mechanic historian.
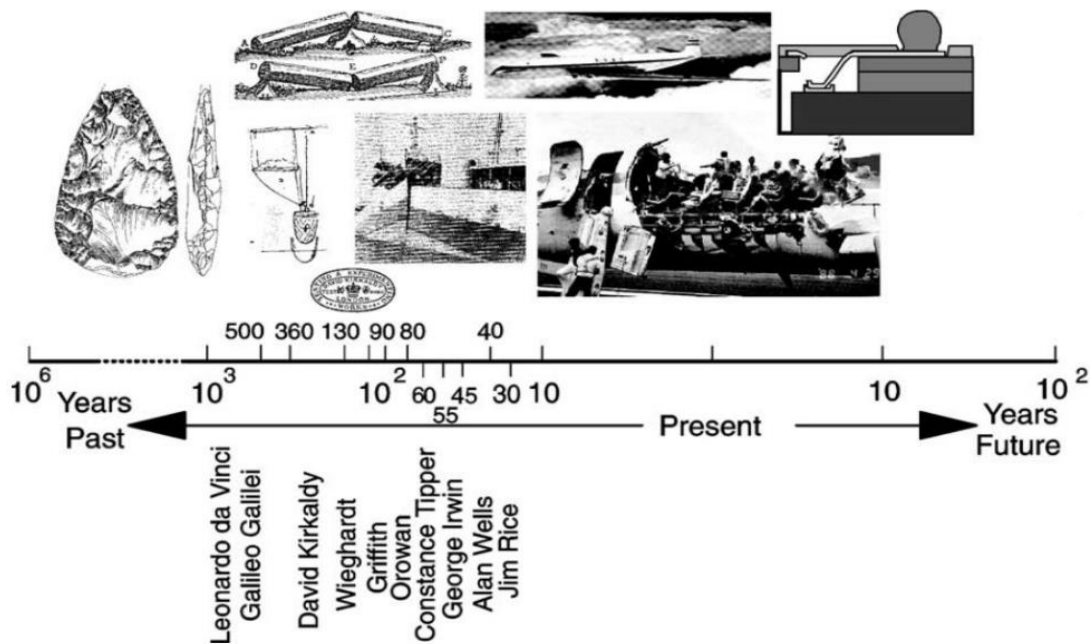
Figure 2.1 The schematic view of fracture perspective (Cotterell, 2002)

The most important driving force in the development and investigation of fracture mechanics is the fact that there are accidents caused by fracture. Figure 2.1 shows the ship named Schenectady, which was divided into two in 1943 and a Boeing 737 that lost its top section in 1988.

Investigations about fracture mechanics, pioneered by the studies of A. A. Griffith (Griffith, 1920) in the early 1920s, gained momentum in World War II as a result of accidents of ships. Griffith laid the foundations of modern fracture mechanics with his works (Griffith, 1924).

The experimental studies of Griffith were conducted on glass samples and he stated that the low strength of glass was caused by small cracks in the surface. According to Griffith, each material has micro cracks in different directions and sizes no matter how careful and controlled they are produced. Due to the stress that occurred around the ends of these micro cracks, they combine to cause the material damage (Griffith, 1920). He also realized that the stress values are in relationship with crack length. The relationship between energy, crack, crack length, and crack propagation are also

10

mentioned in his study (Griffith, 1924). Although his studies and realizations are convenient only for brittle material, he gave opportunities to many researchers by opening them new fields and providing them an innovative vision.

Although the studies related with size effect were investigated by Docherty in 1932 (Docherty, 1932), this size effect phenomenon did not attract attention because there was not much size effect on metals, which was the most commonly studied material for those years. Irwin was the researcher who realized the engineering importance of the expansion of Griffith's work and continued to develop the Linear Elastic Fracture Mechanic (LEFM) concept (Cotterell, 2002). Fracture mechanics has been a popular subject of mechanics, which has been studied on various materials and under various subtopics.

2.2. Fundamentals of Fracture Mechanics

In order to understand science of fracture mechanics and its background some fundamental concepts should be understood. Some of these are stress intensity factor (SIF), fracture toughness, linear elastic fracture mechanic (LEFM), elastic plastic fracture mechanics (EPFM) and fracture modes. In this section these concepts and parameters are mentioned briefly.

2.2.1. Stress intensity factor and fracture toughness

The stress intensity factor (SIF) developed by Barrenblatt in 1962 defines the singular stress magnitude (Barrenblatt, 1962). This factor is related with the magnitude of applied stress around the crack tip and crack length and represents as *K*. *K* is a function of applied load, crack and specimen dimensions such as size and shape. The function of SIF can be seen below;

$$K = \sigma \sqrt{\pi a} \, Y \qquad\qquad (2.1)$$

where:

σ : applied stress around the crack tip (MPa)

a : crack length (m)

Y: dimension and geometry dependent constant (dimensionless)

As can be seen from Equation 2.1, SIF is dependent on applied stress around the crack tip, crack length, specimen width, and correction factor that depends on dimension and geometry of specimen. The material properties such as Young's Modulus (*E*) and Poisson's Ratio (*υ*) are not affective parameters for SIF determination.

Fracture toughness, which denotes as K_c, defined as the critical stress intensity factor and it is a measure of toughness of a material. It is basically the resistance of the materials to fracture. K_c can be changed with the variation of temperature, loading rate and microstructure of the specimen. Because *K* is a stress based parameter, when *K* exceeds K_c, crack initiates and propagates.

A crack can proceed, when one the following two conditions are met;

    i.   When the energy stored in the material as a result of loading exceeds a critical value,

    ii.   When the value of the stress at the crack tip exceeds a critical value.

In concrete related studies, the fracture determination is generally refer as fracture energy denotes as G_c. It represents the measure of required energy for fracture and directly related with applied stress, crack length and the Young's Modulus or Modulus of Elasticity. The function of G_c is shown as below

$$G_C = \frac{\sigma^2 \pi a}{E} \qquad\qquad (2.2)$$

where:

σ = applied stress (MPa)

a = crack length (m)

E = Young's Modulus (or Modulus of Elasticity) (MPa)

When Equation 2.2 is rearranged, the right side of the Equation 2.2 is equal to K.

$$\underbrace{\sqrt{EG_c}}_{K} = \sigma\sqrt{\pi a} \qquad (2.3)$$

When a critical value of SIF (K) is reached, crack initiates and propagates and it can be represented as:

$$K = K_c \qquad (2.4)$$

The relationship between G_c (fracture energy) and K_c (fracture toughness) can be expressed as below (where E is Young's Modulus);

$$K_c = \sqrt{EG_c} \qquad \text{(plane stress)} \qquad (2.5)$$

$$K_c = \sqrt{\frac{EG_c}{(1-v^2)}} \qquad \text{(plane strain)} \qquad (2.6)$$

2.2.2. Linear Elastic Fracture Mechanic (LEFM)

All of the analytical expressions developed based on the principle that all behaviors in the material remain within elastic limits are defined as Linear Elastic Fracture Mechanics (LEFM) (Anderson, 2005). The basic principle of this method is to express the stresses which occurred at the crack end are depending on the stress applied to the part, the length and direction of the crack (Yayla, 2007).

The methodology of LEFM is based on the assumption that the material is isotropic and behaves linear elastic. These concepts point out the fact that the material properties are independent of direction and can be represented by Young's Modulus (E) and Poisson's ratio (v) as two independent elastic constants (Keleş and Tutluoğlu, 2011). The stress field near the crack tip location is calculated by following the theory of elasticity while this assumption is only valid in case the inelastic deformation has a smaller value compared to the size of the crack observed during experiments.

A major shortcoming of the linear elastic methodology is that very high stresses at the crack tip are estimated even for vanishingly small applied loads although it is known that plastic flow will always occur at this location. Elastic-plastic analysis has to be performed to determine the stress and strain distributions at the crack tip location that is known to be affected by this plastic flow. LEFM concepts are valid in case a small region near the crack tip is found as the concentration of the nonlinear deformation of the material. The criterion representing the catastrophic failure expected for brittle materials occurs accurately (Anderson, 2005).

The discrepancy is observed when plastic deformation is dominant on considerably larger regions of the material before a crack propagates. The development of Elastic Plastic Fracture Mechanics (EPFM) is based on the necessity to analyze these relatively larger regions that could be defined as plastic zones. The methodology of Elastic Plastic Fracture Mechanics (EPFM) assumes that the material analyzed is defined as elastic-plastic and isotropic. This assumption is the basis of the calculation of the strain energy fields or opening displacement near the crack tips. The crack growth is stated to increase when the energy or opening displacement exceeds the critical value (Parton, 1992).

Fracture mechanics basically investigates the conditions that increase the intensity of stresses such as cracks, notches and cavities in the material and related failures. For this reason, especially in concrete and reinforced concrete structures, how, where and under what conditions defeat will occur, under which conditions an existing crack will progress decisively or unstable is gaining importance (Akkaya, Bayramov and Taşdemir, 2003).

LEFM was first discussed by Griffith (1920) and was applied to the concrete by Kaplan (1961) in the early 1960s. However, in later studies, it was stated that LEFM is inadequate for concrete and concrete structures due to its heterogeneity and also it is found that fracture parameters cannot be calculated exactly with LEFM (Kesler, Naus and Lott, 1971). Therefore, LEFM was modified in the following years and

Nonlinear Fracture Mechanics approaches were developed (Hillerborg, Modeer and Peterson, 1976; Bazant and Oh, 1983; Jenq and Shah, 1985; Nallathambi and Karihaloo, 1986; Bazant and Kazemi, 1990).

2.2.3. Fracture modes

As Griffith (1920) explained in his work, the materials contain micro cracks and these cracks progress in three different ways depending on loading conditions. They are called fracture modes and are defined as follows (Irwin, 1958);

- Mode I is tensile opening
- Mode II is in plane sliding
- Mode III is out of plane sliding

Three fracture modes can be seen from Figure 2.2 and practical examples of these fracture modes are given in Figure 2.3.
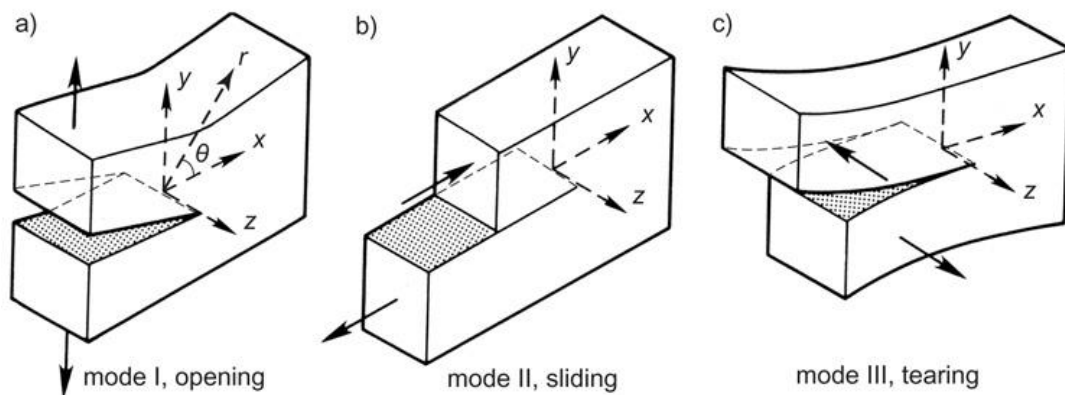
Figure 2.2 Three modes of fracture a) Opening mode I, b) Sliding mode II, c) Tearing mode III (Kanninen and Popelar, 1985)

It is known that the deformation related to cracks can be observed as either individual occurrences or a combination of any kind, defined as mixed mode.

15
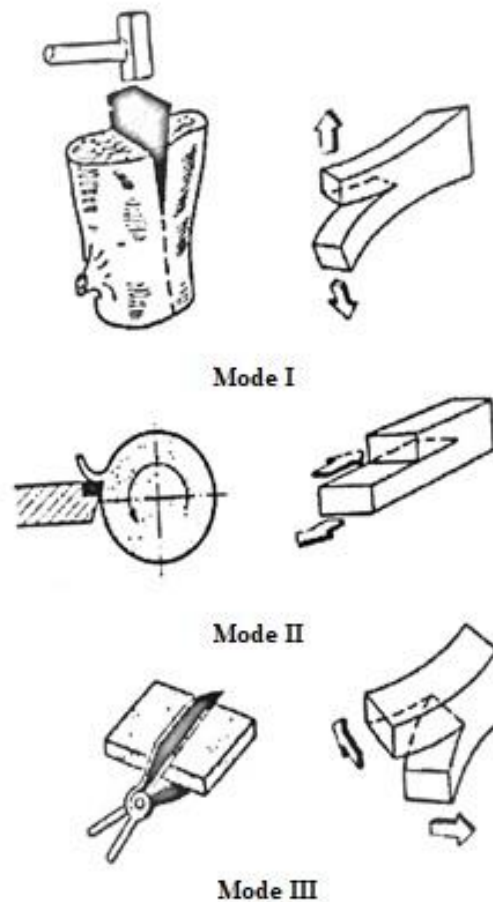
Figure 2.3 Examples of fracture modes (Yayla, 2007)

For brittle materials the essential failure mode is Mode I as the primary weakness of these materials, also for concrete, is their weakness in tension. Mode I is technically most important fracture modes, because it occurs under tension. Another reason is that it is the most common and most damageable crack propagation (Yayla, 2007).

The stress and displacement components near crack tip for mode I fracture modes were first described by Westergaard (1934) and almost ten years after his study Williams (1957) identified stress and displacement components around crack tip for mode II and mode III.

The stress components around crack tip (Figure 2.2) are expressed for mode I and mode II as listed in Table 2.1. In Table 2.1 the symbols represent;

υ : Poisson's ratio

K_I : SIF for mode I

K_{II} : SIF for mode II

r : distance from crack tip

θ : angle from x-direction

Table 2.1 Stress components around crack tip for Mode I and Mode II

	Mode I	**Mode II**
σ_{xx}:	$\dfrac{K_I}{\sqrt{2\pi r}}\cos\dfrac{\theta}{2}\left[1 - \sin\dfrac{\theta}{2}\sin\dfrac{3\theta}{2}\right]$	$-\dfrac{K_{II}}{\sqrt{2\pi r}}\sin\dfrac{\theta}{2}\left[2 + \cos\dfrac{\theta}{2}\cos\dfrac{3\theta}{2}\right]$
σ_{yy}:	$\dfrac{K_I}{\sqrt{2\pi r}}\cos\dfrac{\theta}{2}\left[1 + \sin\dfrac{\theta}{2}\sin\dfrac{3\theta}{2}\right]$	$\dfrac{K_{II}}{\sqrt{2\pi r}}\sin\dfrac{\theta}{2}\cos\dfrac{\theta}{2}\cos\dfrac{3\theta}{2}$
τ_{xy}:	$\dfrac{K_I}{\sqrt{2\pi r}}\cos\dfrac{\theta}{2}\sin\dfrac{\theta}{2}\cos\dfrac{3\theta}{2}$	$\dfrac{K_{II}}{\sqrt{2\pi r}}\cos\dfrac{\theta}{2}\left[1 - \sin\dfrac{\theta}{2}\sin\dfrac{3\theta}{2}\right]$
σ_{zz}:	0 (plane stress) υ ($\sigma_{xx}+\sigma_{yy}$) (plane strain)	0 (plane stress) υ ($\sigma_{xx}+\sigma_{yy}$) (plane strain)
τ_{xz}:	0	0
τ_{yz}:	0	0

The equations used for determining the stress component near crack tip include a constant (K_I or K_{II}) and two variables such as r (distance from crack tip) and θ (angle from x-direction) for both mode I and II.

The displacement components around crack tip are expressed for mode I and mode II as listed in Table 2.2.

	Mode I	Mode II
u_x:	$\dfrac{K_I}{2\mu}\sqrt{\dfrac{r}{2\pi}}\cos\dfrac{\theta}{2}\left\{\kappa-1+2\left(\sin\dfrac{\theta}{2}\right)^2\right\}$	$\dfrac{K_{II}}{2\mu}\sqrt{\dfrac{r}{2\pi}}\sin\dfrac{\theta}{2}\left\{\kappa+1+2\left(\cos\dfrac{\theta}{2}\right)^2\right\}$
u_y:	$\dfrac{K_I}{2\mu}\sqrt{\dfrac{r}{2\pi}}\sin\dfrac{\theta}{2}\left\{\kappa+1-2\left(\cos\dfrac{\theta}{2}\right)^2\right\}$	$-\dfrac{K_{II}}{2\mu}\sqrt{\dfrac{r}{2\pi}}\cos\dfrac{\theta}{2}\left\{\kappa-1-2\left(\sin\dfrac{\theta}{2}\right)^2\right\}$
u_z:	0	0

$$\text{where } \mu = \text{shear modulus and}$$
$$\kappa = \begin{cases} 3-4\upsilon & \text{(plane strain)} \\ \dfrac{(3-\upsilon)}{(1+\upsilon)} & \text{(plane stress)} \end{cases}$$

If the value of SIF is known, the stress and displacement components near the crack tip can be calculated from the formulas given in Table 2.1 and Table 2.2.

The crack propagates/advances when these stress and displacement values reach a certain critical value. In other words, the crack progresses when the K_I value reaches a certain critical value. For mode I, this critical stress intensity factor is called K_{Ic}. The K_{Ic} is also known as fracture toughness, which is a parameter specific to each material as other material properties like hardness and/or Young's modulus.

2.3. Mode I Fracture Toughness Testing Methods on Core Samples

There are several proposed methods to find the values of K_{Ic}, which is defined as the fracture toughness under mode I loading state. In order to compare these methods with each other, they can be grouped according to the loading conditions such as compression, tension or bending. Experimental set-up, preparation of the specimens, specimen geometry, and suitability for mixed mode fracture tests are other factors in grouping the methods (Keleş and Tutluoğlu, 2011). The comparison of these methods are summarized in Table 2.3.

In Table 2.3 the methods are given as abbreviations listed below:

- BD : Brazilian disc
- FBD : Flattened Brazilian disc
- MR : Modified ring
- HCFBD : Hole-cracked flattened Brazilian disc
- SR : Short rod
- CSTBD : Cracked straight through Brazilian disc
- DC : Diametric compression
- SECRBB : Straight edge cracked round bar bend
- SCB : Semi-circular bending
- CCNBD : Cracked chevron notched Brazilian disc
- CB : Chevron bend
- CNSCB : Chevron notched semi-circular bending

Table 2.3 Fracture tests comparison (Keleş and Tutluoğlu, 2011).

Method	Notch Type			Loading method	Set-up and equipment	Pre-crack	Mixed mode evaluation
	Straight		Chevron				
	Rotary saw	Wire saw	Rotary saw				
BD	-	-	-	Compressive	Simple	-	No
FBD	-	-	-	Compressive	Simple	-	No
MR	-	-	-	Compressive	Simple	-	No
HCFBD	Yes	-	-	Compressive	Simple	-	No
SR	-	-	Yes	Tensile	Complex	-	No
CSTBD	-	Yes	-	Compressive	Simple	Yes	Yes
DC	Yes	-	-	Compressive	Simple	Yes	No
SECRBB	Yes	-	-	Bending	Simple	Yes	Yes
SCB	-	-	-	Bending	Simple	Yes	Yes
CCNBD	-	-	-	Compressive	Simple	-	Yes
CB	-	-	-	Bending	Complex	-	No
CNSCB	-	-	-	Bending	Simple	-	Yes

According to Table 2.3, Brazilian Disc, Flattened Brazilian Disc and Modified Ring methods can be selected as the most attractive methods for the readily availability of cores, easiness of specimen preparation and simple testing set-ups, (Keleş and Tutluoğlu, 2011). In Modified Ring method, there must be a hole in the core specimen and if this hole is made before curing is complete, it will cause unnecessary cracks in the concrete. Therefore, in this study FBD geometry was preferred for mode I fracture toughness testing of the shotcrete. Brazilian disc testing method was applied as conventional testing method to find mechanical properties of shotcrete.

2.3.1. Brazilian Disc test

Brazilian Disc test is an ISRM suggested method (Ulusay and Hudson, 2007) and this method is simpler than other methods based on the experimental set-up and specimen preparation. The loading condition is compression and the completion time of this method is short enough to allow further experimentation. Schematic view of BDT type specimen can be seen in Figure 2.4 Schematic representation of BDT type specimen (modified from Alkılıçgil, 2010).
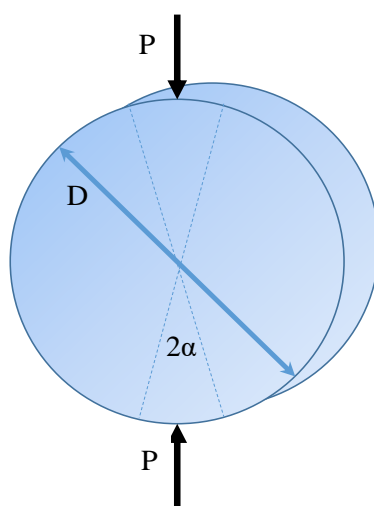
Figure 2.4 Schematic representation of BDT type specimen (modified from Alkılıçgil, 2010)

Crack initiation and progress was investigated analytically as well as experimentally in order to find fracture toughness values by Guo, Aziz and Schmidt (1993). The fracture toughness can be calculated by using Equation 2.7 below.

$$K_{Ic} = P_{min}\, x\, B * x\, Y(^a/_R) \qquad (2.7)$$

where;

K_{Ic}: fracture toughness (MPa$\sqrt{m}$)

P_{min}: minimum local load (N)

R: radius of the disc (m)

t: thickness of the disc (m)

Y(a/R): dimensionless stress intensity factor (dimensionless)

a: half of crack length (m)

$$B = \frac{2}{\pi^{3/2}\ R^{1/2}\ t\ \alpha}$$

α: half of the loading angle (radian)

Traditionally, loading angle is represented by the symbol 2α as adopted from Wang and Xing (1999), Alkılıçgil (2010) and Keleş and Tutluoğlu, (2011).

The samples prepared for Brazilian disc test does not include any notch or cut and this makes Brazilian Disc test method easier and more practical.

2.3.2. Flattened Brazilian Disc method

Wang and Xing (1999) modified the Brazilian Disc method to ensure that the crack initiation occurs at the center of the specimen and called the method Flattened Brazilian Disc method. Schematic view of FBD type specimen can be seen in Figure 2.5.
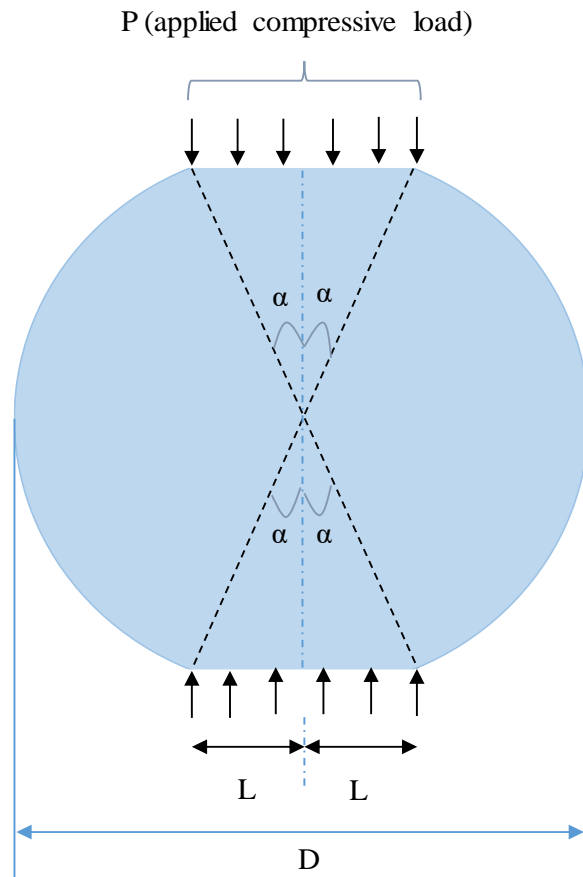
Figure 2.5 Schematic representation of FBD type specimen under loading condition (modified from Wang, Jia and Kou, 2004)

The fracture toughness can be calculated by using Equation 2.8 below.

$$K_{Ic} = \frac{P_{min}}{\sqrt{R}\, t} \, Y_{Imax} \qquad\qquad (2.8)$$

Where;

K_{Ic}: fracture toughness (MPa$\sqrt{m}$)

P_{min}: minimum local load (N)

R: radius of the disc (m)

t: thickness of the disc (m)

Y_{Imax}: maximum mode I dimensionless SIF

The difference between Brazilian disc and Flattened Brazilian disc is the flattened loading ends. This method is also one of the most attractive methods based on the specimen preparation and experimental set-up. As can be seen from Figure 2.5, D means specimen diameter and α represents half of the loading angle, whereas L represents half of the flattened end.

2.4. Fracture Mechanics Application on Concrete

Fracture mechanics are used in a wide variety of fields and have been studied on various materials. However, this study focuses mainly on molded shotcrete samples. Fracture mechanics related to concrete studies have been done since 1960s and the first trials of Linear Elastic Fracture Mechanics (LEFM) applications on concrete were done by Kaplan (Kaplan, 1961). Later, in 1970s, it was understood that LEFM was not an appropriate options for quasibrittle materials such as concrete with experiments and researchers (Kesler, Naus and Lott, 1971). The reasons behind this finding is the dimensions of the fracture process zone (FPZ) in front of and around the tip of the main cracks in concrete. This FPZ with relatively large sizes is neglected by LEFM. Therefore, many researchers have focused on non-linear fracture mechanics and have made various studies in order to fully explain cracks and failure mechanisms on concrete.

These approaches are mainly grouped as the fictitious crack (Hillerborg et al, 1976), the crack band (Bazant and Oh, 1983), the two parameter (Jenq and Shah, 1985), the effective crack (Nallathambi and Karihaloo, 1986), the size effect (Bazant and Kazemi, 1990), the peak load method (Tang, Ouyang and Shah, 1996) and the variable-notch one-size test method (Tang, Yang and Zollinger, 1999). Although in LEFM only one fracture parameter is needed, these approaches especially the size effect models require at least two parameters, which can be found with experiments, for explaining cracks and failure mechanism in concrete and/or concrete structures (Bazant and Kazemi, 1990).

In fracture mechanics, failure on concrete samples was determined generally by energy criteria. The size effect law is defined as the change/variation of stress as the size changes on geometrically similar samples of different dimensions. In the failure state of the brittle material, the load decreases as the softening progresses. One of the reasons for this load reduction which affects the mechanical behavior of material is the size effect. The fact that failure in concrete does not start at a single point, but occurs in the finite region in front of the crack indicates as the failure is initiating (Bazant and Planas, 1998). In the studies investigating the size effect, it has been observed that the failure stress changes in varying dimensions. After the maximum load level the softening phenomenon or crack development stage were dominated in the concrete structures. Size effect is the transition between LEFM and strength criterion.

The size effect in concrete structures is significant and should be taken into account in the design codes. Before failure, micro-cracking in the concrete causes deviations of the size effect from the geometrical size effect known from LEFM, because for normal geometrical size the fracture process zone is relatively large with regard to the geometry of the structure, and therefore the size effect can be correctly calculated using non-linear fracture mechanics (Eligehausen and Ozbolt, 2018).

The fracture energy (G_c) of concrete is defined as the unit energy required for crack propagation in an infinitely large sample according to Bazant. This definition is independent of both sample size and sample shape. The fracture energy obtained should be independent of the type, size and shape of the sample as geometrically similar samples can be extrapolated to an infinitely large sample (Bazant and Planas, 1998). For the brittle failure of geometrically similar concrete and concrete-like heterogeneous material, the size effect (size effect law) of Bazant (Bazant and Planas, 1998) is very commonly used in concrete community. This law will be explained in Chapter 6.2.6.

CHAPTER 3

SHOTCRETE MIXTURE AND SAMPLE PREPARATION

Studies on fracture mechanics are mostly focused on rocks. However, investigating the fracture behavior of shotcrete (sprayed concrete)/concrete is another interesting challenge, due to its wide use in underground mining support systems. Any tensile crack initiation in arch or beam type support systems may lead to the failure of the support system. Tensile mode fracture toughness might prove itself to be a useful parameter in efforts to optimize the design of thin spray liners.

Experimental work of this entire study has been planned to concentrate on shotcrete specimens. Although the shotcrete samples prepared in the laboratory were not sprayed, the samples were called shotcrete because the mixture used was suitable for shotcrete rather than concrete. The details of this distinguish is given in detail below. However, it is more appropriate to use the term "molded shotcrete samples" to distinguish it from shotcrete used in the field.

Above all, the appropriate shotcrete mixture has to be designed before the experiments are carried out. It is important to obtain the optimized mixture for shotcrete and to choose the right materials (ingredients) that make up this ideal mixture.

All of the conventional mechanical experimental works were carried out on core type shotcrete specimens. However, the fracture toughness tests were conducted on FBD type shotcrete specimens, considering the convenience of pouring mixtures into the molds designed and manufactured at different sizes.

Specimens were prepared with the same ingredients (cement, aggregate, water, and additives) and the same mix design ratio. In order to obtain consistent results from the experiments, it was aimed to make the shotcrete samples as homogeneous as possible, even though this composite material is generally defined as heterogeneous.

In general, aggregate type and granulometry, type and dosage of cement, water/cement ratio and concrete compactness are listed as factors affecting shotcrete strength values. Apart from these factors, casting and curing conditions also have an important role on the strength properties. However, the ingredients and its properties are the primary elements stated in the list of the parameters to investigate. In this part of this study, the ingredients of the shotcrete mixture, the design stages, and the casting procedure are explained in detail.

3.1. Materials

Materials used in shotcrete production are generally the same as those used for conventional concrete; aggregates, cement, water, chemical additives / admixtures, and if necessary mineral additives, such as fly ash or silica fume. Mineral additives are generally used for improving the plastic behavior of the mix design. However, in this study, mineral additives were not used for preparing the samples as it was aimed to observe the pure behavior of plain shotcrete.

All of the ingredients/materials used have been tested in the Laboratories of Turkish Cement Manufacturers' Association (TCMA) R&D Institute to investigate whether or not they are suitable for shotcrete production. Most of these tests are conformity tests to EN standards.

All of the conformity tests were carried out in accordance with *EN ISO/IEC 17025 General requirements for the competence of testing and calibration laboratories* accreditation requirements and results are given in the following sections with the uncertainty of measurements. As a result, the main purpose of this chapter is to provide detailed information about the ingredients/materials used in the experiments.

3.1.1. Cement

The most important ingredient of shotcrete is cement, which is a material with hydraulic binder properties. Portland cement is obtained by grinding clinker with appropriate proportions of gypsum. Yet, clinker is produced by mixing clay and

limestone at the proper proportions and burning them at a temperature of approximately 1400-1500°C in a rotary kiln (Kuleli, 2010).

The mechanical properties, especially strength of the shotcrete, generally depend on the type and amount of cement used. The most appropriate type of cement should be selected according to the application area. The main role of cement in shotcrete is to connect the sand and gravel granules and to give strength to shotcrete by providing adherence and cohesion in the concrete (Yalçın and Gürü, 2006).

For the experimental studies, Ordinary Portland Cement (OPC) - CEM I 42.5 R was used in the shotcrete mixture because blended cements are not common in shotcrete production and the samples are meant to represent the conditions of use in the field.

The results of the general chemical and mechanical tests conducted by the laboratories of TCMA are listed in Table 3.1. In this table, the standard limits listed in *EN ISO/IEC 197-1:2012 Cement – Part 1: Composition, specification and conformity criteria for common cements* standard are also given for available parameters. The particle size distribution of this cement can be seen in Appendix-A.

As a common behavior for practical applications, OPC having a surface area of about 4000 ± 100 cm^2/g is most preferred for shotcrete; because it provides the optimal connection between small size aggregates, sand, and gravel (Erdoğan, 2003). Therefore, when choosing the cement of mixture, the specific surface area (Blaine) parameter was examined more carefully.

As it is seen from Table 3.1, the cement used in the shotcrete mix design meets the *EN ISO/IEC 197-1* standard conformity criteria. Therefore, it can be concluded that this cement is suitable for the experiments to be conducted within the scope of this study.

Table 3.1 Chemical and mechanical test results of OPC - CEM I 42.5 R

Test Name	Unit	Results	EN ISO/IEC 197-1:2012 Standard Limits
Loss on Ignition	%	2.46	Max. 5.0
SiO_2	%	19.15	-
Al_2O_3	%	4.61	-
Fe_2O_3	%	3.54	-
CaO	%	63.15	-
MgO	%	2.32	
SO_3	%	2.78	Max. 4.0
Na_2O	%	0.60	-
K_2O	%	0.55	-
Na_2O Equivalent Total Alkali	%	0.96	-
Cl^-	%	0.0107	Max. 0.1
2 days compressive strength	MPa	29.2	Min. 20.0
28 days compressive strength	MPa	52.8	Min. 42.5 & Max. 62.5
Initial Setting Time	min.	155	Min. 60
Final Setting Time	min.	205	-
Soundness	mm	1.0	Max. 10
Density	g/cm^3	3.11	-
Specific surface area - Blaine	cm^2/g	3980	-

3.1.2. Aggregate

Aggregate is a general name given to materials such as natural sand, gravel, and crushed stone used in the production of concrete and/or shotcrete. In shotcrete mixtures, the volume of aggregates is generally around up to 65-75% by volume. Aggregates are usually obtained from crushing plants or riverbeds (Ghasemi, 2017).

There are mainly two types of aggregates used in the shotcrete production, fine aggregates (sand) and coarse aggregates (gravel). Due to the changes in the geometric shape of the aggregates, internal stresses may occur in the hardened mixture. Because of the internal stresses, the bond between cement paste (combination of cement and

water) and aggregates can be broken more easily so this situation may directly affect the strength properties. When practical applications are examined, the aggregates in the shotcrete mixtures are selected from sand, broken sand, and/or crushed stones (Hazır Beton Komitesi Yıllık Faliyet Raporu, 2017). Conventionally, the dimensions of the aggregates in the shotcrete mix design are suggested to have a maximum size of 9.5 mm (US Army Corps of Engineers, 1993). Coarser aggregates are generally not preferred in order to increase the pumpability and sprayed surface adhesion properties.

In this study, only fine natural aggregates from the same source, washed stream sand, were used for the fracture toughness experiments due to the mold dimensions and the aim of representing a practical example. Since the smallest mold thickness used in the experimental works is 50 mm, the maximum grain size (d_{max}) of the aggregates was determined to be 5 mm. If the aggregate dimensions were chosen larger, the test results might not be considered as reliable. Moreover, during experimental work, cracks might not ideally form, and the distribution of the binder might not be uniform due to the weak adherence. Also consistent test data would not be found in repeated experiments and standard deviations of results would be high. Therefore, the mix design of shotcrete contains more fine aggregates than concrete. The sieve analysis of these fine aggregates can be seen from Figure 3.1.
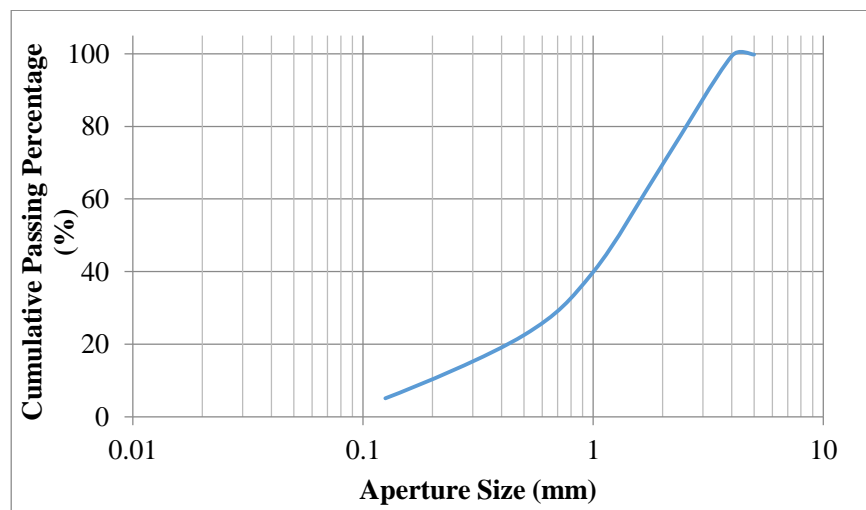
Figure 3.1 Sieve analysis of fine aggregates

29

According to the *EN 206-Concrete* standard, aggregates used in shotcrete applications should not contain harmful components such as organic compounds, chloride and sulfate salts (EN 206:2013+A1 Concrete - Specification, performance, production and conformity standard). In order to check this conformity criteria, these parameters were analyzed at TCMA's Laboratories. The results of these analyses can be seen in Table 3.2.

Table 3.2 Test results of conformity analysis of aggregates listed in EN 206 standard

Parameters	Unit	Results
Water Soluble Cl^-	%	0.0004
CaO	%	55.27
$CaCO_3$	%	98.64
Methylene Blue	g-dye/kg	0.50
Density	g/cm^3	2.51
Water Absorption	%	0.8

The methylene blue test is used for determining the amount of clay in the fine aggregates (EN 933-9 Tests for geometrical properties of aggregates - Part 9: Assessment of fines - Methylene blue test). It is generally preferred that this value is below 1.50 for construction applications (EN 206:2013+A1 Concrete - Specification, performance, production and conformity standard). Therefore, a value of 0.50 methylene blue test result means that these aggregates can be used in all construction application areas. According to the practical applications, the density of the aggregates is usually selected between 2.40 and 2.80 g/cm^3 (Yalçın and Gürü, 2006).

The technical properties of the aggregates have important effects on the mechanical properties of the shotcrete. For example, aggregates generally reduce the possibility of crack formation by preventing volume change, which might be due to the shrinkage in curing of shotcrete. Because they are durable materials, they have positive impacts on the strength properties. When selecting suitable aggregates having high abrasion

index, the abrasion resistance of the shotcrete formed with this aggregate can be increased (Mindess, Young and Darwin, 2003).

When selecting aggregate for shotcrete mix, grain size distribution is generally the first parameter to be considered. So, aggregates having the ability of being uniformly distributed in mix design are more preferable and it is also important that this distribution will not be changed when pouring or applying this mixture to any surface.

3.1.3. Water

Another important ingredient for shotcrete mixture is water. In practical usage, water that is available on site is preferably used for shotcrete production. This mixing water must be clean and depurated from the chemicals, since these can be harmful for reinforcement and shotcrete itself. Some chemicals in the mixing water might have a negative effect on the mechanical properties of the shotcrete (Kosmatka, Kerkhoff and Panarese, 2003). Due to these effects, *EN 1008 Mixing water for concrete - Specifications for sampling, testing and assessing the suitability of water, including water recovered from processes in the concrete industry, as mixing water for concrete* conformity standard was published and it is expected that the mixing water to be used will be analyzed according to this standard in case of doubt. However, in most technical specifications, it is stated that it is appropriate to use water with drinking water characteristics (EN 206:2013+A1 Concrete - Specification, performance, production and conformity standard). For the experimental works in this study, tap water is used as concrete mixing water.

3.1.4. Admixtures/Additives

Admixtures/additives are divided into two groups; i) mineral additives, and ii) chemical additives. In shotcrete production, fine-grained fly ash and silica fume can be used as mineral additives. As for the chemical additives, they are organic and inorganic chemical substances, which are ingredients of mixture other than water, aggregate, and cement. They are added to the fresh or hardened mixture in small amounts. They can generally be used for improving the properties of cement or

changing it to a certain extent. The common purpose for using chemical additives is to improve strength by sustaining workability and changing the setting time (Tokyay, 2016).

Generally, in shotcrete production two types of admixture are used, plasticizers and setting time accelerator. However, since it takes a certain time to pour the shotcrete mixtures into the molds during the experimental works, the use of the setting time accelerator additive is not considered and only a plasticizer additive is used to obtain the proper consistency.

The label of the used admixture as plasticizers is SIKA ViscoCrete Hi-Tech 2001. The properties of the admixture used are summarized in Table 3.3. These values are taken from Product Data Sheet of SIKA ViscoCrete Hi-Tech 2001 (SIKA, 2001).

Table 3.3 Properties of admixture (SIKA, 2001)

Admixture Name	Parameters	Results
SIKA ViscoCrete Hi-Tech 2001 (Plasticizers)	Density	1.06 kg/l
	pH	3-7
	Chemical base	Modified polycarboxylates based polymer

The main purpose of using plasticizer is to achieve the desired consistency of the shotcrete/concrete mixture by using less water. Consistency is a term generally used for the fluidity of mixture paste. Using less water and cement can be economically beneficial to the user while the workability is stable at the same time. Due to the plasticizer, there is no negative effect on the strength in the reduced amount of water situation.

3.2. Shotcrete Mix Design

Mixtures of shotcrete are composed of cement, water, aggregates with appropriate granulometry and, if necessary, additives/admixtures. Mix design is generally created based on the application surface and the desired strength classes. Conventional concrete has to be placed in a mold whereas shotcrete does not have to be compressed or shaped.

The most important difference between concrete and shotcrete mix design is the granulometry and maximum grain size of the aggregates. Shotcrete mix design is based on the volumetric material amount like conventional concrete design. However, shotcrete mixture contains more cement and fine aggregate than concrete mixture. One of the reasons for containing more fine aggregates is to obtain a design having higher cohesion and adhesion onto the application surface. The second reason is that the shotcrete pumps generally have a thinner hose. For this reason, an optimal formulation is needed to provide high strength, minimum cracks, high pumpability, and high adhesion properties for shotcrete.

Many mix design can be optimized according to aggregate, cement, and additive type to be used. However, as a rule of thumb, a regular mix design consists of minimum 300-400 kg cement and approximately 1600-1800 kg aggregates in 1 m^3 shotcrete mixture (EN 206:2013+A1 Concrete - Specification, performance, production and conformity standard). The amount of water should be determined based on the amount of cement (i.e. water/cement ratio), which is selected according to the desired strength values. If necessary, chemical additives (% of cement by mass) should be used to increase the mechanical properties. Since mixtures are set on a volumetric basis, unit weight, water absorption, and the particle size of the ingredients should be known. In addition, a good understanding of the properties of the surface on which shotcrete will be applied plays an important role in the choice of chemical additives.

Plasticizer is used as admixture to obtain an ideal consistency in the mix design, whereas set accelerator admixture is not used because the duration of the mixture in

the molds is long enough. The specimens are removed from the molds one day after the mixing procedure. Plasticizer around 1% of the cement by weight is added to the mixture. Besides, the addition range is indicated on the label of admixture's Product Data Sheet (SIKA, 2001).

The type and amount of cement is the most important parameter directly affecting the strength results. Therefore, OPC is used in the mixture. The amount of cement is chosen as 450 kg in 1 m^3 of shotcrete mixture for obtaining high strength and less shrinkage cracks. In practical application, the economic reasons restrict the cement amount to be applied.

The water/cement ratio is generally chosen in the range of 0.40-0.50 considering the pumpability properties of shotcrete. If this ratio is kept higher, there is a risk that the mixture cannot be settled and compacted properly. Based on these considerations, the water/cement ratio was chosen as 0.40 as an ideal consistency was aimed. The amount of shotcrete ingredients in the mix design used in the experimental works are given in Table 3.4.

Table 3.4 Details of shotcrete mix design

Material Type	Amount of material in 1 m^3 shotcrete mixture	% by volume	% by mass
Cement	450 kg	14.5	19.4
Water	180 kg (calculated from w/c ratio)	18.0	7.8
Admixture (plasticizer)	4.5 kg (%1 of cement amount by mass)	0.4	0.2
Aggregates	1684 kg (aggregate size ≤ 5 mm)	67.1	72.6
Water/cement (w/c) ratio	0.40	-	-

The shotcrete mixture listed Table 3.4 has been formed by following steps;

1. At first, the amount of cement planned to be used is determined (m_{cement}=450 kg).

2. Water/cement ratio is selected based on the application area. (w/c=0.40).

3. The amount of water is determined according to the selected water/cement ratio (m_{water}=180 kg).

4. The amount of admixture is calculated using the ratio indicated on its Product Data Sheet (the recommended ratio on Product Data Sheet is 1% by mass of cement; $m_{admixture}$=4.5 kg).

5. The volume of each ingredient except aggregates is calculated by using their density values (V_{cement}= 0.145 m^3; V_{water}= 0.180 m^3; $V_{admixture}$= 0.004 m^3)

6. Since the shotcrete mixture with a volume of 1 m^3 is targeted, the remaining volume is calculated. This remaining volume is equal to the volume of the aggregates in the mixture. ($V_{aggregate}$= 1 − (0.145 + 0.180 + 0.004) = 0.671 m^3)

7. The amount of aggregates is determined based on its density value ($m_{aggregate}$=1684 kg)

3.3. Preparation of Shotcrete Samples

The shotcrete samples used in the experimental works are prepared according to the mix design given in Table 3.4. The listed materials are weighed and mixed in a laboratory scale concrete mixer available in the Rock Mechanics Laboratory. Then, they are poured into a box-shaped mold. It is important to have a similar compaction state for every test sample. That is, the amount of voids in one sample should be almost the same for the rest.

There is a correlation between the compactness and the strength (Mindess, Young and Darwin, 2003) as seen in Figure 3.2. The mixture settling method is very important in order to obtain the same compactness state for every sample.
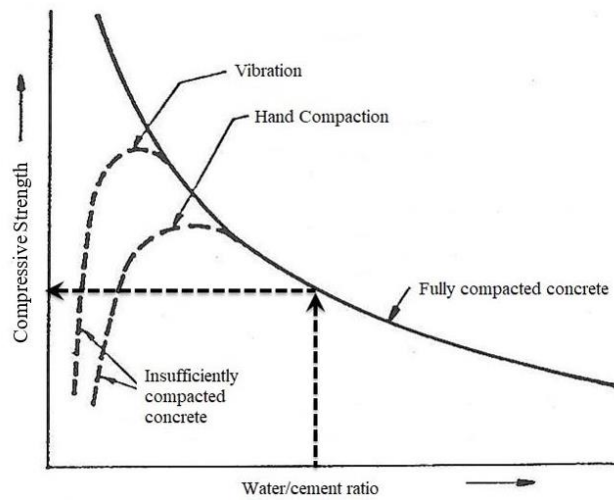
Figure 3.2 Effect of compactness on strength values of concrete/shotcrete (Mindess, Young and Darwin, 2003)

The curing time of the shotcrete mixture is very important, as the strength increases significantly, 4-5 times with the wet curing time varying from 1 to 28 days (Heere and Morgan, 2002). After completing the curing process, poured shotcrete was taken out of the curing-box. Additionally, core samples with 54 mm diameter were prepared for the conventional deformability, uniaxial compressive strength, and Brazilian type tensile strength tests (Figure 3.3). Details of the experiments and their results are given in Chapter 4 and 5.

Figure 3.3 Preparation process of shotcrete samples

In order to prepare the Flattened Brazilian disc (*FBD*) type specimens for fracture testing, the shotcrete mixture was poured into large containers. Appropriate core samples were taken through the cured mixtures. Then, a grinder mounted lathe machine was used to flatten the bottom and top surfaces of the specimens at the specified angles. This technique ended up to be unsuccessful. Smooth and properly dimensioned specimen geometries were not obtained because of the aggregates. Undesirable voids formed on the flattened surfaces of the samples. Moreover, it was difficult to change the sample diameters, since the sample sizes were limited by the available core drill diameters.

During the machining for surface flattening, coarser aggregates were separated by breaking away from the material. This caused the formation of voids on the flattened surface of the material. Three sample prepared this way was tested. Instead of following a path along the central diametric plane, it was observed that cracks proceeded to these voids at the corner of the flattened end of the sample. The samples and the path of the cracks (red boxes) after testing can be seen from Figure 3.4.

Figure 3.4 Representative view of a sample after an invalid test

So, it is decided to make specimen molds with the help of 3D printing technology to get the FBD type samples in the desired dimensions and shapes with rather smooth

flattened ends. The desired diameters, heights and loading angles values can be obtained by means of molds manufactured by a 3D printer.

3.4. 3D Shotcrete Molds

In the experimental works, the dimensions and the loading angles of the samples were to be varied different to investigate the size and geometry effect on fracture toughness. For this reason, shotcrete molds were manufactured with a 3D printer to prepare samples in the desired size and geometries. The shotcrete molds were printed with a Zortrax M300 3D printer. Image of the Zortrax M300 3D printer can be seen in Figure 3.5.

Figure 3.5 Image of the Zortrax M300 3D printer (Poligon Mühendislik, 2019)

Technical drawings of 3D-molds were made with Space Claim Software (SpaceClaim Support, 2018). An example of the drawings prepared for the shotcrete molds is given in the Figure 3.6 and all 3D drawings of molds can be seen in Appendix-B.

2α: loading angle
2L: flattened end
R: radius
D: diameter
H: height
t_m: thickness of the mold

(a) Plan view of mold   (b) 3D view of mold
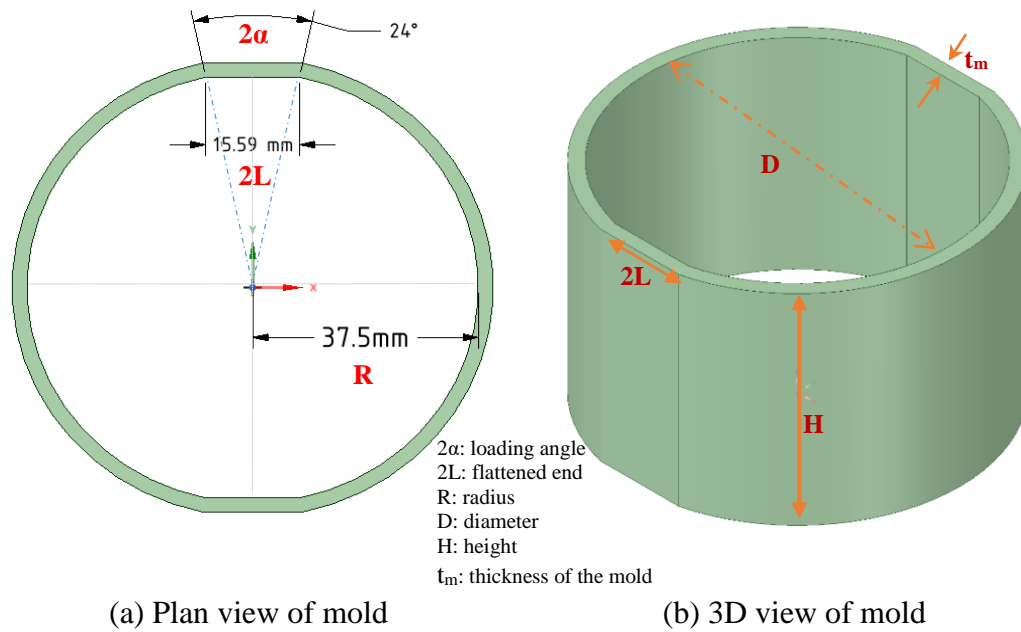
Figure 3.6 Technical drawing of 75 mm diameter and 24° loading angle shotcrete mold

There were totally 16 molds with the targeted specimen diameters of 75 mm (having 24° and 30° loading angles), 100 mm (having 22° and 28° loading angles), 120 mm (having 22° and 28° loading angles), 140 mm (having 22°, 26° and 28° loading angles), 160 mm (having 22°, 24° and 28° loading angles), 180 mm (having 22° and 28° loading angles), and 200 mm (having 20° and 22° loading angles). In order to evaluate the effect of different loading angles on the determination of the fracture toughness values, different loading angles were chosen on the same diameter. The diameter values represent the inner diameter of molds and the diameter/height (*D/H*) ratio were kept the same as 1.5. The height/radius (*H/R*) ratio were selected as 1.3 for all the samples due to the plane strain conditions. All solutions are based on plane strain condition. Geometric entities of the 16 molds are given in Table 3.5.

Table 3.5 Main dimensional parameters of 3D molds

Mold No	Diameter D (mm)	Radius R (mm)	Height H (mm)	Loading Angle 2α (º)	Wall Thickness t_m (mm)
Mold-1	75	37.5	50	24	5
Mold-2	75	37.5	50	30	5
Mold-3	100	50	67	22	5
Mold-4	100	50	67	28	5
Mold-5	120	60	80	22	5
Mold-6	120	60	80	28	5
Mold-7	140	70	94	22	10
Mold-8	140	70	94	26	10
Mold-9	140	70	94	28	10
Mold-10	160	80	107	22	10
Mold-11	160	80	107	24	10
Mold-12	160	80	107	28	10
Mold-13	180	90	120	22	15
Mold-14	180	90	120	28	15
Mold-15	200	100	133	20	15
Mold-16	200	100	133	22	15

In order to prevent any damage while the shotcrete sample is extracted out of the molds, the solidity ratio of molds was kept rather high. Solidity ratio is a measure of the ratio between the printed material and empty voids and used to represent the amount of the material in a unit print area. To make the molds compatible with changing diameters, the wall thicknesses of the molds (t_m) were adjusted to increase as the diameter increased. The wall thicknesses (t_m) of molds varied between 5-15 mm range. The representative photos of molds can be seen in Figure 3.7.

Figure 3.7 View of 16 molds used in this study

The mix design used for these molds and the amount of the material used in the mixtures are listed in Table 3.6. The material amounts were calculated according to the approximate volume of these molds. Mixtures for the increasing mold sizes were proportioned accordingly. Thus, the mix design was kept the same for all the samples.

Table 3.6 The necessary material amount of mixtures used to cast samples

Ingredients	Diameter of molds (mm)						
	75	100	120	140	160	180	200
Cement (g)	113	270	450	675	990	1395	1890
Water (g)	45	108	180	270	396	558	756
Admixture (g) (plasticizer)	1.13	2.70	4.50	6.75	9.90	13.95	18.90
Aggregates (g)	420	1008	1680	2520	3696	5208	7056

3.5. Shotcrete Sample Preparation Set-Up

Due to the size of the molds, it was not practical to mix the shotcrete mixture required for sample preparation in large scale concrete-mixer that was also available at the laboratory. Therefore, a Hobart N50 laboratory type mixer (Figure 3.8) and for larger samples UTEST laboratory type concrete mixer (Figure 3.9) was used for preparing these shotcrete mixtures.

Hobart mixer has almost 1.5-2 dm^3 capacity, therefore for amount of mixtures having larger volume, the UTEST mixer with almost 10 dm^3 capacity was used. In the first stage, where the materials given in Table 3.6 should be mixed in dry state, the mixer capacity is very important. Both mixers have adjustable and 2-stage mixing speed. The small capacity mixer has a rotation speed of 136 rpm for the agitator and 60 rpm for the attachment in low speed and 580 rpm, 255 rpm in the high speed setting. Similarly, the large scale mixer has a speed range of 10-240 rpm around its agitator and 20-480 rpm around its own axis that can be adjusted by a control button.

Figure 3.8 Hobart N50 laboratory type mixer

Figure 3.9 UTEST laboratory type concrete mixer

The application procedure during the casting of each mix design into the 3D molds for shotcrete samples used in the study is listed below.

  i.   First, aggregate and then cement are put in the mixer container. It should be noted that pouring the coarser material first is of key importance (Figure 3.10 (a)).

 ii.   The materials are mixed in dry condition for 30 seconds at slow speed (at speed no: I). The aim is to mix all solid materials homogeneously so that the coarse materials do not accumulate at the bottom of the container.

 iii.   The water and additive are mixed in another smaller container. Then this liquid mixture (water+additive) is added to the container (Figure 3.10 (b)).

 iv.   The materials are mixed in wet condition for 30 seconds at slow speed (at speed no: I) (Figure 3.10 (c)).

  v.   The materials are mixed for 30 seconds at fast speed (at speed no: II). The aim of increasing the speed is to obtain an ideal consistency of the mixture homogeneously as the water in the mixture is considerably less than conventional concrete mixture (Figure 3.10 (d)).

It is important to put the coarser material (aggregate) in the container first, because of two reasons. If the coarse materials are left above the fine materials, the mixture cannot be mixed well. The second reason is that the fine material remains adhered to the wall of the container in case they are kept under the coarser material. Therefore, the material balance in the mixture is changed.

After placing the ingredients in the container, it is aimed to mix fine materials with coarser material and make the mixture homogenous by mixing it dry first. Also in this stage, if all of the fine material remains on top, it will absorb most of the water and change the water/cement ratio balance in the mixture. The reason of mixing admixture with water is that admixture performs its function together with water to achieve the ideal consistency of mixture.

Figure 3.10 Sample preparation procedure (a) dry mixing, (b) chemical additive with water, (c) materials after slow mixing process, (d) material after fast mixing process

The mixture appears to be relatively dry (Figure 3.10 (c)) when mixing slowly, but it is essential that no additional water is added to eliminate the dryness. Instead, the mixing operation proceeds according to the procedure and the desired consistency is reached in the rapid mixing step (step v). While the material is mixed quickly, it will provide the ideal consistency to leave some of the water that aggregates hold (Figure 3.10 (d)). Therefore, it should be kept in mind that if a mix design prepared according to the appropriate calculation has remained dry, the problem is in the mixing process.

For each sample, much attention was given to the consistency and the homogeneity of the mixture. Therefore, especially in the mixture with a large amount of material, the walls of the container were controlled twice.

After the mixture was prepared according to the procedure, this mixture was filled into the 3D molds. Normally, two methods are used when filling concrete into molds. In the first method, the mixture is put into the molds manually and placed with the help of a mallet. In the second method, the material is placed in the mold with the help of a vibrating equipment so that the material does not contain air voids.

In this study, the vibration method was preferred in order to avoid problems caused by voids. Since the molds are small compared to the normal concrete molds, no device is used for vibration operation. This vibrating process is conducted manually and some images of samples after vibration process can be seen in Figure 3.11.

It is known that the temperature and moisture of the area where the mixture is casted has an effect on the mechanical properties of concrete. For this reason the environmental conditions during concrete casting was kept same.

Figure 3.11 Images of some samples after vibration process (a) in Mold-14, (b) in Mold-15, (c) in Mold-14 and Mold-12, (d) in Mold-16

CHAPTER 4

TESTING FOR CONVENTIONAL MECHANICAL PROPERTIES OF SHOTCRETE

In order to predict and determine the mechanical behavior of a material, first it is necessary to learn about its basic mechanical properties. Therefore, before investigating the fracture behavior of shotcrete, it is important to determine the mechanical properties of them. Density and porosity, static deformability, Uniaxial Compressive Strength (*UCS*) tests, and Brazilian Disc tests (*BDT*) are some of the fundamental tests to be considered for this purpose.

All the tests were completed according to ISRM suggested methods (Ulusay and Hudson, 2007). For the entire experimental program, MTS 815 Rock Testing System was used. An external 500 kN load cell is connected to the MTS 815 servo controlled loading machine. During static deformability tests in order to find the circumferential and axial strain, transducers and extensometer of MTS were attached on the specimens.

The density and porosity tests, *UCS* and *BDT* tests were conducted on shotcrete samples with different curing time for validation purposes. Tests were conducted on water-cured samples in validation studies. After determining the curing time for the experiments to be continued, tests were repeated on air-cured samples at the determined curing time. The relationship between tests results and curing time as well as the relationship between uniaxial compressive strength (σ_c) and tensile strength (σ_t) had a very important role to determine the curing time.

4.1. Density and Porosity Tests for Validation

Density and porosity tests were conducted on shotcrete specimens having different curing times as 2-days, 7-days, and 28-days. Samples of different sizes were prepared

for *UCS* and *BDT* tests as well and the density calculation was made from these samples in different sizes to control the homogeneity of the prepared specimen. For this purpose, the size of the third sample group is different from the others. The density values of these specimens were determined and listed in Table 4.1.

Table 4.1 Density test results of shotcrete specimen for different curing time

ID	Curing time t_d (days)	Diameter D (cm)	Length L (cm)	Mass M (g)	Density ρ (g/cm^3)
1		5.38	14.40	678.0	2.07
2	2	5.34	14.50	670.0	2.06
3		5.32	1.82	82.9	2.05
				Avg. ± Std. Dev.	*2.06±0.01*
1		5.26	14.30	640.8	2.06
2	7	5.28	14.30	648.6	2.07
3		5.31	2.90	136.2	2.06
				Avg. ± Std. Dev.	*2.06±0.01*
1		5.28	14.20	642.9	2.06
2	28	5.30	14.10	638.4	2.05
3		5.32	3.00	137.0	2.05
				Avg. ± Std. Dev.	*2.05±0.01*

As seen from Table 4.1, the average density value for all the samples is 2.06 g/cm^3. The density of hardened concrete is not expected to change with respect to the curing time and there is no major change due to air voids (Yalçın and Gürü, 2006).

Another purpose of measuring the weight of the samples before the tests is to check the mold settlement conditions of the shotcrete mixture. As it is seen in Table 4.1, the compactness of the sample is almost the same for every sample and every curing time. In other words, the compactness of the concrete is generally controlled by the void ratio and thus by the density test. Table 4.1 shows that the density values of the samples are very close so the compactness can be stated to be at the same degree.

50

To check the change for air voids, porosity tests were also conducted on prepared shotcrete sample. The porosity tests results can be seen in Table 4.2.

Table 4.2 Porosity tests results shotcrete specimen for different curing time

ID	Curing time t_d (days)	Porosity Φ (%)
1		5.8
2	2	5.6
3		6.0
Avg. ± Std. Dev.		*5.8±0.2*
1		6.3
2	7	5.6
3		5.7
Avg. ± Std. Dev.		*5.9±0.4*
1		5.5
2	28	6.2
3		5.7
Avg. ± Std. Dev.		*5.8±0.4*

According to Table 4.2, it is seen that the porosity values is almost the same for three different curing time and between %5.5-6.0 range.

4.2. Deformability Tests for Validation

Static deformability tests were carried out according to *ISRM* suggested method to determine the Young's Modulus (*E*), Poisson's ratio (*v*), and uniaxial compressive strength (σ_c) (Ulusay and Hudson, 2007). In order to check the quality and uniformity of shotcrete mix design, deformability tests are conducted on 15 samples with different curing time, 1-day, 2-days, 3-days, 7-days, 14-days, and 28-days, respectively. Each shotcrete sample was approximately 135 mm in length and 54 mm in diameter. The uniaxial compressive strength (σ_c), Young's Modulus (*E*) and Poisson's ratio (*v*) values are listed in Table 4.3.

Table 4.3 Deformability Test Results for Validation

Sample ID	Curing time t_d (days)	Uniaxial Compressive Strength (σ_c) MPa	Peak Load (P) kN	Young's Modulus (E) GPa	Poisson's ratio (v)
1		11.9	25.5	30.0	0.19
2	1	11.6	25.8	29.2	0.22
3		12.0	26.4	23.2	0.32
Avg. ± Std. Dev.		*11.8±0.2*	*25.9±0.5*	*27.5±3.7*	*0.24±0.07*
1		23.8	53.5	39.9	0.23
2	2	26.0	57.5	40.6	0.23
3		28.2	62.5	40.7	0.23
Avg. ± Std. Dev.		*26.0±2.2*	*57.8±4.5*	*40.4±0.4*	*0.23±0.00*
1		29.7	65.9	44.1	0.28
2	3	26.1	74.9	48.1	0.26
3		31.0	72.7	46.2	0.29
Avg. ± Std. Dev.		*28.9±2.5*	*71.2±4.7*	*46.1±2.0*	*0.28±0.02*
1		40.7	90.5	52.8	0.24
2	7	40.8	90.6	49.9	0.26
3		35.9	73.6	51.4	0.29
Avg. ± Std. Dev.		*39.1±2.8*	*84.9±9.8*	*51.4±1.5*	*0.26±0.03*
1		43.2	96.8	53.0	0.26
2	14	41.0	91.9	48.9	0.27
3		40.9	91.3	53.1	0.3
Avg. ± Std. Dev.		*41.7±1.3*	*93.3±3.0*	*51.7±2.4*	*0.28±0.02*
1		47.6	105.3	49.1	0.25
2	28	43.9	92.9	57.8	0.31
3		46.7	103.2	49.2	0.27
Avg. ± Std. Dev.		*46.1±1.9*	*100.5±6.6*	*52.0±5.0*	*0.28±0.03*

Photos of a randomly selected sample before, during, and after the test can be seen in Figure 4.1. Other sample photos of deformability tests are given in Appendix-C.

(a) before test   (b) during test   (c) after test
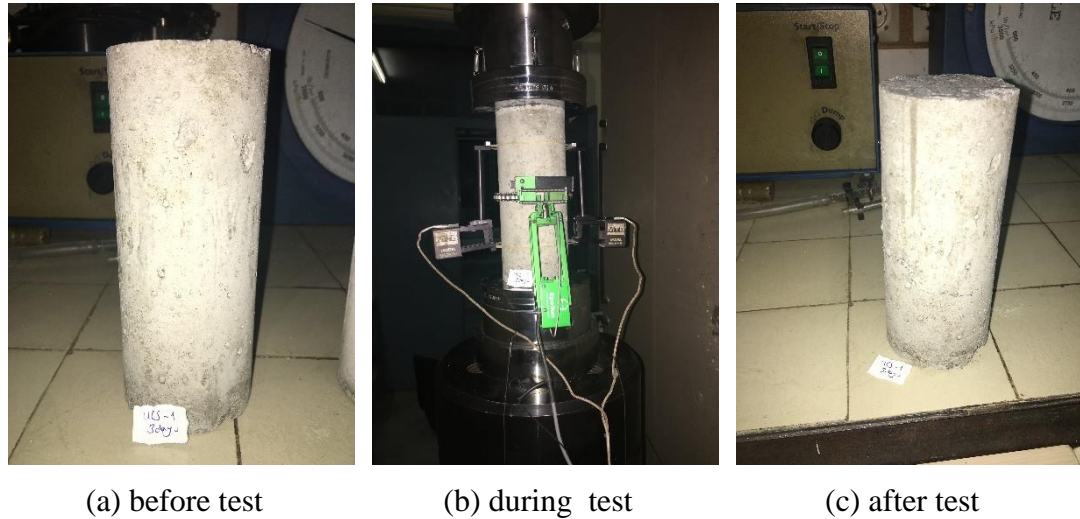
Figure 4.1 Photos of a specimen taken (a) before, (b) during and (c) after UCS *test*

The average of axial stress (σ_{axial}), axial strain (ε_{axial}) and lateral strain ($\varepsilon_{lateral}$) calculated from the deformability test results of 5 different specimen for each curing time can be seen in Figure 4.2 below.

UCS values and *E* values increased as expected with increasing curing time. As it was a shotcrete mixture, the ascent in the early days was fast, and the change of the *UCS* values for the 14 and 28 days is considerably smaller than the change in first 3 days. C30 / 37 type concrete was targeted as a mix design. C30 / 37 type concrete means that 28-days compressive strength of cubic samples should be reach a minimum of 37 MPa, and 28-days compressive strength of cylindrical samples should be reach a minimum of 30 MPa. In Figure 4.2, the *UCS* value obtained from the 7-day cylindrical samples exceeds 30 MPa, which means a representative mixture is obtained in 7 days as targeted. The curing time to be determined according to the entire validation studies for FBD samples can be most probably 7 days due to the UCS results.
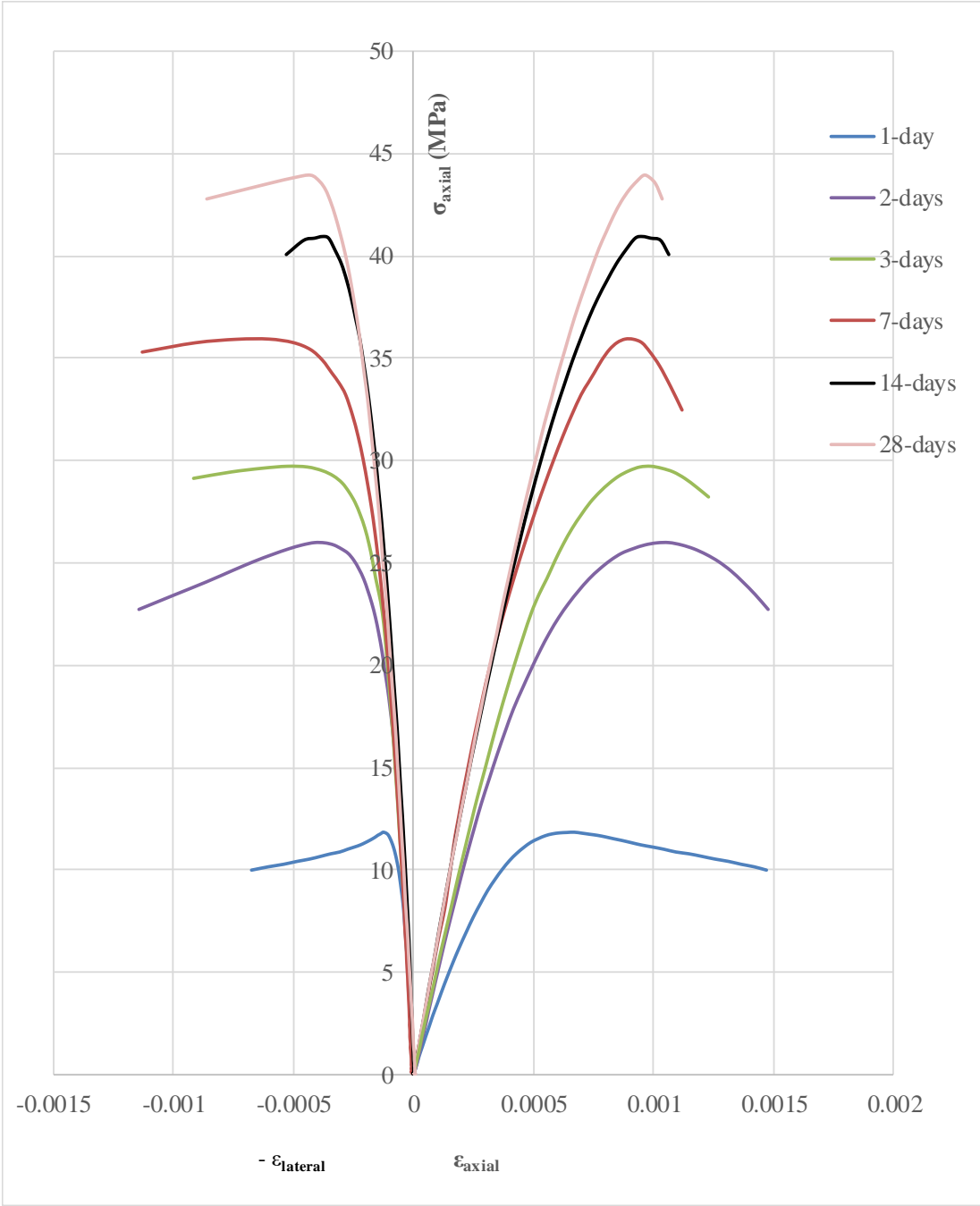
Figure 4.2 The average of axial stress (σ_{axial}) - axial strain (ε_{axial}) and axial stress (σ_{axial}) - lateral strain ($\varepsilon_{lateral}$) of shotcrete samples with 6 different curing time

The individual and average uniaxial compressive strength test results can be seen in Figure 4.3 and in this figure; the red dots represent the average values, whereas blue dots represent the results of each individual test sample. Besides, the dashed red line and equation represents the relationship between average σ_c results and curing time (t_d).
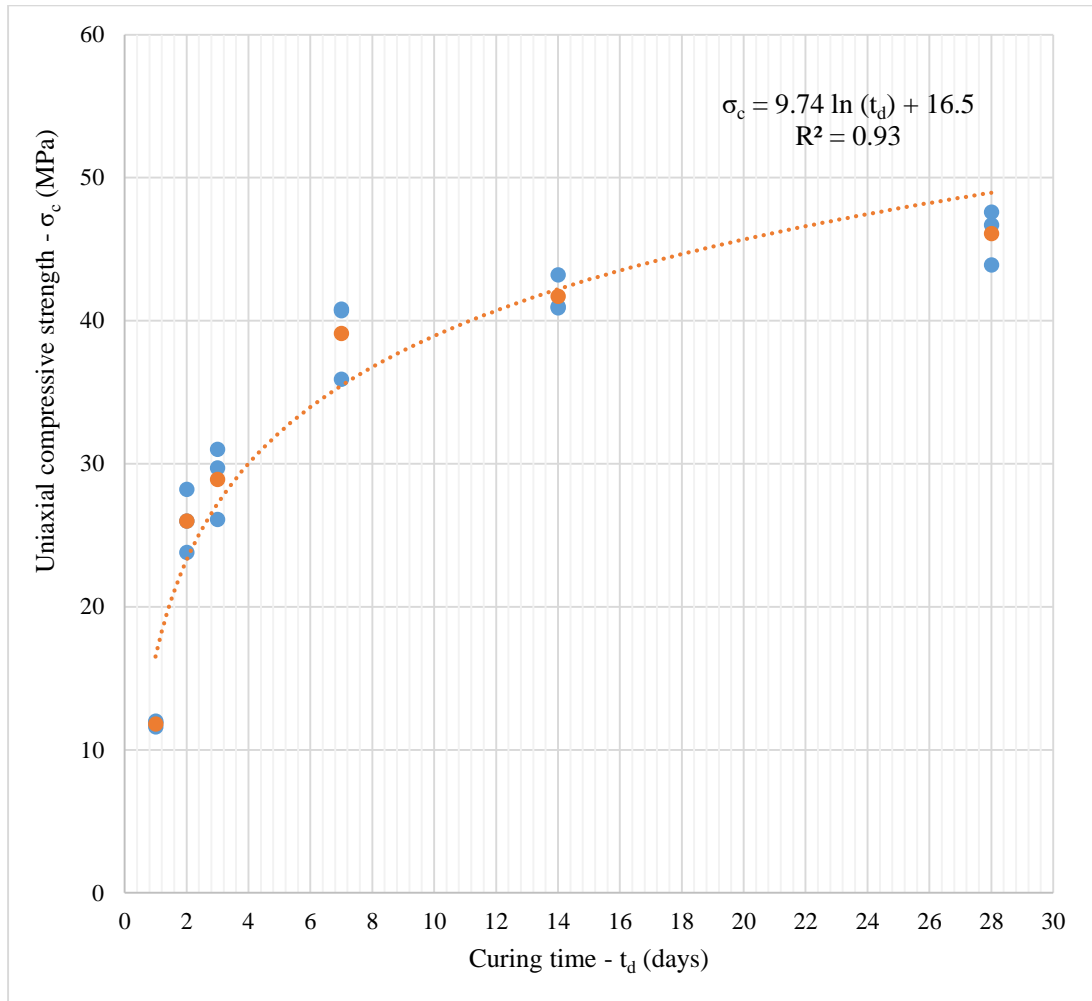
Figure 4.3 The relationship between uniaxial compressive strength and curing time

These values for different curing times appear to be higher than the values of the shotcrete samples applied on site. One of the reasons for this difference may be due to the spraying effect that was not simulated in the sample preparation process under the

55

laboratory conditions. In the field application, this effect may not be fully applied. In addition, the curing condition for all of the sample are nearly perfect as desired unlike practical application.

Since the mechanical tests results of validation studies are within acceptable limits, it has been decided to continue with this mixture in further validation tests. However, minor changes in the further deformability analysis after validation tests results were expected because of heterogeneous nature of shotcrete.

4.3. Brazilian Disc Test for Validation

For validation studies, Brazilian Disc tests were conducted on 15 shotcrete core samples having 6 different curing times, 1-day, 2-days, 3-days, 7-days, 14-days, and 28-days, respectively. Shotcrete samples were around 30-35 mm in thickness and around 54 mm in diameter.

Photos of a randomly selected *BDT* sample taken before, during, and after BDT can be seen in

Figure 4.4. Other sample photos of deformability tests are given in Appendix-C.

| (a) before test | (b) during test | (c) after test |
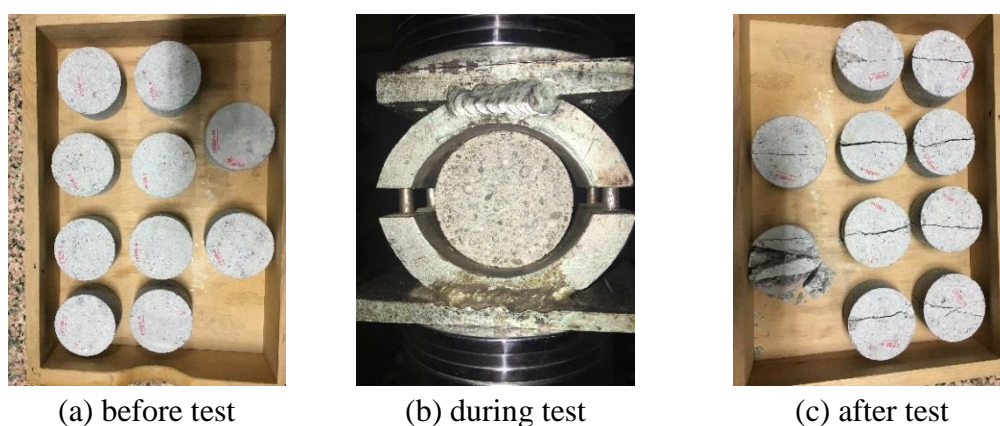
Figure 4.4 Specimen photos taken (a) before, (b) during, and (c) after BDT for validation

BDT results of shotcrete specimen for different curing time are listed in Table 4.4.

Table 4.4 BDT results for validation

ID	Curing time t_d (days)	Peak Load P (kN)	Tensile Strength σ_t (MPa)
1		4.7	1.7
2	1	5.3	1.9
3		5.2	1.8
	Avg. ± Std. Dev.	*5.1±0.3*	*1.8±0.1*
1		8.5	2.9
2	2	8.9	3.1
3		9.2	3.2
	Avg. ± Std. Dev.	*8.9±0.3*	*3.1±0.2*
1		9.2	3.3
2	3	9.4	3.3
3		8.9	3.1
	Avg. ± Std. Dev.	*9.2±0.3*	*3.2±0.1*
1		11.8	4.1
2	7	12.2	4.2
3		11.2	3.8
	Avg. ± Std. Dev.	*11.7±0.5*	*4.0±0.2*
1		12.5	4.3
2	14	11.5	4.0
3		11.9	4.1
	Avg. ± Std. Dev.	*12.0±0.5*	*4.1±0.2*
1		12.9	4.5
2	28	12.2	4.3
3		12.0	4.2
	Avg. ± Std. Dev.	*12.3±0.5*	*4.3±0.2*

The relationship between tensile strength (σ_t) and curing time (t_d) can be seen in Figure 4.5.

The figure displays a scatter plot with the fitted equation:
$$\sigma_t = 0.69 \ln(t_d) + 2.30$$
$$R^2 = 0.86$$
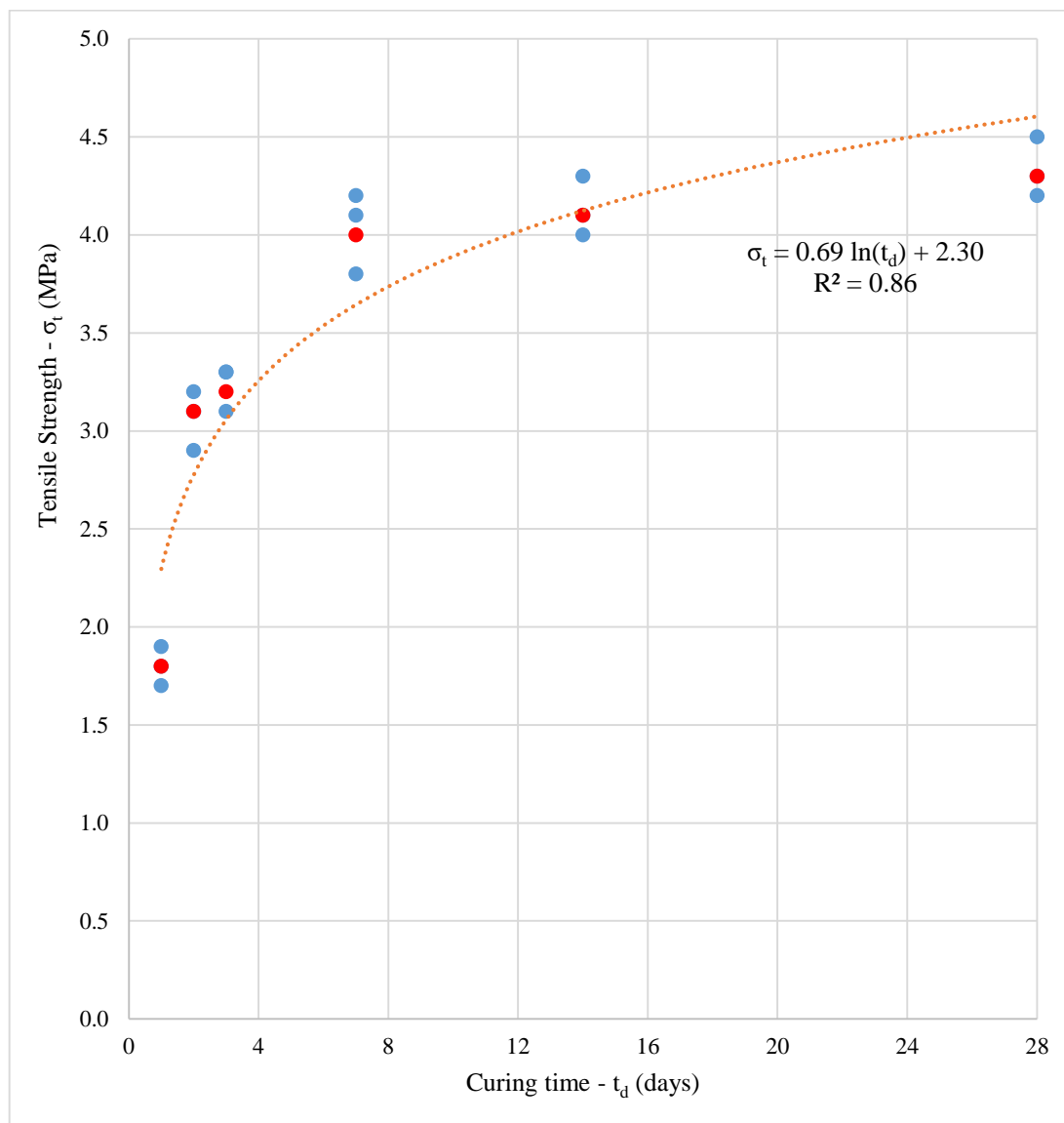
Figure 4.5 The average tensile strength values of shotcrete specimen according to different curing time

As seen in Figure 4.5, tensile strength (σ_t) increases almost twice with the increasing curing time. It is validated that shotcrete has lower tensile strength than compressive strength as expected. Moreover, the standard deviation values found in BDT are smaller than the standard deviation values found in *UCS* tests.

4.4. Validation Analysis for Determined Curing Time

Since 28 days curing time were assumed to be long to complete the entire experimental program, the optimum curing time had to be determined. This optimum curing time was determined with the help of conventional mechanical tests results and literature.

In general, for reinforced concrete design calculations, the tensile strength of plain concrete is assumed negligible, since the tensile strength of entire system is to be provided by reinforcement such as bars. In reinforced concrete design related literature, it is reported that the tensile strength of concrete can be assumed as 1/10 of its compressive strength (Pillai, Erki and Kirk, 1999). Therefore, the UCS/σ_t values of shotcrete samples used in this study for different curing times are listed in Table 4.5.

Table 4.5 UCS/σ_t *values of water-cured samples*

Curing Time (days)	UCS/σ_t			
	Sample-1	Sample-2	Sample-3	Avg. ± Std. Dev.
1 day	7.0	6.1	6.7	6.6 ± 0.5
2 days	8.2	8.4	8.8	8.5 ± 0.3
3 days	9.0	7.9	10.0	9.0 ± 1.0
7 days	9.9	9.7	9.4	9.7 ± 0.2
14 days	10.0	10.3	10.0	10.1 ± 0.1
28 days	10.6	10.2	11.1	10.6 ± 0.5

The highest UCS/σ_t ratio is found as 10.6 on average for 28-days water-cured samples here. In order to see the relationship between UCS/σ_t ratio and curing time, the average values of the UCS/σ_t ratio of water-cured shotcrete samples used in this study are plotted in Figure 4.6 according to the dimensionless curing time. Dimensionless curing time represent 1/28 (day/day), 2/28 (day/day), etc.

The graph shows a plot with y-axis labeled "Uniaxial compressive strength / Tensile strength UCS/σ_t" ranging from 0.0 to 12.0, and x-axis labeled "Dimensionless curing time - t_d" ranging from 0 to 1. The trend equation shown is:

$$\text{UCS}/\sigma_t = 1.08 \ln(\text{dimensionless } t_d) + 10.93$$
$$R^2 = 0.89$$
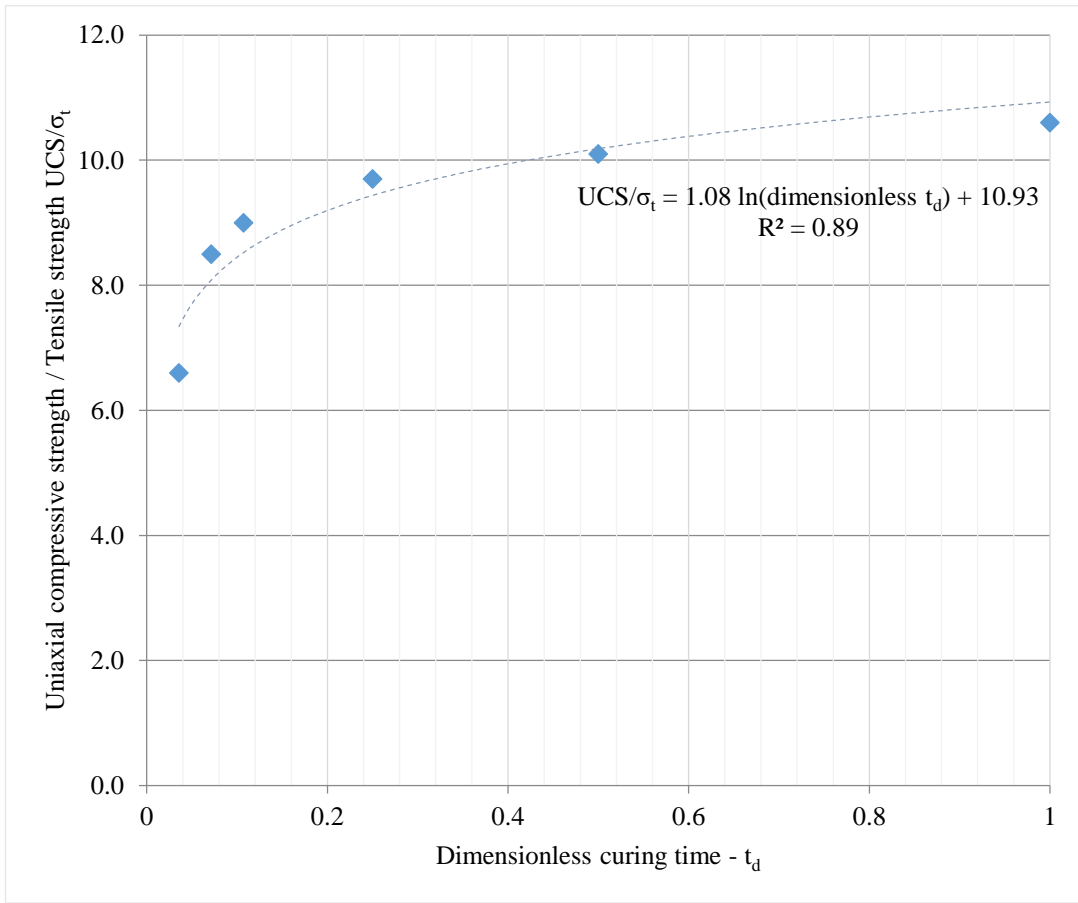
Figure 4.6 The average UCS/σ_t *ratio according to dimensionless curing time*

As can be seen from Figure 4.6, *UCS/σ_t* ratio rapidly increase first 3 days, and after 7th day this increase slow down. Additionally, the UCS values of shotcrete sample at 7 day curing time is more than 30 MPa, which is the standard limit of 28 days compressive strength for C 30 / 37 cylindrical type concrete mixture. Therefore, samples were subjected to 7 days curing time for fracture toughness tests to save time in completing the overall experimental program.

4.4.1. Deformability tests on 7-days curing time

In prior validation studies, the shotcrete specimens are cured in water. But after specifying the curing time as 7 days, the deformability tests were repeated on 4-core shotcrete specimens cured 7 days in the air to represent the field condition. Each shotcrete sample was approximately 136 mm in length and 54 mm in diameter. With

the help of the deformability tests, Young's Modulus (E), Poisson's ratio (v), and σ_c values were determined. Specimen photos taken before, during, and after deformability tests can be seen in Figure 4.7.

| (a) before test | (b) during test | (c) after test |
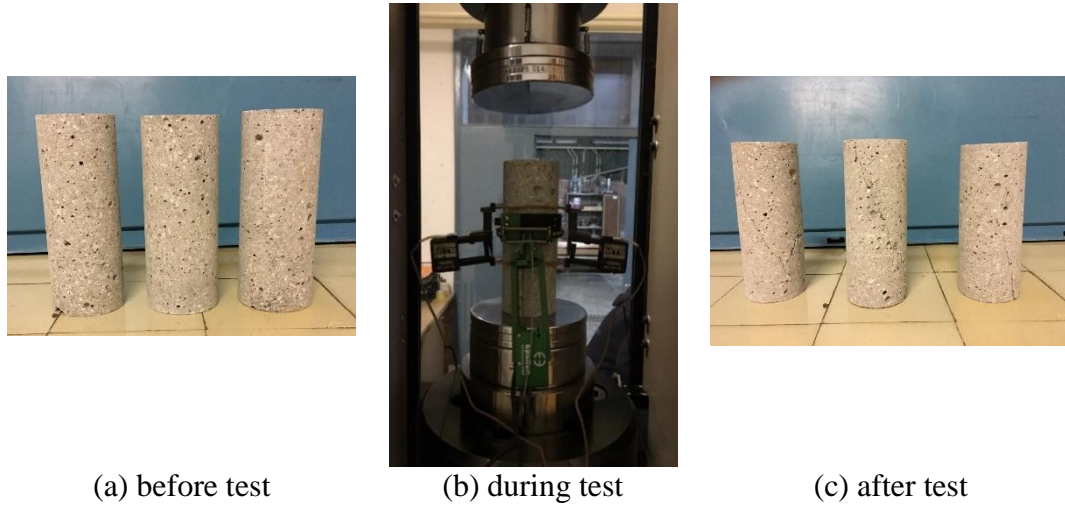
Figure 4.7 Specimen photo taken (a) before, (b) during, and (c) after deformability test

The stress-strain curve of a randomly selected sample out of 4 samples are given in Figure 4.8 below.
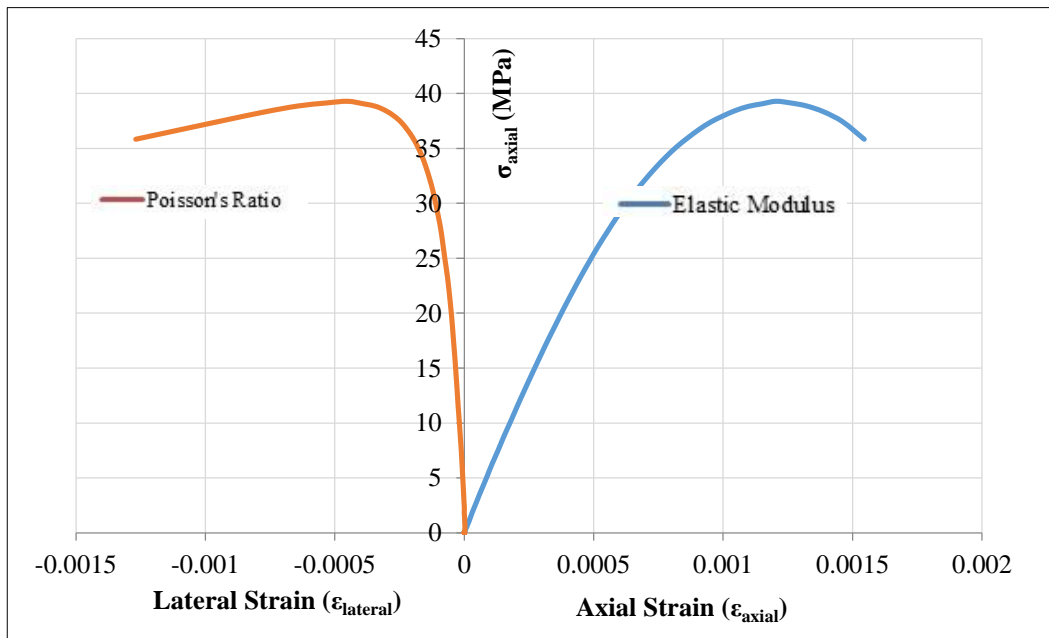
Figure 4.8 Stress-strain curve of a randomly selected shotcrete sample

When load started to drop, the deformability test was stopped and test data were recorded in order to drawn axial stress-axial strain (σ_{axial}-ε_{axial}) and axial stress-lateral strain (σ_{axial}-$\varepsilon_{lateral}$) graphs. E and υ values were calculated from these graphs.

The results of the static deformability tests of air-cured shotcrete specimen for 7-days are given in Table 4.6.

Table 4.6 UCS and deformability test data of air-cured shotcrete specimen for 7 days

ID	Uniaxial Compressive Strength - σ_c (MPa)	Peak Load P (kN)	Young's Modulus E (GPa)	υ
1	39.6	90.7	50.9	0.23
2	39.0	89.1	48.7	0.25
3	40.3	89.7	52.8	0.24
4	38.6	88.3	48.5	0.26
Avg ± Std. Dev.:	*39.4±0.7*	*89.5±1.0*	*50.2±2.0*	*0.25±0.01*

According to Table 4.6 the average deformability test values are as follows; average σ_c is obtained as 39.4 MPa, average E is determined as 50.2 GPa, and average υ is calculated as 0.25, respectively. The difference between deformability test results of sample with curing in water and in the air is acceptable, therefore; air curing will be used in the remaining experiments for fracture analysis.

4.4.2. BDT tests on 7-days curing time

After deciding 7 days as curing time, BDT is repeated on 4 air-cured shotcrete core samples to compare the tensile strength of air-cured samples to the water-cured ones. Shotcrete samples were around 30-35 mm in length and around 54 mm in diameter. Specimen photos taken before, during, and after BDT can be seen in Figure 4.9.

| (a) before test | (b) during test | (c) after test |
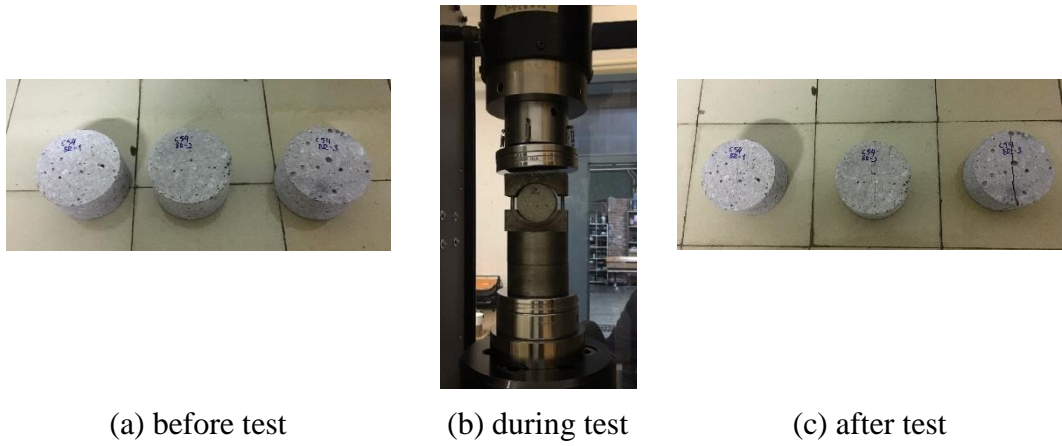
Figure 4.9 Air-cured BDT samples (a) before, (b) during and (c) after the test

A typical load-displacement graph of a randomly selected sample out of 4 samples is given Figure 4.10 below.
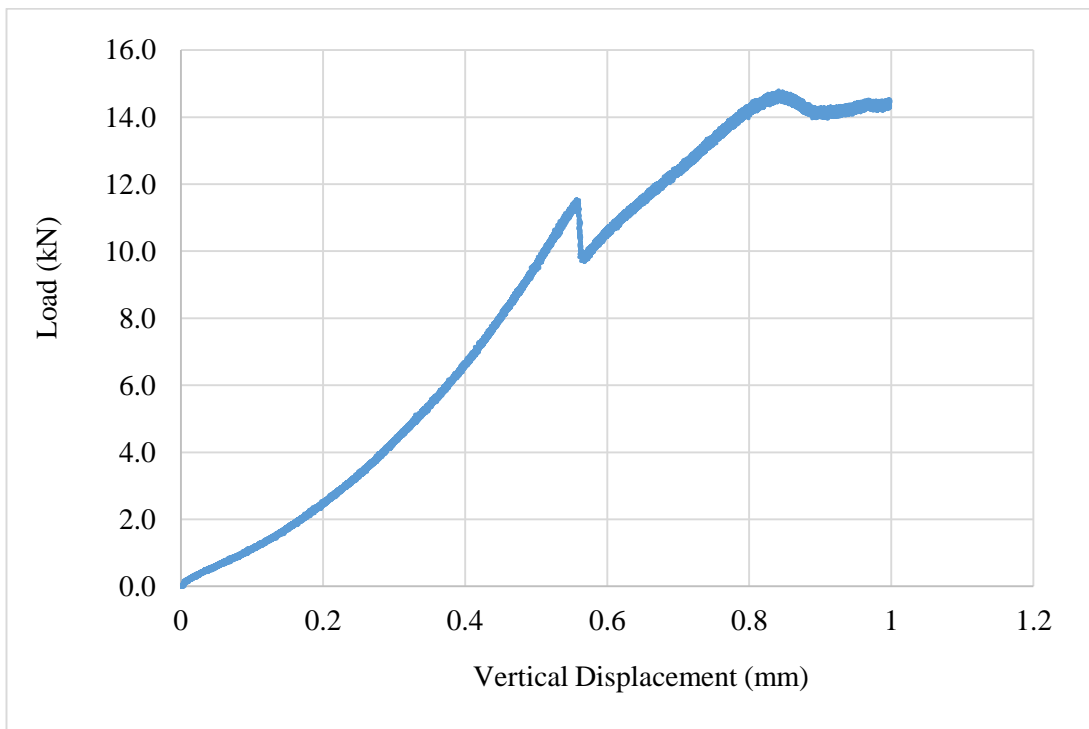
Figure 4.10 Load vs. vertical displacement graph of sample no#1

As seen in Figure 4.10, the load drop phenomena of fracture tests with FBD geometry is observed in all of the BDT with curved jaws. This is believed to be a result of using curved jaws on the upper and lower boundaries of BDT samples. Jaws to distribute the load is possibly generating an effect similar to machining a flat end with a loading angle of around 20° at the boundaries.

BDT results, tensile strength (σ_t), and peak load of air-cured shotcrete specimen for 7-days curing time are given in Table 4.7.

Table 4.7 BDT results of air-cured shotcrete specimen for 7-days curing time

ID	Peak Load P (kN)	Tensile Strength σ_t (MPa)
1	11.5	4.3
2	11.6	4.1
3	11.7	4.1
4	10.4	3.9
Avg. ± Std. Dev.	*11.3±0.6*	*4.1±0.2*

The average tensile strength is determined as 4.1±0.2 MPa for the air-cured samples. Average failure (peak) load is evaluated as 11.3±0.6 kN. The difference between BDT results of sample with curing in water and in the air is acceptable, since the BDT test results are very close. Therefore, air curing is employed in the remaining fracture experiments due to the easiness of application.

CHAPTER 5

MODE I FRACTURE TOUGHNESS TESTS ON SHOTCRETE SPECIMENS

Mode I fracture toughness K_{Ic} tests are generally conducted on beam type specimens as beam type specimens are common for concrete structures involving structural units like columns and beams. However, in this study core type specimens having Flattened Brazilian Disc (FBD) geometry are subjected to mode I fracture toughness tests due to the wide availability of core type specimens in structural and rock mechanics applications.

For all of the fracture toughness testing program MTS 815 was used and a low and constant displacement rate of 0.4 µm/sec was selected to detect the first evolution of the central crack.

In general, shotcrete samples reaches strength values, which is equal to the 28-days compressive strength values of conventional concrete, at the 7-days curing time (Austrian Concrete Society). Therefore, mode I fracture toughness tests were conducted only on 7-days cured shotcrete specimens for saving time in completing the overall experimental program.

5.1. FBD Fracture Tests

Mode I fracture toughness test was conducted on FBD test samples and these samples were cured in the air. The test samples were removed from the 3D molds 1 day after casting and waiting until the 7-day curing time. After removing from molds, a coding/labelling system was appplied on the FBD specimen as shown in Figure 5.1.
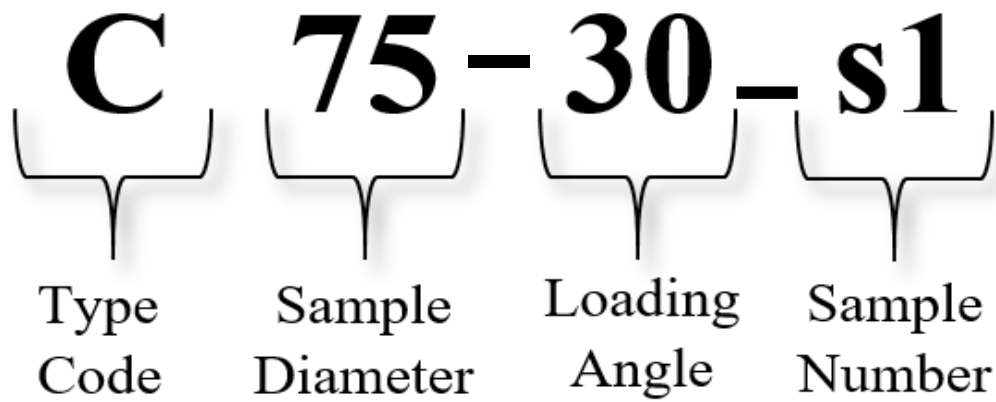
Figure 5.1 Specimen coding for FBD sample

In the coding/labelling system, the specimen type is illustrated by the letter C for shotcrete sample as "C" is the abbreviation commonly used in the construction related areas. The diameter of the sample is indicated by using the value. Then, 30 represents the loading angles (2α) ranging from 20° to 30° and *s1* indicates the sample number.

In this study, the mode I fracture toughness tests were conducted on samples with diameter of 75 mm, 100 mm, 120 mm, 140 mm, 160 mm, 180 mm, and 200 mm having different loading angles. The geometries of all the shotcrete specimen are listed in Table 5.1.

In Table 5.1, the diameter (*D*), flattened end length (*2L*), thickness (*t*), loading angle (*2α*), and the *D/2L* ratio are given. The height/diameter (*H/R*) ratio is kept the same for all the shotcrete samples, i.e. molds, as 1.3 in order to provide a specific layout between molds.

Table 5.1 Dimensions of the shotcrete specimens

Sample Code	Diameter D (mm)	Flattened Length 2L (mm)	Height H (mm)	Loading Angle 2α (°)	D/2L
C75-24	75	15.6	50	24	4.81
C75-30	75	19.4	50	30	3.86
C100-22	100	19.1	67	22	5.24
C100-28	100	24.2	67	28	4.13
C120-22	120	22.9	80	22	5.24
C120-28	120	29.0	80	28	4.13
C140-22	140	26.7	94	22	5.24
C140-26	140	31.5	94	26	4.45
C140-28	140	33.9	94	28	4.13
C160-22	160	30.5	107	22	5.24
C160-24	160	33.3	107	24	4.81
C160-28	160	38.7	107	28	4.13
C180-22	180	34.3	120	22	5.24
C180-28	180	43.5	120	28	4.13
C200-20	200	34.7	133	20	5.76
C200-22	200	38.2	133	22	5.24
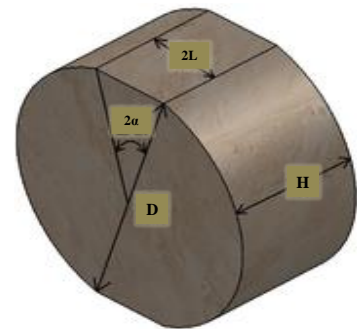
In mode I fracture toughness tests, some parameters were measured whereas some were calculated according to related equations existing in the literature. For example, the geometries of samples (i.e. diameter, thickness, loading angles), P_{min} and a_{ce} (experimental crack length) values are measured. P_{min} values are detected after the initial crack opening where the force suddenly drops because of the energy release.

As mentioned before, the dimension of experimental crack length (a_{ce}) is measured with the help of the following procedure;

i. The loading speed during the test is set to be particularly slow (0.4 µm/sec) to be able to see the first crack opening.

ii. The start and end points of the initial crack are marked on the both side of the sample when the first crack is opened at the time where there is a load drop detection in the load-displacement graph (Figure 5.2a).

iii. At the end of the experiment, the distance between the start and the end point of the initial crack was measured and recorded (Figure 5.2b).

iv. The measured crack length on the front and the back side of the sample are sometimes different to a certain and acceptable extent especially for samples with higher thickness values. Therefore, in order to be able to generalize the test results, the average values of experimental crack length on both sides were calculated and defined as a_{ce}.

(a)   (b)
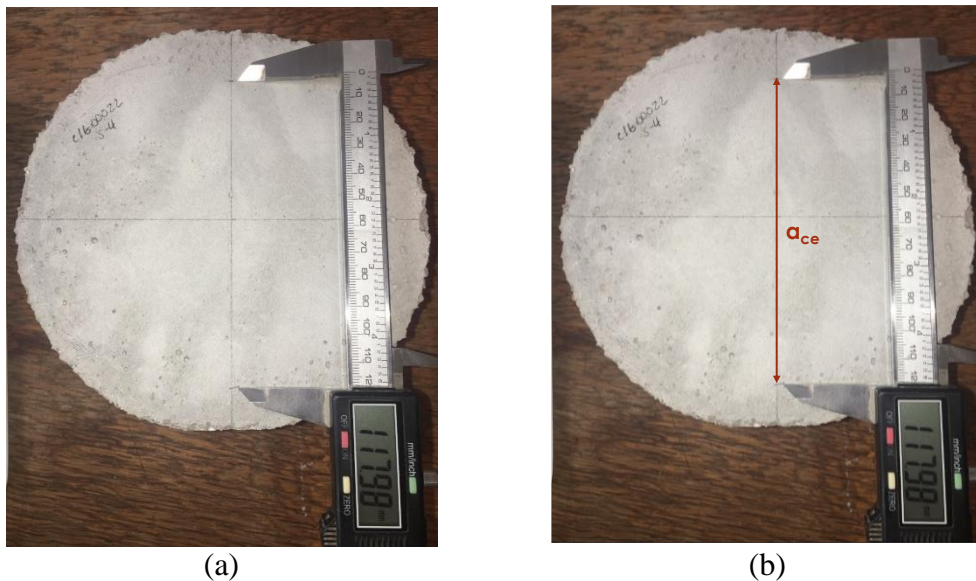
Figure 5.2 An example of the procedure of crack length measurement

Dimensionless stress intensity factor (SIF) of FBD specimen for mode I (K_I) was described by (Wang and Xing, 1999) as following Equation 5.1.

$$Y_I = \frac{K_I \, t \, \sqrt{R}}{P} \qquad\qquad\qquad (5.1)$$

In this equation; Y_I is dimensionless SIF, K_I represents SIF for mode I, P is the applied load. t and R are thickness and radius of the specimen, respectively. In order to use this formula, the SIF for mode I (K_I) must be calculated. This calculation was conducted with the help of finite element modeling. In Wang et al (2004), Y_I was found as 0.7997 valid only for $2\alpha= 20^\circ$ and as 0.5895 valid only for $2\alpha=30^\circ$.

By following the procedure described by Wang *et al.* (1999 and 2004), a new expression for Y_I can be developed covering wider loading angle ranges. This approach is done by Özdoğan (2017) and the formula derived for calculating the dimensionless SIF for mode I (Y_I), suitable for all loading angles on FBD specimen were tried to be verified.

In Özdoğan (2017), FBD tests were conducted on rock material (andesite and marble). Specimen diameters were 54, 75, 100, and 125 mm in the FBD tests. Numerical analyses were performed by ABAQUS finite element software to find mode I SIF. The J-integral approach was used for K_I computation in ABAQUS. Stress intensity factors were computed for different t, D, and 2α values with numeric models created by ABAQUS software. 2α values were changed between 2° and 50°. In the models, plane strain condition was assumed and elastic properties of materials were taken as $E= 12$ GPa and $\upsilon = 0.15$. Elastic properties does not affect the K_I computations, because the J-integral approach is a path independent scalar work based entity. K_I was converted to a dimensionless form to proceed in terms of dimensionless stress intensity factor Y_I.

In the procedure of Özdoğan (2017) K_I values were determined for different models having different crack lengths (a). To find Y_{Imax} (maximum dimensionless SIF for mode I) and corresponding critical crack length a_{cn}/R (dimensionless crack length), Y_I vs a/R graph was plotted for each loading angle.

Y_I vs a/R graph plotted from the data of Özdoğan's study (2017) can be seen in Figure 5.3 representing the dimensionless stress intensity factor (Y_I) versus dimensionless crack length (a/R) at loading angle of 20º.
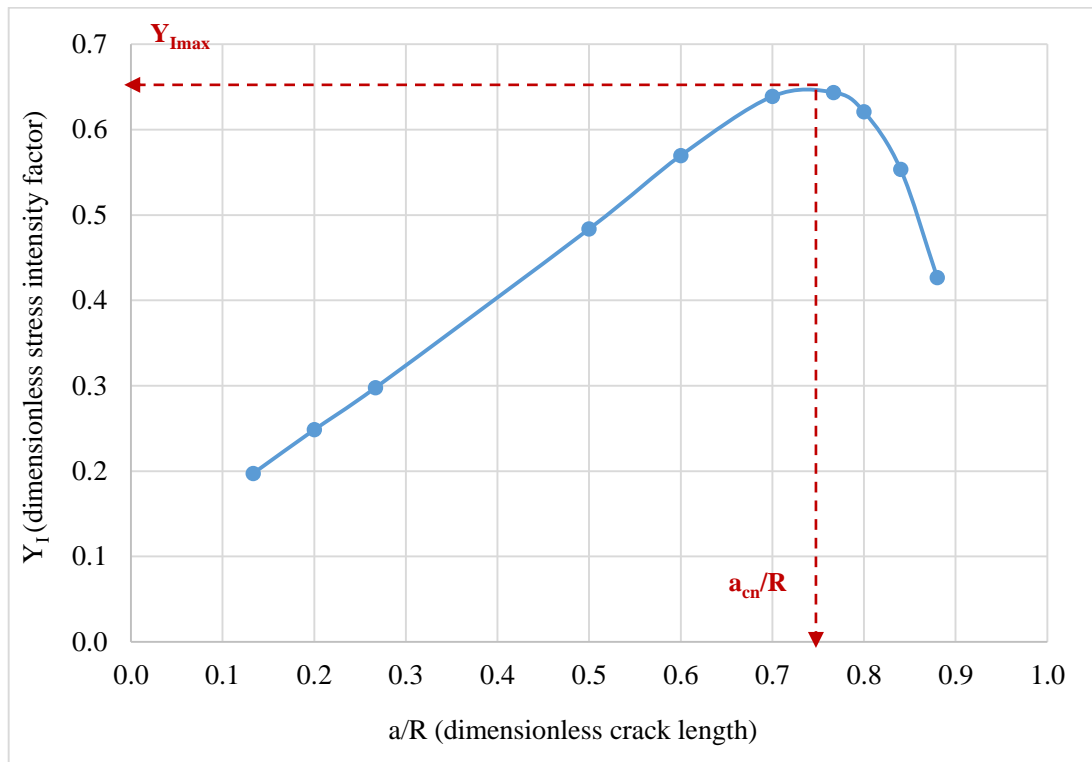
Figure 5.3 Dimensionless stress intensity factor for mode I (Y₁) versus dimensionless crack length (a/R) at loading angle (2α) of 20°

New parametric expressions were derived for Y_{Imax} and critical dimensionless crack length a_{cn}. Özdoğan (2017) derived two formulas. One can be used for finding Y_{Imax} and then K_{Ic}. The other one is used for determining critical crack length based on numerical models.

After finding all the Y_{Imax} values for each loading angle, Y_{Imax} vs $2α$ graphs (e.g Figure 5.4) was plotted. In Figure 5.4, 26º loading angle was marked with a black circle. Because Özdoğan indicated that at 26º loading angle a_{cn} and a_{ce} are detected as the same value.
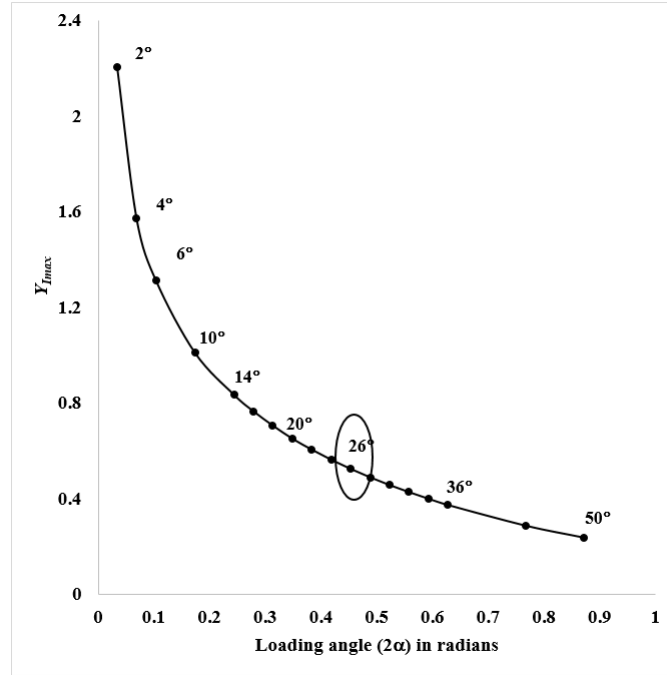
Figure 5.4 The graph of Y_{Imax} *vs loading angle in radians (Özdoğan, 2017)*

Equation 5.2 of Özdoğan (2017) was used here to compute Y_{Imax}:

$$Y_{Imax} = e^{\frac{1.6897+1.4854*(2\alpha)-62.3324*(2\alpha)^2}{1+31.7876*(2\alpha)+4.3693*(2\alpha)^2-2.1703*(2\alpha)^3}} \quad (5.2)$$

In this equation, Y_{Imax} represents maximum mode I dimensionless SIF and 2α is loading angle in radians.

Parametric expression to compute a_{cn}/R vs loading angle (2α) is given in Equation 5.3 (Özdoğan, 2017).

$$\frac{a_{cn}}{R} = 0.9974e^{-0.844(2\alpha)} \quad (5.3)$$

In this equation, 2α is loading angle in radians.

According to the results of the numerical models, the loading angle and crack length were found to be related inversely proportional; when loading angle is equal to zero, the crack length is found to be approximately equal to the radius of the specimen, (Figure 5.5). In Figure 5.5, the red point represents 26° loading angle, which is the proposed loading angle for rock samples having FBD geometry.

71
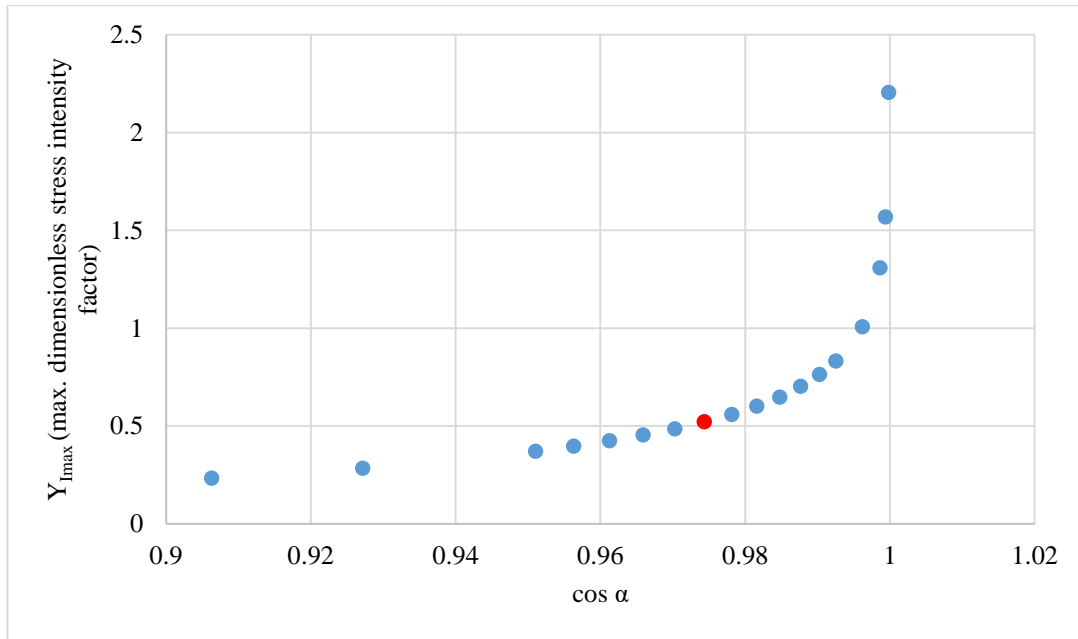
Figure 5.5 Y_{Imax} *vs cos α (modified from the study of Özdoğan (2017))*

This statement was validated by the BDT without curved jaws platens. During these trial tests, the load dropped instantly once, and there was no rise again. In other words, the first load drop and then subsequent rise were not observed. In addition, all of the shotcrete samples were split into two pieces at the load drop and the initial crack dimension was measured to be equal to the sample diameter.

Özdoğan (2017) derived an improved equation to find the mode I fracture toughness (K_{Ic}) for rocks with FBD geometries. After calculating the Y_{Imax} values from Equation 5.2, K_{Ic} values can be found with the help of Equation 5.4, which is derived from Equation 5.1.

$$K_{Ic} = \frac{Y_{Imax}\, P_{min}}{t\, \sqrt{R}} \qquad (5.4)$$

According to Özdoğan (2017), these equations were valid for a wide range of loading angles from $2\alpha = 2° - 50°$. Although these formulas are derived for rock samples, they

72

are used for tests on shotcrete here, since rock and shotcrete have similar internal structures. One of the aim of this study is experimentally validation of these formulas.

5.2. Typical valid and invalid tests

A total of 16 molds were used to obtain the samples with diameters range from 75 mm to 200 mm. Loading angles varied between 20-30 degrees, corresponding to flattened end lengths of *2L*= 15.6-43.5 mm.

A total of 80 valid mode I fracture tests were conducted. Some test results were discarded, since a clear load drop or a theoretically desired central splitting of samples were not observed. It was assured that there were five valid tests for each diameter group and each loading angle group regarding a specific diameter. The number of valid and invalid tests are listed in Table 5.2.

Table 5.2 Completed FBD tests including invalid ones

Diameter (mm)	2α (º)	# of valid tests	# of invalid tests
75	24	5	4
	30	5	4
100	22	5	2
	28	5	2
120	22	5	2
	28	5	1
140	22	5	2
	26	5	1
	28	5	-
160	22	5	1
	24	5	1
	28	5	-
180	22	5	1
	28	5	-
200	20	5	1
	22	5	-

73

In order to check the homogeneity of the samples, each FBD sample was weighed and recorded before the fracture toughness tests. The mean and standard deviation values of the mass values of each valid test sample are given in Table 5.3 below.

Table 5.3 Averages values of mass of the FBD samples

Diameter (mm)	2α (º)	Average mass of valid FBD tests samples (g)
75	24	456 ± 4
	30	452 ± 3
100	22	1085 ± 5
	28	1079 ± 3
120	22	1865 ± 7
	28	1859 ± 5
140	22	3010 ± 8
	26	3005 ± 6
	28	3000 ± 7
160	22	4342± 10
	24	4339 ± 8
	28	4330 ± 9
180	22	6289 ± 14
	28	6279 ± 11
200	20	8605 ± 14
	22	8591 ± 12

As seen in Table 5.3, before beginning the fracture tests all of the samples were check in terms of homogeneity by their mass values.

5.2.1. Valid FBD Tests

The two important indication of a valid FBD tests are a clear load drop in load-vertical displacement graph and crack formation in the center of the sample. A typical and

acceptable load-vertical displacement graph can be seen in Figure 5.6 and in this figure the important parameters such as P_{max} and P_{min} are marked.
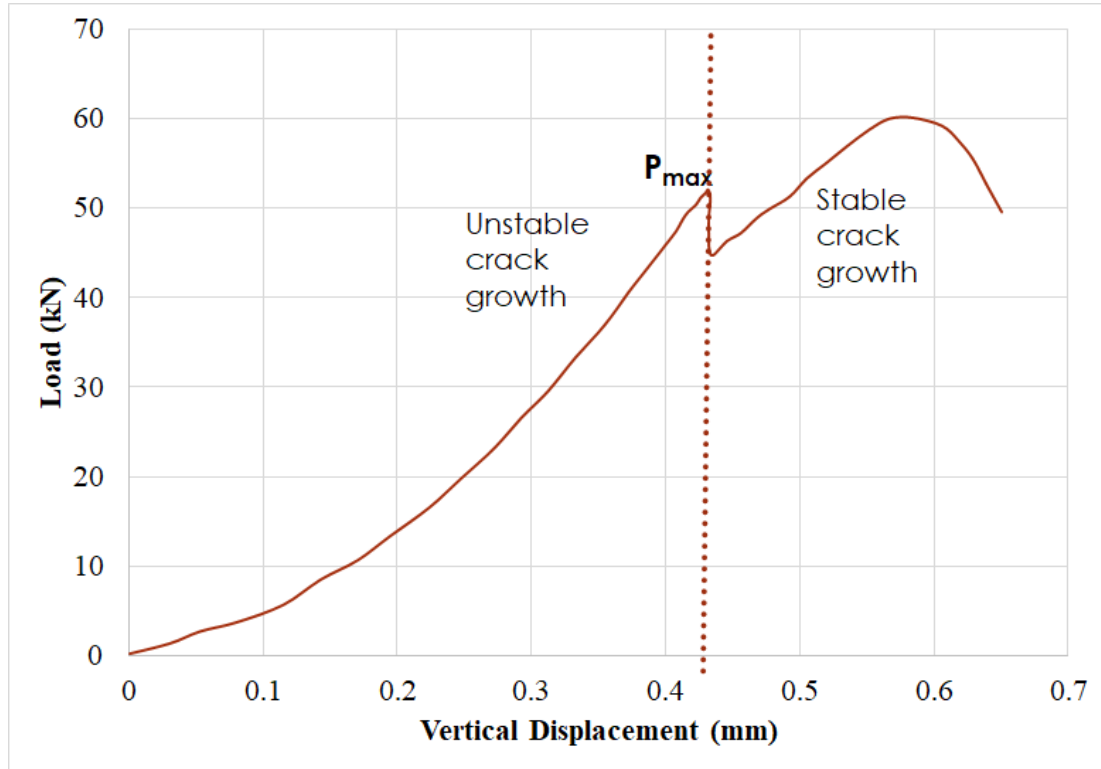
Figure 5.6 A typical and acceptable load-vertical displacement graph of FBD test

As can be seen in Figure 5.6, the FBD specimens were loaded until P_{min} (minimum local load) was observed at the onset of stable crack propagation. The complete failure was observed when the load application was continued to the final state.

In valid FBD tests, after detecting P_{min} values K_{Ic} values are calculated. Since fixed molds were used in the experiments, sample geometries remained the same in each mold. For this reason, Y_{max} value, a function related to the 2α value has not changed and was calculated. Close shot photos were taken before, during, and after the test.

After completing the test experimental crack length (a_{ce}) were measured and compared with the computed crack length (a_{cn}). As fixed molds were used, a_{cn} value, a function related to the 2α value, did not change for each mold.

As an example, the applied procedure of C200-22 coded sample is summarized below. The rest of the results, calculations, related load-vertical displacement graphs and photos of randomly selected samples of each mold before, during, and after test can be seen in Appendix-D, whereas remaining FBD tests photos can be seen in Appendix-E.

Mode I fracture toughness tests were successfully conducted on 5 shotcrete samples with 200 mm diameter and 22° loading angle. For these samples, the flattened length (*2L*) and radius (*R*) are 38.2 mm and 100 mm, respectively. Photos of a sample before, during, and after test can be seen in Figure 5.7.

(a) before test   (b) during test   (c) after test
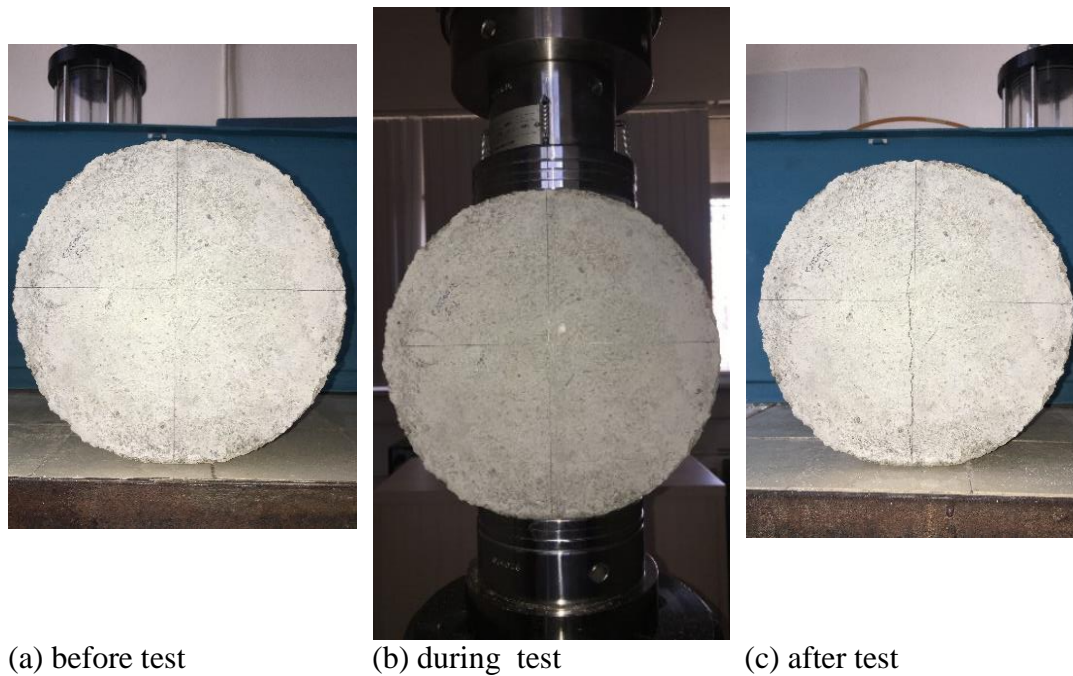
Figure 5.7 C200-22 coded - FBD sample before, during and after the test

P_{min} and K_{Ic} values are listed in Table 5.4. Y_{max} value and 2α value is calculated as 0.604 and 0.384 radians (22°), respectively.

Table 5.4 P_min and K_Ic values of C200-22 coded shotcrete FBD samples

ID	P_{min} (kN)	K_{Ic} (MPa $\sqrt{m}$)
C200-22_s1	104.7	1.50
C200-22_s2	105.4	1.51
C200-22_s3	102.1	1.47
C200-22_s4	101.5	1.46
C200-22_s5	102.8	1.48
Avg. ± Std. Dev.	*103.3±1.7*	*1.48±0.02*

According to Table 5.4, average P_{min} and K_{Ic} values are calculated as 103.3±1.7 kN, and 1.48±0.02 MPa$\sqrt{m}$, respectively. In addition, the load-vertical displacement graph of a randomly selected sample out of 5 samples is given in Figure 5.8.
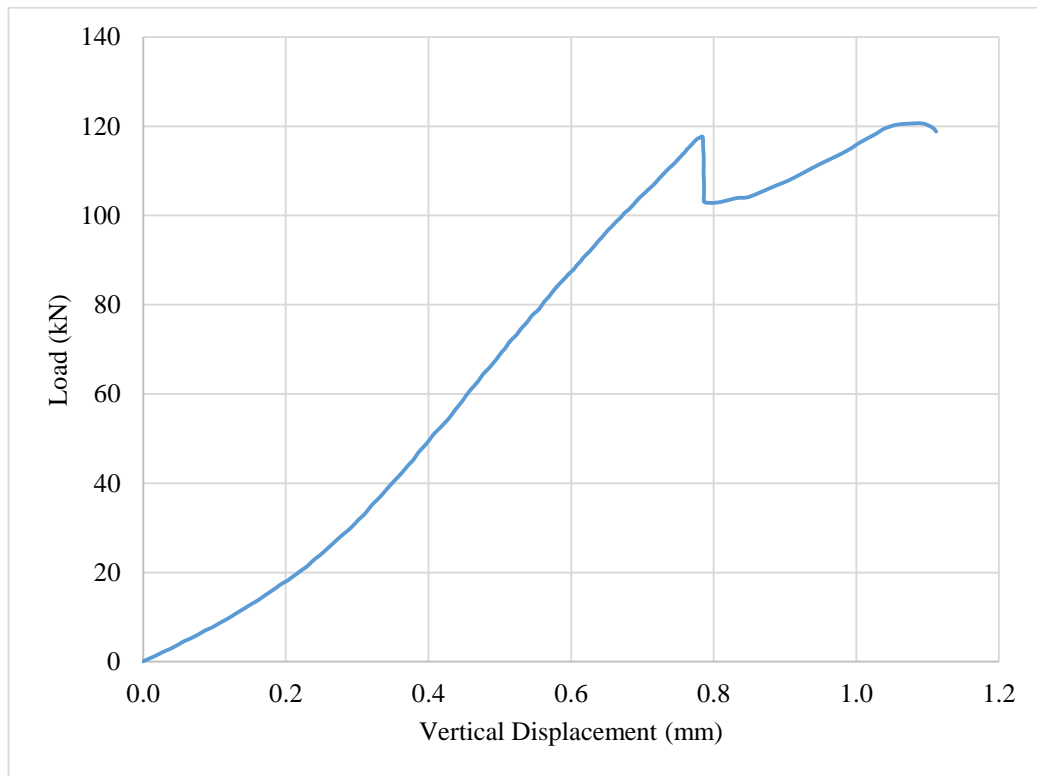
Figure 5.8 Load-vertical displacement graph of C200-22_s5

The measured crack length (a_{ce}) and a_{ce}/R are listed and compared in Table 5.5. The calculated value of a_{cn} is 72.13 mm and a_{cn}/R is 0.721, respectively.

ID	a_{ce} (mm)	a_{ce}/R	$\|a_{ce}\text{-}a_{cn}\|$ (mm)	$\|a_{ce}/R\text{-}a_{cn}/R\|$
C200-22_s1	72.16	0.722	0.03	0.000
C200-22_s2	74.25	0.743	2.12	0.021
C200-22_s3	73.02	0.730	0.89	0.009
C200-22_s4	74.59	0.746	2.46	0.025
C200-22_s5	72.81	0.728	0.68	0.007
Avg. ± Std. Dev.	*73.37±1.02*	*0.734±0.010*	*1.23±1.02*	*0.012±0.010*

As it is seen from Table 5.5, the average absolute difference between $\|a_{ce}\text{-}a_{cn}\|$ is 1.23±1.02 mm and the absolute difference between a_{ce}/R and a_{cn}/R is 0.012±0.010.

5.2.2. Invalid FBD tests and their reasons

When performing experimental work, it is noticed that the expected sudden load drop, which is the characteristic behaviour of samples on FBD tests, cannot be observed in all of the tests. Examples of invalid tests and their possible reasons are explained below.

As it can be seen from Table 5.2, the number of invalid tests decreased as the specimen size increased. One of the possible reasons is that it was easier to pour the shotcrete mixture with aimed consistency into the large size molds by using the same mixture under the same environmental conditions. The demolding process of samples with larger dimensions was easier than small-sized samples due to the higher thickness of large size molds.

For the sample preparation, 3D molds produced by 3D printer were used. Therefore, geometries of the samples did not have major defects. There was no inclination or roughness of the flattened ends of the samples, or anything that would disrupt the parallel orientation of the flattened ends with respect to each other. Generally, the problem is rather related with the sample preparation. Small samples, especially

specimen having 75 mm diameter were found to be the most difficult to prepare due to the limited space in small-size 3D molds.

a. Two-stage load drop case

The most important issue during tests was to catch the drop in the load displacement graph. Sometimes, it was noticed that there was another drop after the first one was formed. An example of the resulting load displacement graph for this case is given in Figure 5.9.
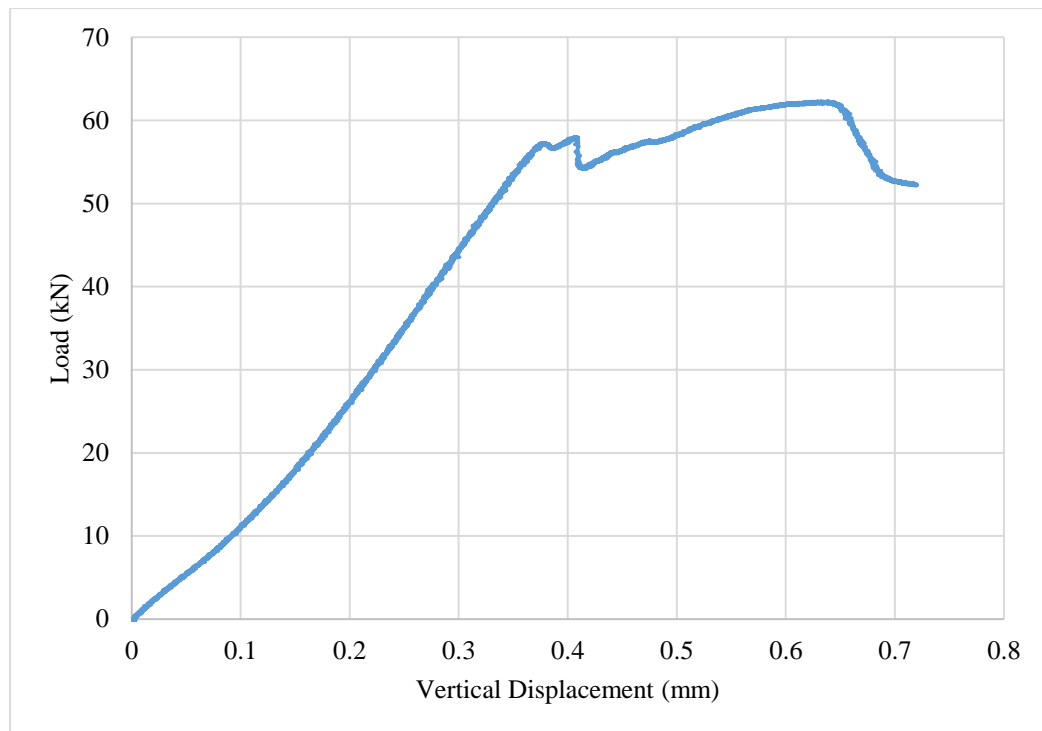
Figure 5.9 Load-vertical displacement graph for two-stage load drop case

The reason of this two-stage load drop is the presence of secondary cracks. The first crack does not cause sufficient energy release and thus a clear load drop cannot be identified. Some secondary cracks form and a second load drop is observed in the load-displacement graph. Another reason of this two-stage load drop is that there might be cracks opened at different times on the two diametric surfaces of the samples having higher thickness values.

79

b. No load drop case

Second type of invalid test is that the expected load drop after the peak is not clearly observed. An example graph of this situation can be seen in Figure 5.10. The reason for this case is that the sample is more porous than the targeted state, so it cannot show the behavior of typical real shotcrete mixture state (Figure 5.11).
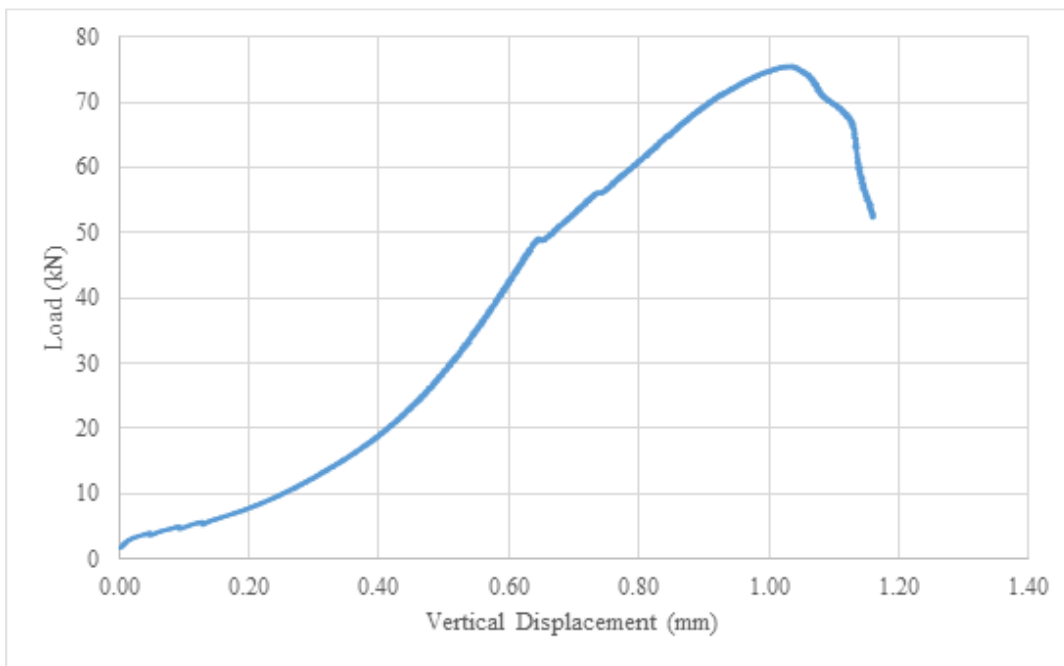
Figure 5.10 Load-vertical displacement graph for no load drop case

One of the reasons may be the over trapped presence of small aggregate fragments at the junctions of the flattened ends and the curved parts of the sample. In the load-displacement graph shown in Figure 5.10 a couple of deviations from the smooth load displacement behavior are seen before the peak load. For some little parts of the curves, load seems to remain constant as the displacement increases along horizontal parts.

Figure 5.11 Example of shotcrete specimen (a) with porous structure and (b) with targeted normal structure

Clear load drop cannot be observed due to the uneven distribution of aggregate pieces in rather plastic cement binder. It is possible that unevenly distributed aggregate accumulations are penetrating and seating in the plastic binder. Summarizing, brittle state of aggregate parts dominate the load displacement behavior, and thus no clear load drop and P_{min} can be detected after the peak load.

CHAPTER 6

EXPERIMENTAL RESULTS AND DISCUSSION

Mode I fracture toughness tests were conducted on cylindrical shotcrete samples having FBD geometries with diameters of 75 mm, 100 mm, 120 mm, 140 mm, 160 mm, 180 mm, and 200 mm. The specimens have different loading angles varying between 20°-30° corresponding to flat end/radius ratios of L/R=0.17-0.26. These specimens were loaded until a local minimum load P_{min} was observed at the onset of stable crack propagation. The complete failure was achieved by continuing the load application to the final state in which unstable crack propagation reaches the flat boundaries of the FBD specimens. Close shot photos were taken on both specimen faces to detect the experimentally observed crack length a_{ce} at the onset of stable crack propagation. Experimentally measured crack length a_{ce} at P_{min} was compared to the numerically estimated crack length a_{cn} at P_{min}.

6.1. Summary of Experimental Results

Overall results of the fracture toughness tests conducted with specimens of FBD geometry having seven different diameters and sixteen loading angle combinations are listed in Table 6.1. In the table, K_{Ic} results of seven different diameter groups are summarized as average values and used for analyzing the size effect on mode I fracture toughness. Mode I fracture toughness, K_{Ic}, values are also evaluated as groups and summarized according to the loading angle. The aim in this practice is to analyze the variation of fracture toughness with the loading angle in scope of the boundary influence investigations. As loading angle gets greater, crack tip at P_{min} is closer to the loaded ends and adjacent free boundaries. High stress gradients in this case may result in specimen geometry dependent variations for K_{Ic} measurements.

Table 6.1 Average Flattened Brazilian Disc (FBD) tests results

Sample Code	Diameter D (mm)	Loading Angle 2α (°)	Max. Dimensionless Stress Intensity Factor Y_{Imax}	Min. Local Load P_{min} (kN)	Fracture Toughness K_{Ic} (MPa√m)
C75-24	75	24	0.561	18.1	1.02
C75-30		30	0.454	20.9	0.96
C100-22	100	22	0.604	28.6	1.15
C100-28		28	0.487	34.3	1.11
C120-22	120	22	0.604	40.5	1.23
C120-28		28	0.487	45.9	1.21
C140-22		22	0.604	55.6	1.34
C140-26	140	26	0.522	63.1	1.31
C140-28		28	0.487	63.7	1.24
C160-22		22	0.604	69.5	1.42
C160-24	160	24	0.561	72.8	1.38
C160-28		28	0.487	81.4	1.32
C180-22	180	22	0.604	86.9	1.46
C180-28		28	0.487	101.7	1.37
C200-20	200	20	0.651	96.9	1.50
C200-22		22	0.604	103.3	1.48

According to the local minimum load P_{min} and maximum mode I dimensionless SIF (Y_{Imax}) presented in Table 6.1, mode I fracture toughness values can be examined more clearly and in detail.

P_{min} and Y_{Imax} values are grouped according to the seven different diameter values. The number of specimens for each group is five, in other words, the average values are calculated from five valid test results. Table 6.1 contains only the average values calculated based on the loading angle in order to determine the effect of the sample

diameter on Mode I fracture toughness value. The details of the loading angle investigation based on the overall results are listed in Table 6.2, where the total number of tests accepted as valid are also given.

Table 6.2 Summary of the results

Diameter D (mm)	Loading Angle 2α (º)	# tests	Fracture Toughness K_{Ic} (MPa√m)	
			Regarding 2α (º)	Regardless 2α (º)
75	24	5	1.02±0.07	0.99±0.06
	30	5	0.96±0.06	
100	22	5	1.15±0.05	1.13±0.06
	28	5	1.11±0.06	
120	22	5	1.23±0.05	1.21±0.05
	28	5	1.20±0.03	
140	22	5	1.34±0.06	
	26	5	1.31±0.06	1.30±0.06
	28	5	1.24±0.03	
160	22	5	1.42±0.04	
	24	5	1.38±0.05	1.37±0.05
	28	5	1.32±0.03	
180	22	5	1.46±0.05	1.42±0.06
	28	5	1.37±0.01	
200	20	5	1.50±0.03	1.49±0.03
	22	5	1.48±0.02	

The first noticeable result in the summary tables is that the value of the mode I fracture toughness increases as the specimen diameter increases. The initial and final points of the critical crack length on the smaller samples is near to the flattened ends and the fracture process zone (FPZ) around and in front of the crack tip become more confined so fracture toughness values increase with increasing diameter.

As explained in the previous chapters, Y_{Imax} is calculated from Equation 5.2, which is a function of *2α* only and without taking the size of the specimen into account.

Therefore, the Y_{Imax} values of the specimen geometries with the same loading angle are the same.

The numerically computed a_{cn} values and experimentally measured a_{ce} values are analyzed and presented depending on the observed variations in K_{Ic} in the previous chapters. Based on these results, a_{ce}/R and a_{cn}/R and the absolute difference between them $(|a_{ce}/R-a_{cn}/R|)$ are calculated. The comparison between the average critical crack length values is performed in terms of a_{ce}/R and a_{cn}/R values and summarized in Table 6.3. The average values are again calculated for five different specimens of valid tests.

Table 6.3 The average initial crack length comparison

Sample Code	a_{cn}/R	a_{ce}/R	$\|a_{ce}/R-a_{cn}/R\|$	
			Regarding 2α	Regardless 2α
C75-24	0.70	0.61	0.094	0.097
C75-30	0.64	0.54	0.099	
C100-22	0.72	0.78	0.060	0.062
C100-28	0.66	0.60	0.063	
C120-22	0.72	0.76	0.042	0.040
C120-28	0.66	0.63	0.038	
C140-22	0.72	0.75	0.027	
C140-26	0.68	0.65	0.028	0.028
C140-28	0.66	0.69	0.030	
C160-22	0.72	0.74	0.021	
C160-24	0.70	0.69	0.022	0.022
C160-28	0.66	0.68	0.023	
C180-22	0.72	0.73	0.016	0.017
C180-28	0.66	0.68	0.018	
C200-20	0.74	0.76	0.014	0.013
C200-22	0.72	0.73	0.012	

As it can be seen in Table 6.3, the average a_{ce}/R values are randomly changing while the sample diameter is increasing. However, the difference between measured and computed critical crack length is decreasing while the diameter of the shotcrete sample is increasing. The reason of this decrease is that the load can be distributed more uniformly, since when the loading angle is increased, the flattened area, where the load is applied is also increased. In the samples with small diameter, more energy is produced to generate the initial crack length and therefore a much larger critical crack length than computed was observed. So, the difference between critical crack lengths decreases as the diameter increases.

In Figure 6.1, C200-22_s5 coded sample is seen during the initial crack length generation moment. The fracture started from the center of the specimen as expected and proceeded towards the middle of the flat ends.

Figure 6.1 C200-22_s5 coded shotcrete sample during fracture toughness test

In addition, as the diameter of the sample increased, the success rate of the experiments increased significantly as well the number of invalid tests decreased. As it can be seen in Figure 6.1 in detail, during the tests with the shotcrete samples with larger diameters, it was observed that the fracture generates in the center and is almost ideal. Therefore, as the sample diameters increased, the difference between the initial crack length (a_{ce}) captured during the test and the initial crack length (a_{cn}) values calculated from Equation 5.3 decreased.

6.2. Graphical Representation and Evaluation of the Test Results

Graphical representation and evaluation of the test results are mainly focused on the load drop variation, crack length investigation, effect of loading angle, boundary influence issue, and size effect.

6.2.1. Load drop variation

The specimens are loaded until a local minimum load, P_{min}, is observed at the onset of stable crack propagation. The first peak load, P_{max}, that is observed just before the local minimum load P_{min} is recorded and the difference between these two loads is called ΔP (P_{max}-P_{min}).

In order to investigate any possible variation of these load drops with specimen size, load drops were converted to the applied stress, $\Delta\sigma_a$, at the flattened ends by dividing them by the area of the ends. This way, a fair comparison basis is set to take the increasing peak loads with increasing diameters.

The relationship between the average of $\Delta\sigma_a=\Delta P/(2L*t)$ values and specimen size is presented in Figure 6.2 regardless of 2α.
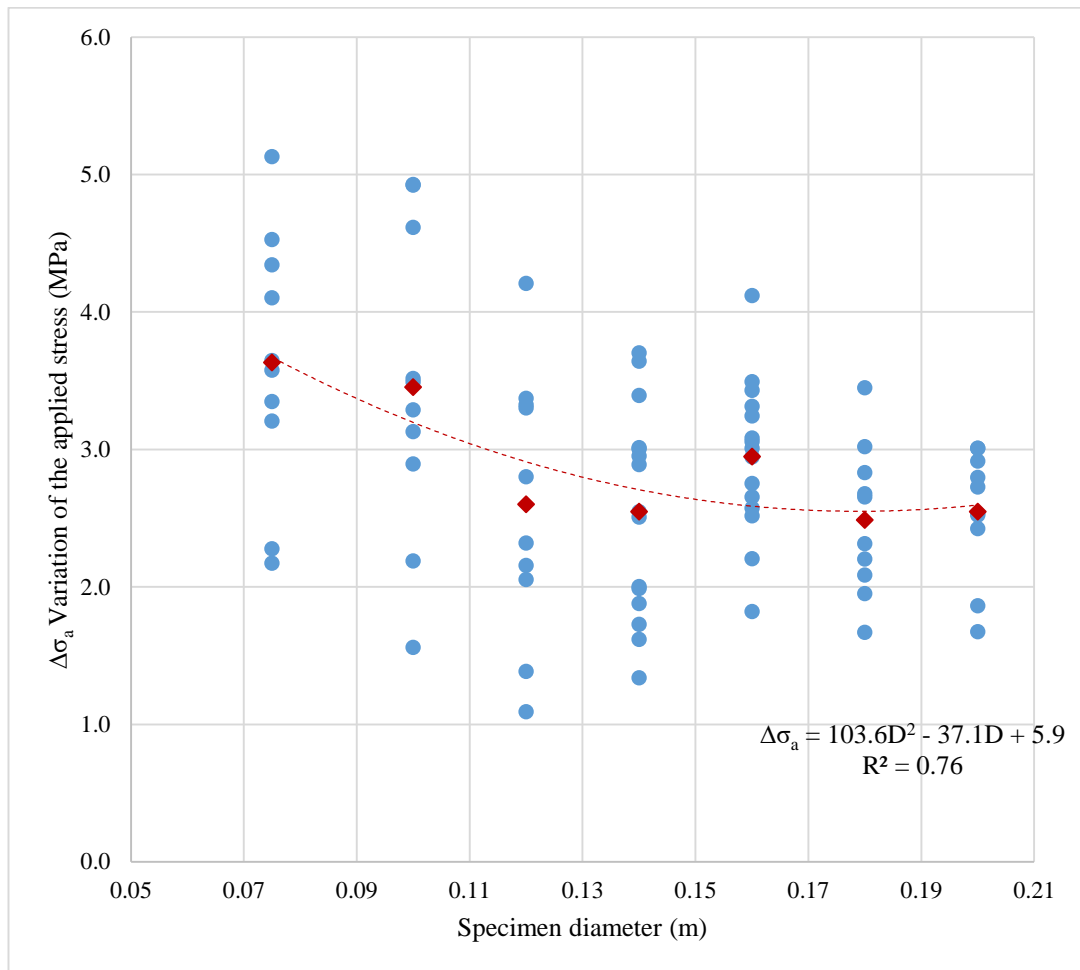
Figure 6.2 Average Δσ_a vs. specimen diameter (regardless of 2α)

The blue dots represent the individual results of all the experiments and the red dots represent the average values calculated regardless loading angle. The trend line and equation are generated for the average values (red dots). According to Figure 6.2, $Δσ_a$ values decrease with increasing specimen diameter. As the diameter of the sample increases, the area where the load is applied increases. At the same time, the load that the sample withstands does increase. In other words, the two parameters, which are used for calculating $Δσ_a$ values, increased. Therefore, $Δσ_a$ is expected to remain constant and/or close to constant, but it has shown a declining trend since the flattened area where the load is applied increases more than $ΔP$. Since the area is proportional to the L^2, its value increases more than $ΔP$.

6.2.2. Investigation of crack length

The critical initial crack length values were compared between experimentally determined values and computed values. The absolute differences between *ace/R* and *acn/R* values (*|ace/R-acn/R|*) vs. specimen diameter graph are plotted in Figure 6.3.

The equation shown on the plot:

$$|ac_e/R-ac_n/R| = 820.38 \, D^{-2.078}$$
$$R^2 = 0.99$$
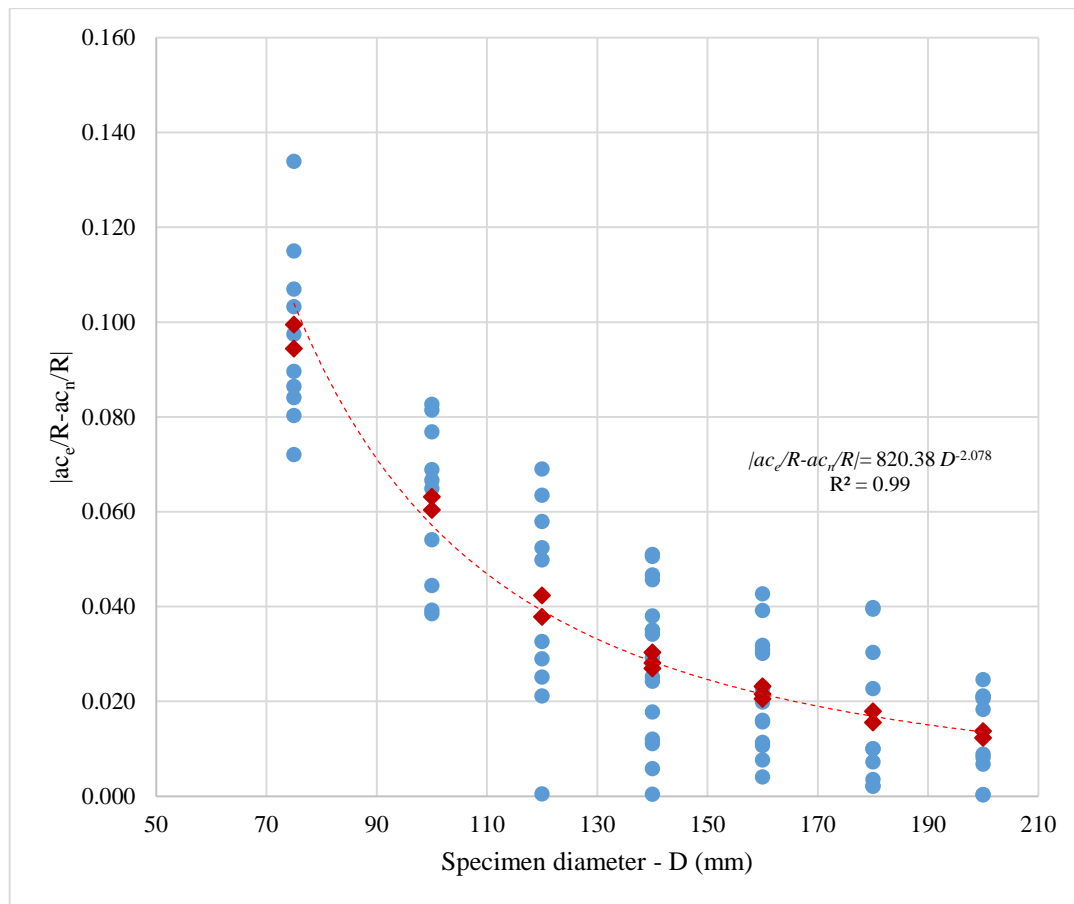
Figure 6.3 |a_ce/R-a_cn/R| vs specimen diameter

Again, the blue dots represent individual results whereas the red dots represent average values of each sample group. The trend line and related equation are based on the average values.

As it can be seen from Figure 6.3, the absolute difference between a_{ce}/R and a_{cn}/R values (*|a_ce/R-a_cn/R|*) decreases while specimen diameter increases. As mentioned earlier, the tests conducted on specimens having comparably larger diameter were

90

more precise than smaller diameter. Therefore, the experimentally determined initial crack length values were close to the calculated initial crack length values. It is seen that as sample diameter increases, the differences between measured and computed values become negligible and the measured values are detected very close to the calculated values.

In order to simplify Figure 6.3 and to see the specimen diameter effect on initial crack length calculation, this graph was modified by not considering the 2α situation as seen in Figure 6.4.
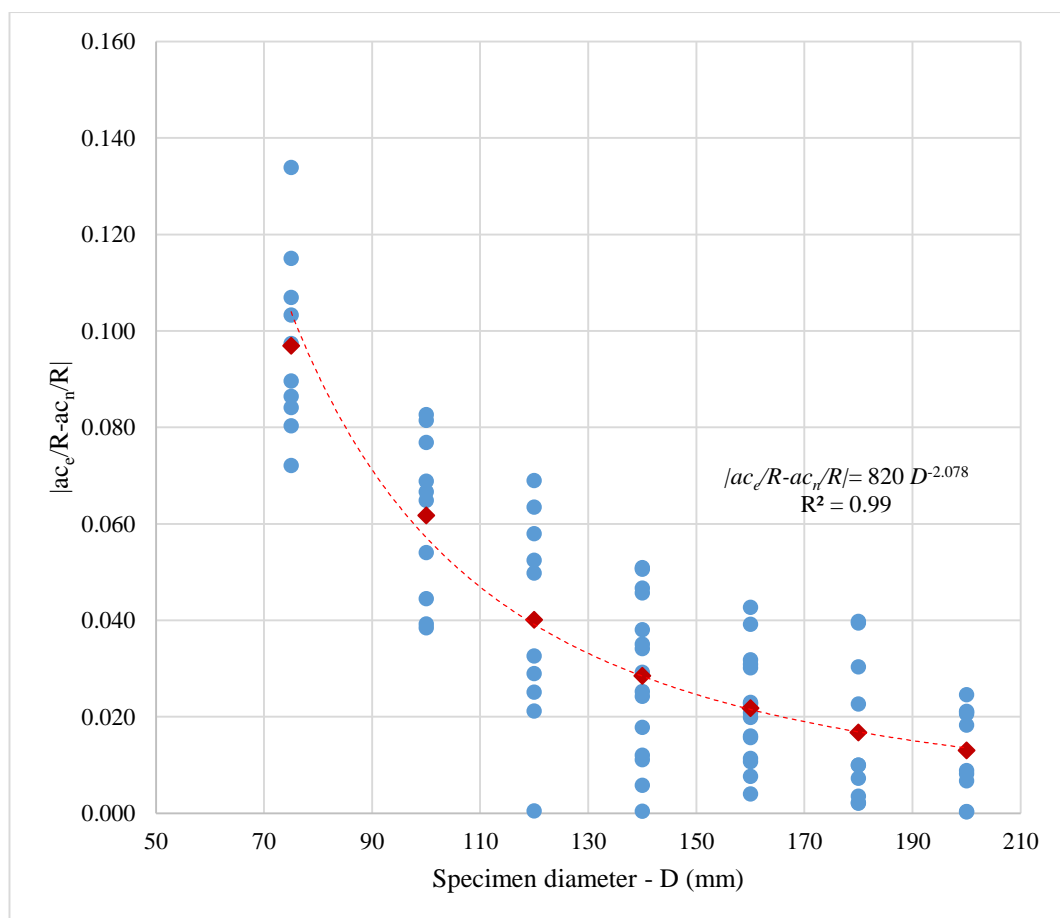
Figure 6.4 $|ac_{ce}/R-a_{cn}/R|$ vs specimen diameter (regardless 2α)

Unlike Figure 6.3, in Figure 6.4 the red dots represent average values calculated regardless the loading angle whereas the blue dots presents individual results again.

91

As sample diameter increased, the difference between calculated and measured initial crack length decreased.

Figure 6.4 can be interpreted as the difference decreasing extremely, about 10 times, between the small diameter and the largest diameter sample groups. Moreover, the deviation of the individual results decrease on samples having 160 mm or larger than 160 mm diameter. In fact, the smaller deviation is detected on samples having the largest diameter as 200 mm. From this point of view, samples having 160 mm diameter are considered to be the most appropriate geometry for experiments.

6.2.3. Effect of loading angle

In order to evaluate the impact of loading angle on size effect analysis, K_{Ic} vs specimen diameter graph is plotted both regarding and regardless of 2α case. The K_{Ic} vs. specimen diameter graph with regarding 2α case can be seen in Figure 6.5.
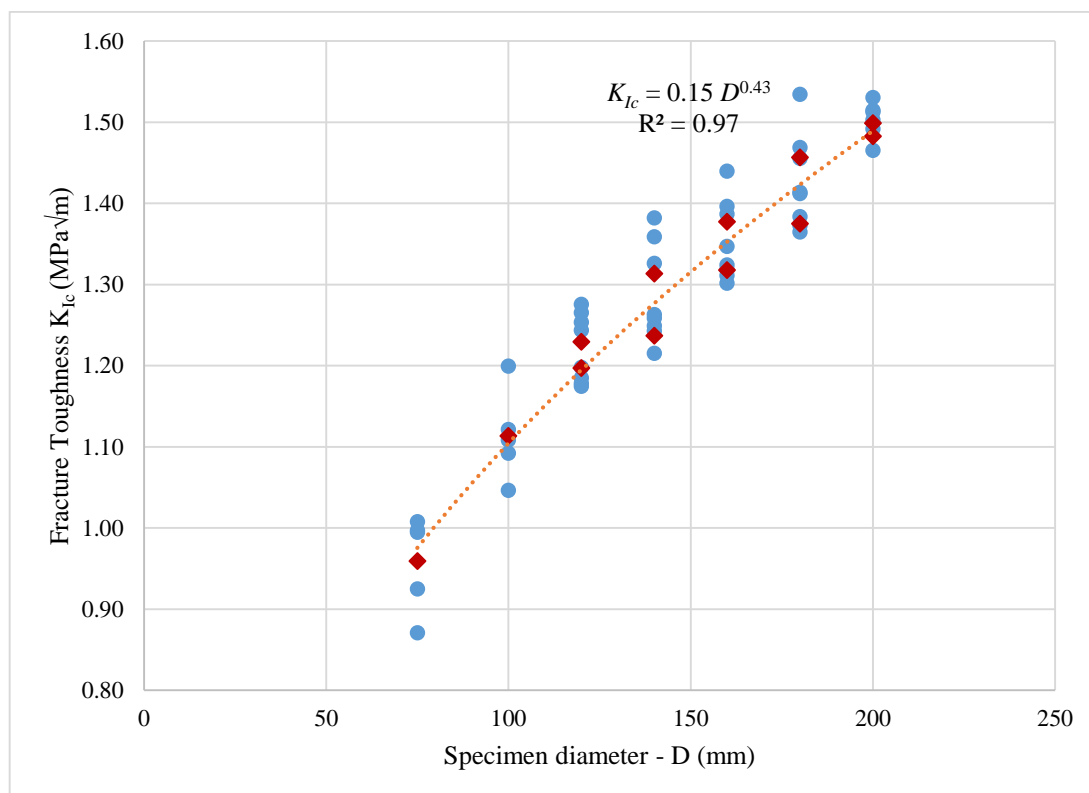
Figure 6.5 K_{Ic} vs specimen diameter graph (regarding 2α)

Figure 6.5 represents the general view of the overall test results. The blue dots represent the K_{Ic} values of each molded shotcrete specimen whereas the red dots represent the average values regarding *2α*. The trend line and equation represent the average values. As it can be seen from the figure, K_{Ic} values increased with increasing specimen diameter. From this graph, it is seen that the change in specimen dimensions (both in diameter and loading angle) affected the FBD test results.

In order to investigate the effect caused by loading angle, the K_{Ic} vs. specimen diameter graph regardless *2α* was plotted and can be seen in Figure 6.6. In this figure, the red dots represent average values regardless *2α*. In another words, red dots represent the average K_{Ic} values of each sample with the same diameter, regardless their loading angles.

Figure 6.6 K_{Ic} vs specimen diameter graph (regardless 2α)

While examining the equation created for Figure 6.5, there was an exponential relationship between the K_{Ic} values and the sample diameter in the equation with the highest R-square value. As for Figure 6.6, the R-square value has reached a more ideal

level than the graph in Figure 6.5, this time the relationship between the two parameters is defined logarithmically. The increasing tendency seen with the increasing diameter slightly decreased compared to Figure 6.5. However, since the R-square value of the equation given in Figure 6.6 is 0.99, it represented the general behavior more appropriately.

For all experiments, K_{Ic} values vs. *cos α* graph are presented in Figure 6.7. Again in this figure, the blue dots represent individual results and the red dots represent the average values regarding specimen diameter. Therefore, there are more than one average value in some loading angles. For example, there are five different average values (five red dots) at 28° due to the five different diameter values.
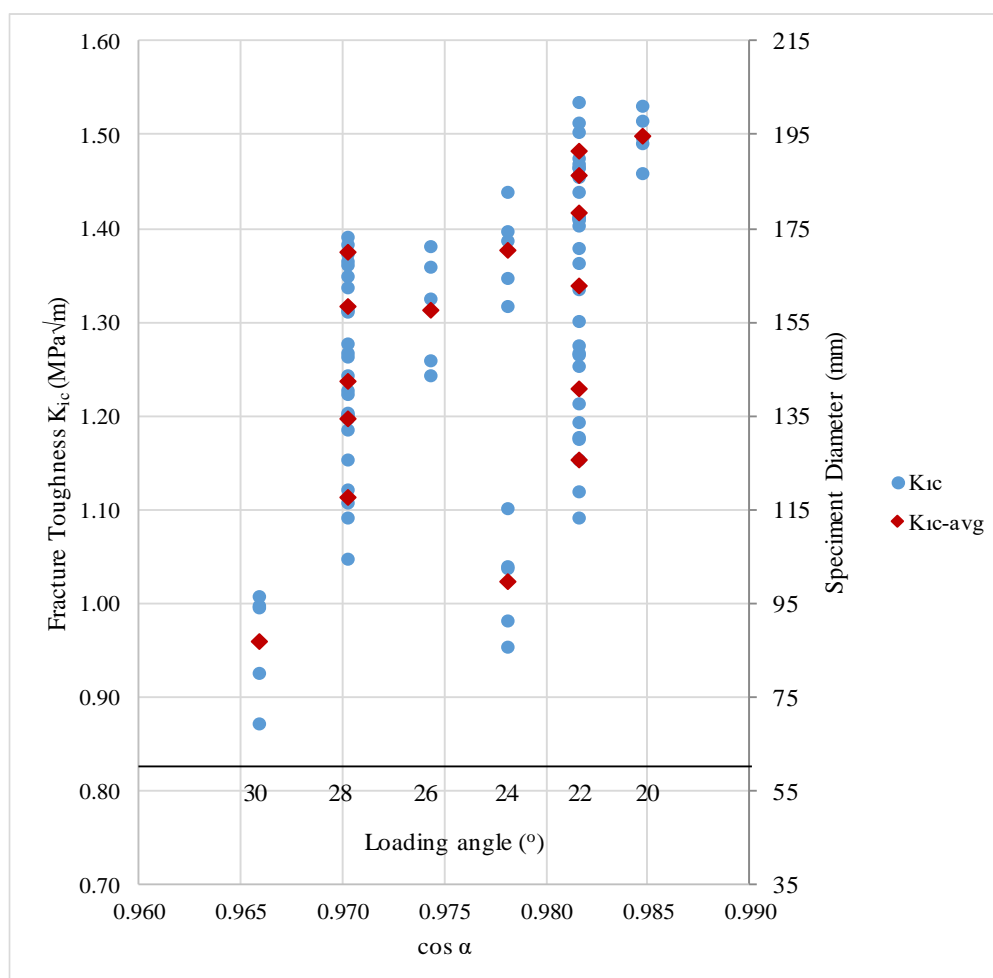
Figure 6.7 Fracture toughness K_{Ic} vs cos α graph

As it can be seen from Figure 6.7, K_{Ic} values increased with increasing specimen diameter at the same loading angle. A secondary axis was added to make this interpretation easier to understand from the graph. So the effect of the changing size of the specimen dimension can easily be detected from Figure 6.7.

6.2.4. Boundary influence issue

The average K_{Ic} values changes at the same diameter with different loading angles are examined and plotted in Figure 6.8.

Specimen diameter D (mm)	75	100	120	140	160	180	200
■ @ Lowest angle	1.02	1.15	1.23	1.34	1.42	1.46	1.50
■ @ Highest angle	0.96	1.11	1.20	1.24	1.32	1.37	1.48
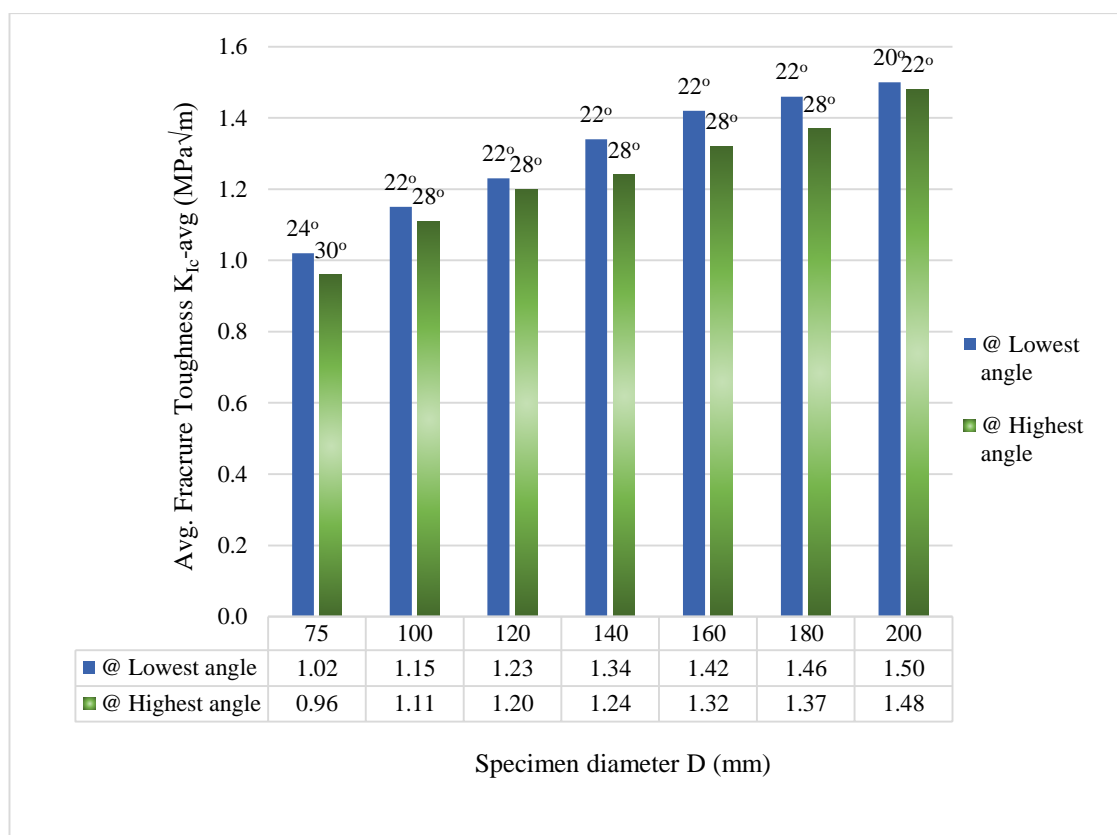
Figure 6.8 Average K$_{Ic}$ values changes at the same diameter with different loading angle

As it can be seen from Figure 6.8, K_{Ic} values decreased with increasing loading angle of the specimen having same diameter. This phenomenon is called boundary influence issue. This boundary influence issue is another problem with the fracture toughness testing on limited size samples. By increasing the loading angle, flat loaded ends get closer to the initial crack tip at the onset of stable propagation. Adjacent to the loaded

ends there are traction free boundaries of curved specimen geometry. Highly stressed loaded ends and immediate free curved boundary combination may affect the fracture toughness results for the specimen geometries having crack tips close to these high stress gradient regions.

6.2.5. Investigation of size effect

For the 16 different 3D molds, there are some specimen having different diameters but same loading angles. For example, there are specimen having five different diameters as 100 mm, 120 mm, 140 mm, 160 mm, and 180 mm at 28° loading angle. Additionally, there are some specimen having six different diameters as 100 mm, 120 mm, 140 mm, 160 mm, 180 mm, and 200 mm at 22° loading angle. According to these molds, the change of mode I fracture toughness values are examined in detail to have a closer look on the size effect phenomenon. The average K_{Ic} values of specimen having different diameter but 28° loading angle are represented in Figure 6.9.
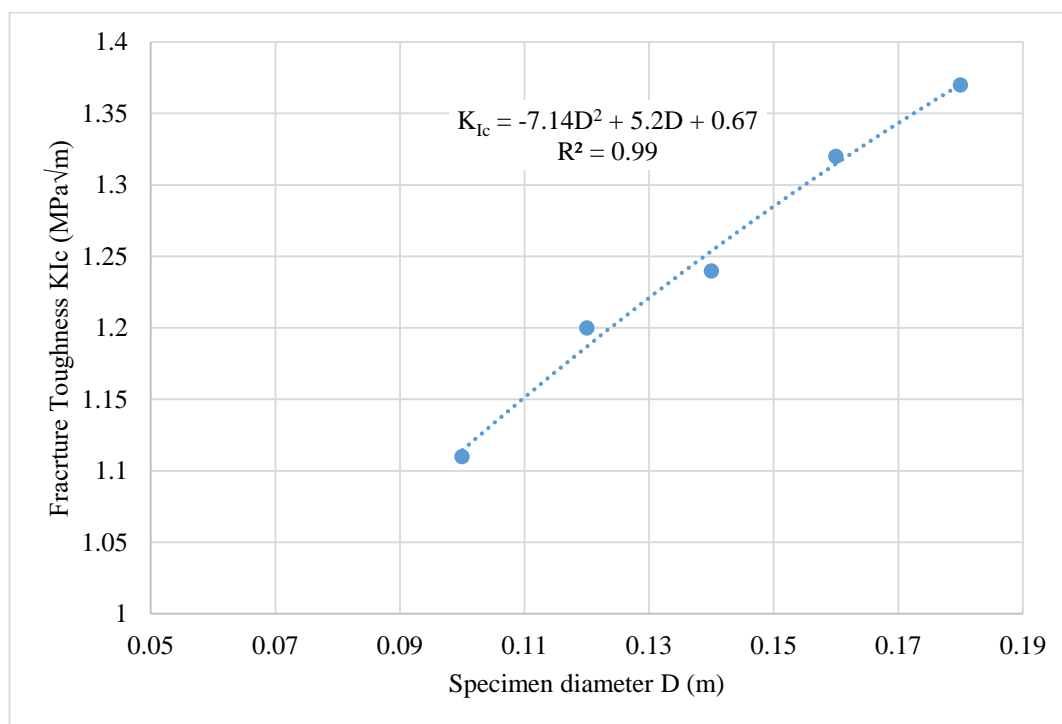
Figure 6.9 Average K_{Ic} *values vs specimen diameter at 28° loading angle*

The size effect phenomenon can be clearly observed from Figure 6.9. At the same loading angle (28º), mode I fracture toughness values are increasing with the increasing specimen diameter. According to the average values plotted in Figure 6.9, the size effect can be basically calculated as 23.4% ($K_{Ic,max}/K_{Ic,min}$) = 1.37/1.11 = 1.234) on the specimen having different diameter at 28º loading angle. In order to investigate the size effect on the relationship between K_{Ic} values and crack length, K_{Ic} vs. R/a_{ce} graph is shown in Figure 6.10.
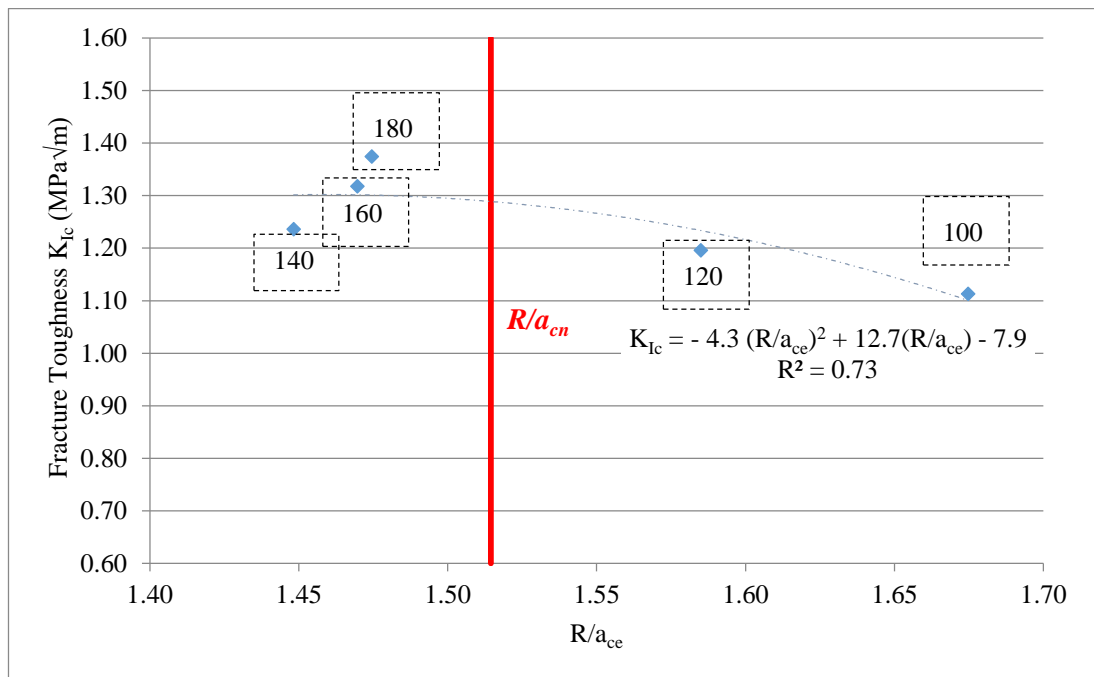
Figure 6.10 Average K_{Ic} *values vs* R/a_{ce} *at 28º loading angle*

In Figure 6.10, the blue dots represent the average K_{Ic} values whereas the vertical red line represents R/a_{cn} values calculated from the equations listed in Chapter 5. The numbers given in the dashed boxes are the sample diameters. As it can be seen from Figure 6.10, K_{Ic} values decrease with increasing R/a_{ce} values at 28º loading angle. When the R/a_{ce} values measured after the experiment are higher than R/a_{cn} values, it can be concluded that the experimentally measured crack length a_{ce} is smaller than the numerically calculated initial crack length a_{cn}, so there is not enough energy release during the crack formation. But when R/a_{ce} values are higher than R/a_{cn} values, it

97

means that a_{ce} is higher than a_{cn}. The average toughness values of the samples with only 140 mm and 160 mm diameter approached the red line. Test results of the samples with small diameters seem to have moved away from the required value. During the experiments, it was determined that as the diameter of the samples increased, the number of valid experiments increased. Therefore, when the samples having a loading angle of 28° were examined, it was found that the diameters of 140 mm, 160 mm, and 180 mm were especially suitable geometries for experiments.

For comparison purposes, the average K_{Ic} values of specimens having different diameters but 22° loading angle are plotted in Figure 6.11.
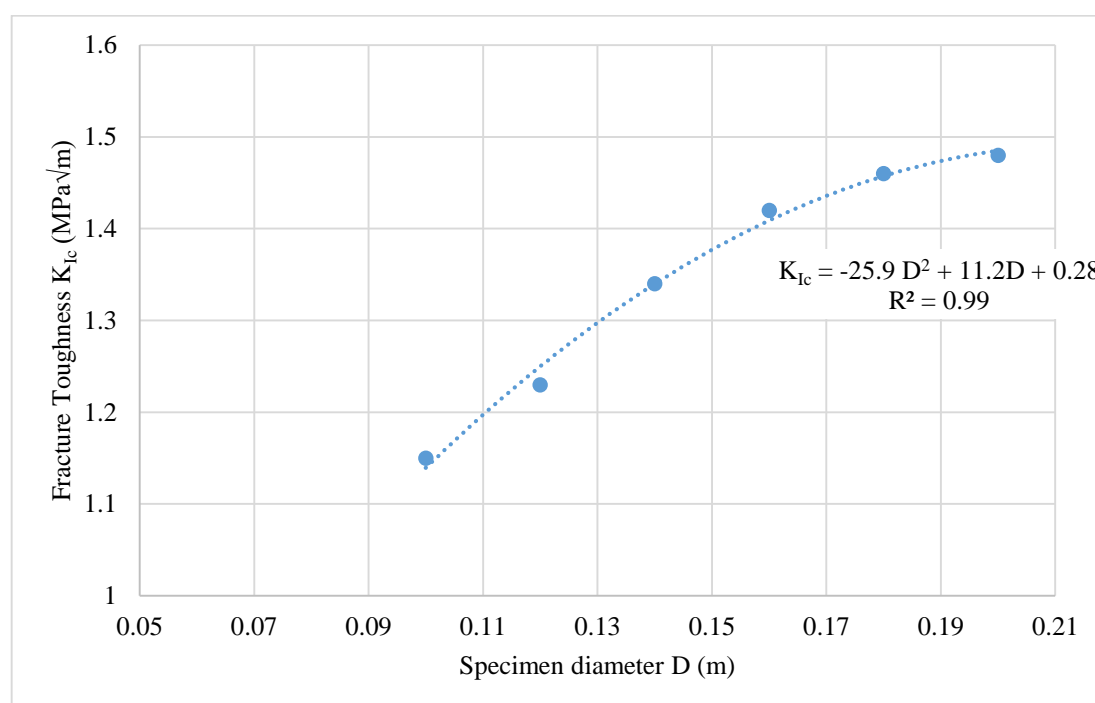
Figure 6.11 Average K_{Ic} *values vs specimen diameter at 22° loading angle*

According to the average values plotted in Figure 6.11, the size effect can be basically calculated as 28.7% ($K_{Ic,max}/K_{Ic,min}$ = 1.48/1.15=1.287) on the specimen having 22° loading angle. When this size effect ratio is compared with the previous size effect ratio valid for 28° loading angle case, it can be concluded that the size effect ratio increases with the decreasing loading angle.

For a detailed investigation, average K_{Ic} vs. R/a_{ce} graph of samples having 22° loading angle is plotted (Figure 6.12) and in this graph the blue dots represent the average K_{Ic} values whereas the red line represents R/a_{cn} values calculated from the equations listed in Chapter 5. Like previous application the diameter of samples are written in the dashed boxes on the graph.
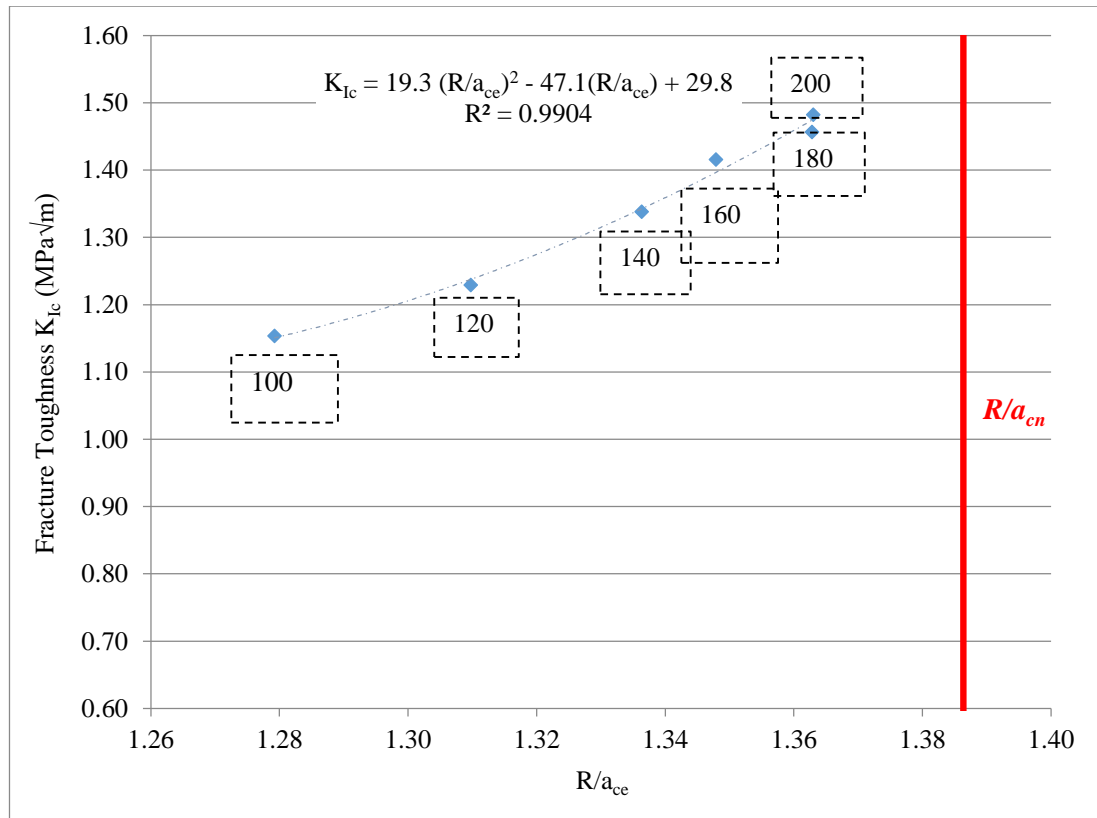
Figure 6.12 Average K_{Ic} *values vs* R/a_{ce} *at 22° loading angle*

In Figure 6.12, the blue dots represent the average K_{Ic} values whereas the red line represents R/a_{cn} values calculated from the equations listed in Chapter 5. As it can be seen from Figure 6.12, K_{Ic} values increase with increasing R/a_{ce} values at 22° loading angle. This is also highlight the fact that the experimentally found initial crack length is greater than the calculated initial crack length. However, the differences between the calculated and experimentally found values decrease with increasing diameters.

The reason behind this trend is that there is no boundary influence issue. Since the loading angle value is small (22°), the distance of the flattened area where the load is applied to the center of the sample is more than the samples with large diameters. Therefore, since the boundary influence issue is low compared to large diameters, the experimentally found crack length values are higher than the calculated values.

When the sample diameters were examined, the fracture toughness difference between 180 mm and 200 mm was lower than the small diameters. The trend of the increase of the fracture toughness in smaller diameters is higher. For this reason, it has been found that larger diameters (180 mm, 200 mm) are more suitable for experiments by means of geometry with 22° loading angle.

The size effect study made so far was performed on samples having 22° and 28° loading angle as the number of tests performed on these samples were sufficient to create an appropriate graphical representation. In order to benefit from the results of the remaining samples, loading angles were combined into two groups as 20-25° and 26-30°. The reason of the distinction between the different loading angles is based on the difficulties experienced during the specimen preparation stage.

Average K_{Ic} values vs specimen diameter at 20-25° (small loading angle range) loading angle and 26-30° (large loading angle range) are plotted in Figure 6.13.

According to the average values plotted in Figure 6.13, the size effect ratio can be calculated as 47.1% ($K_{Ic,max}/K_{Ic,min}$ = 1.50/1.02=1.471) for the specimen group having 20-25° loading angle, and as 42.7% ($K_{Ic,max}/K_{Ic,min}$ = 1.37/0.96=1.427) for the specimen group having 26-30° loading angle. The size effect ratio decreases with increasing loading angle. As the loading angle is increased, the loaded flattened area gets larger, leading to a more uniform stress distribution around the crack and the sample itself.
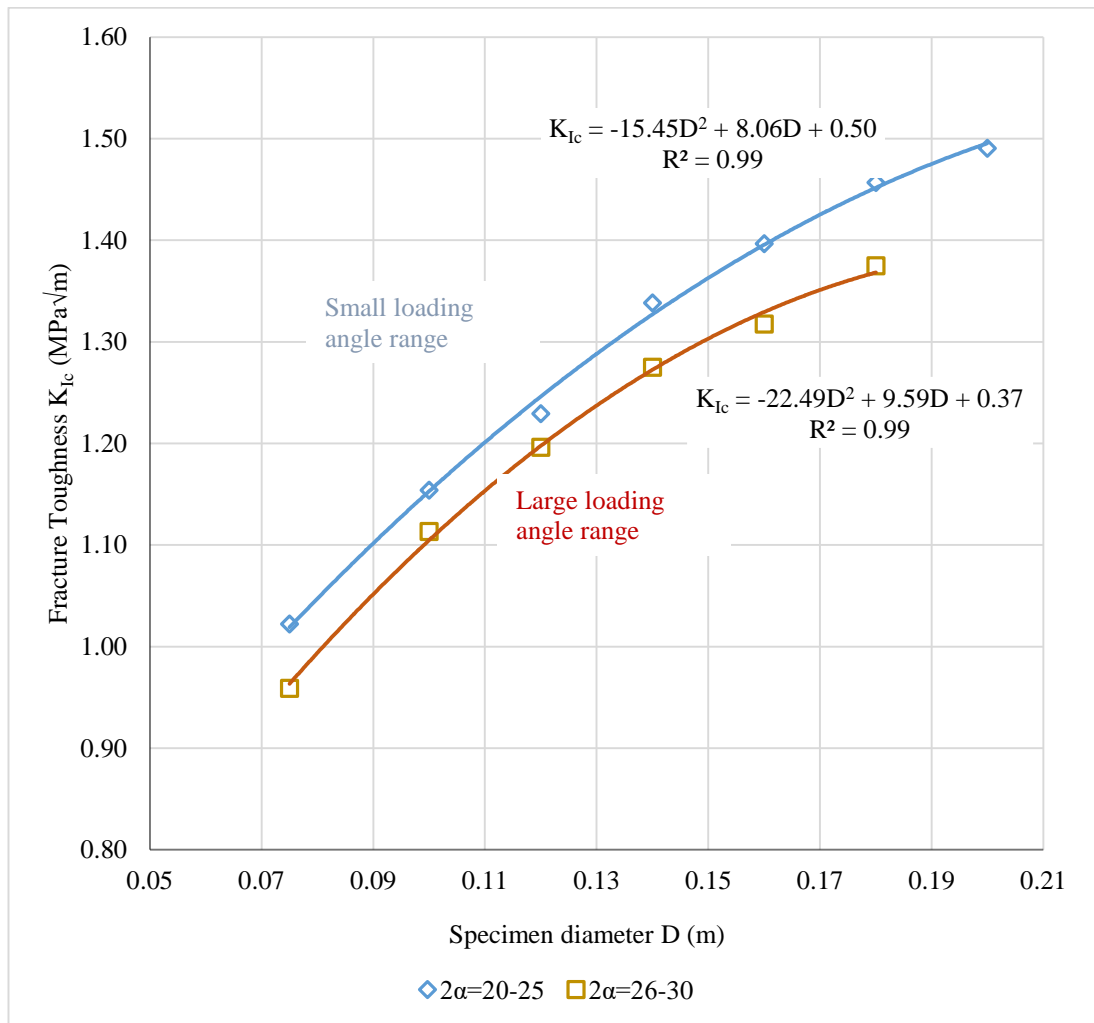
Figure 6.13 Average K$_{Ic}$ values vs specimen diameter at small (20-25°) and large (26-30°) loading angle ranges

According to Figure 6.13, trend will be continued like second degree parabolic equation. When the derivative of this equation was taken and equals to zero, the peak point values ca be found; which is *D* is equal to 0.26 m for small angle range and D= 0.21 m for the large loading angle range. At this diameter values the size independent fracture toughness values can be found as 1.56 MPa$\sqrt{m}$ for the small angle ranges whereas for these ranges the fracture toughness values found from the tests result is 1.50 MPa$\sqrt{m}$. Likewise when the diameter equals to 0.21 m for large loading angle range, the fracture toughness values can be found as 1.39 MPa$\sqrt{m}$ whereas *K$_{Ic}$* value found from the test result is 1.37 MPa$\sqrt{m}$. Therefore, small angle range were selected

for further analysis and the fracture toughness vs specimen diameter graph drawn only for small angle ranges can be seen in Figure 6.14.

The figure shows a plot with y-axis "Fracture Toughness K_{Ic} (MPa√m)" ranging from 0.80 to 1.60, and x-axis "Specimen diameter D (m)" ranging from 0 to 0.5. An equation is shown:

$$K_{Ic} = -15.45D^2 + 8.06D + 0.50$$
$$R^2 = 0.99$$
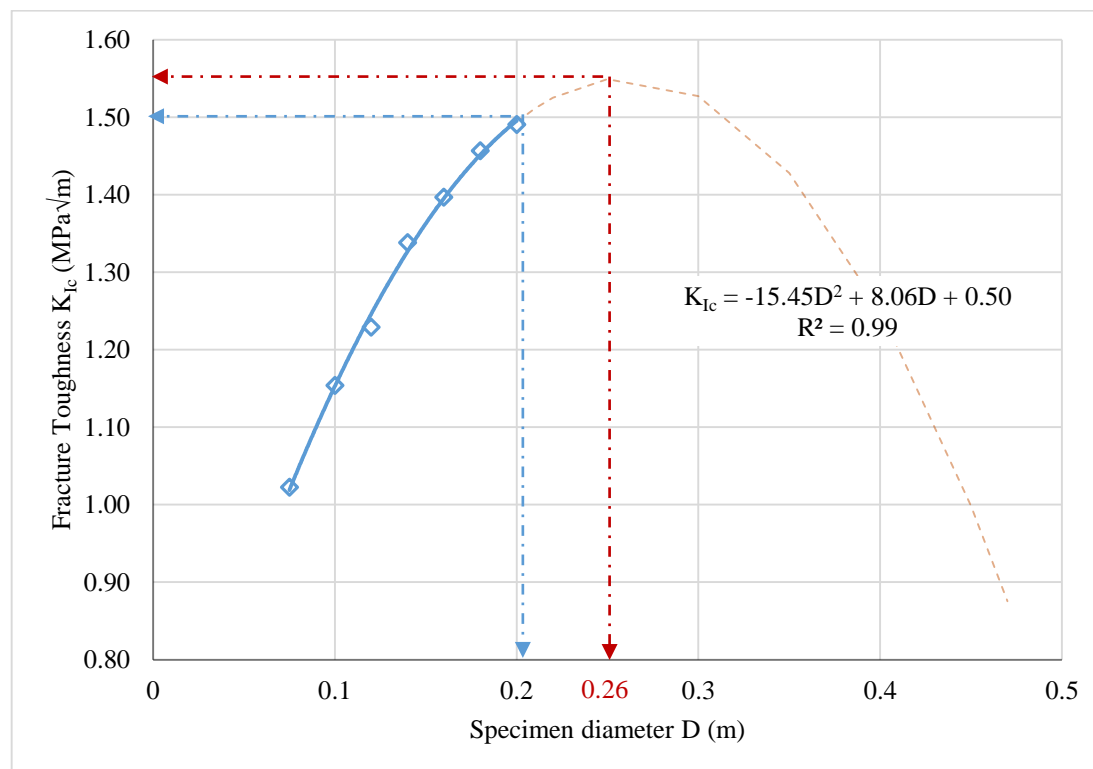
Figure 6.14 Average K_{Ic} values vs specimen diameter at small (20-25º) loading angle range

For small angle range case, when the trend line were sketched for larger diameter, the variation of the graph look like in Figure 6.14. And the difference between found and computed maximum fracture toughness values can be seen more clearly.

This comparison can be interpreted as the angle range (20-25º) is considered to represent K_{Ic} better since the free and loaded boundaries are sufficiently far from the crack tip. Therefore, the same angle range results are used both in size effect investigations and boundary influence investigations.

In order to investigate the size effect in terms of loading angles, average K_{Ic} values vs $L/R = \sin\alpha$ values graphs are plotted in Figure 6.15.
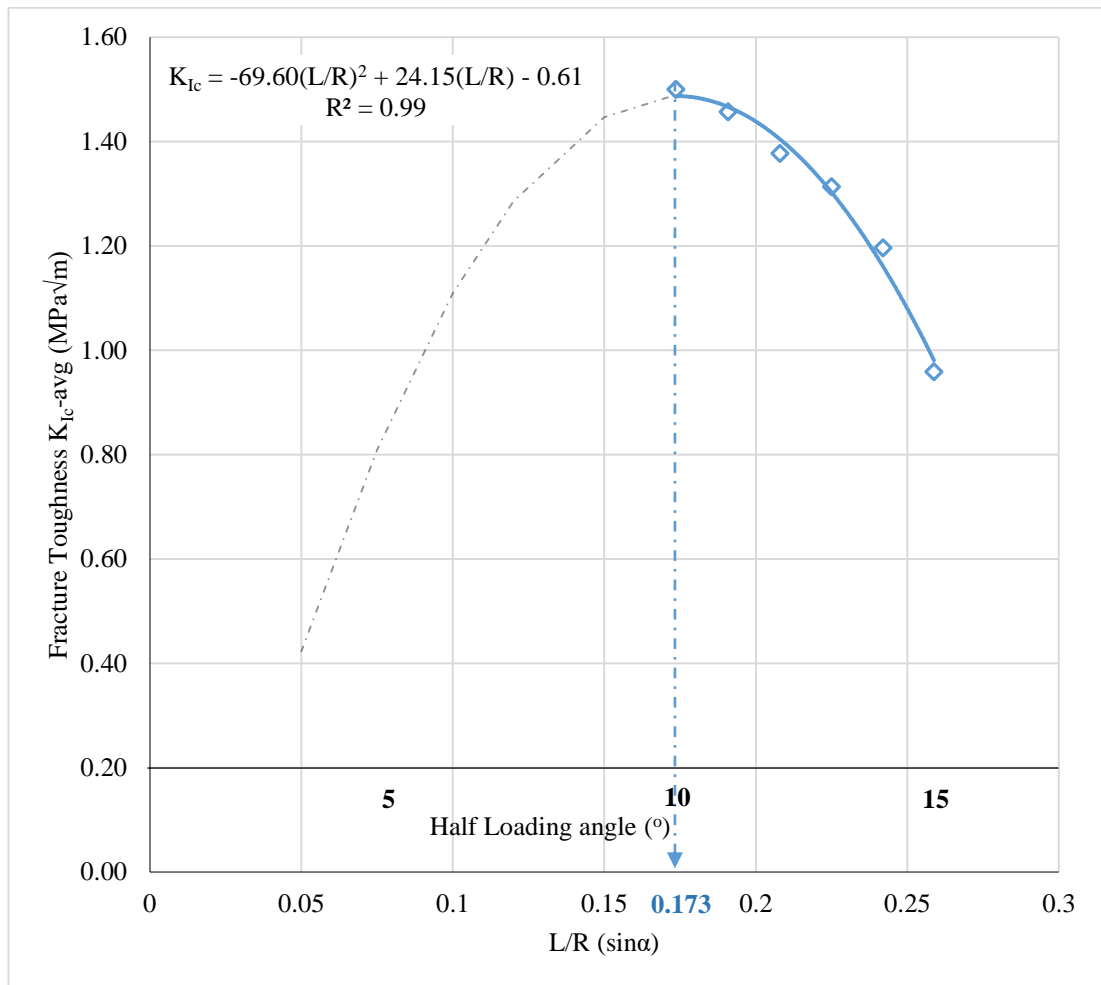
Figure 6.15 Average K_{Ic} *values vs L/R*

According to Figure 6.15, K_{Ic} and *L/R* (which is equal to sinα) graph, it is seen that a quadratic polynomial fit gives the highest R-square value. When the derivative of this equation was taken and equals to zero, the peak point values can be found; which is L/R is equal to 0.173, which means α is 9.96^o and 2α is 19.92^o. At this loading angle the size independent fracture toughness can be found and it and it can be concluded that this loading angle value is near the proposed angle values.

6.2.6. Investigation of Bazant's size effect

The Bazant's size effect law can be expressed by the following formula;

$$\sigma_N = \frac{Bf_t}{\sqrt{1-\beta}} \quad , \quad \beta = \frac{D}{D_o} \qquad\qquad (6.1)$$

where:

σ_N= nominal strength at failure (MPa)

B= empirical constant related with the dimension

f_t= tensile strength of concrete (MPa) for a standard size of laboratory scale

β= brittleness number

D= characteristic dimension of the specimen (m);

D_o= empirical coefficient showing the transition between brittle and nonbrittle behavior (m)

To estimate the nominal strength, σ_N, of a large size structural unit or section, first laboratory tests are done to find f_t. In the limits of Equation 6.1, as β approaches 1, σ_N goes to infinity and material is highly brittle. As β gets to zero, size effect disappears and f_t and σ_N become equal. β becomes 1 when $D=D_o$. On the other hand, β becomes zero as D gets zero so that, no size effect estimation is necessary since the characteristic dimension does not exist anymore.

The D_o parameter gives the deviation from the cut-off point of the asymptotic slope (corresponding to the LEFM) and the geometrical horizontal asymptote (corresponding to the strength criterion) in the size effect curve, (Figure 6.16). D_o and the resulting brittleness number (β) are closely related to the sample shape, size and loading condition. In geometrically similar samples, B and D_o are constant (RILEM, 1991). The size effect related equations (Bazant and Kazemi, 1991) proposed by Bazant can be arranged with regression analysis (Bazant and Planas, 1998). With the help of this regression analysis, the unknown empirical constants B and D_o can be

found. These formulas only apply to concretes with the same mix design and the same maximum aggregate grain size.
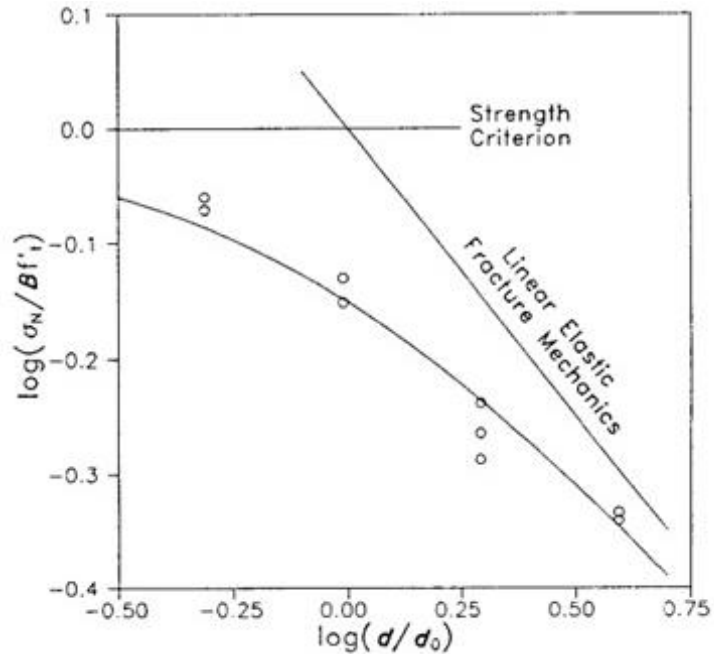
Figure 6.16 Test data and size effect graphs taken from Bazant and Pfeiffer (RILEM, 1991)

In the log (σ_N) vs. log (D) graph (size effect graph shown in Figure 6.16), lab scale strength for any failure criteria can be expressed with the horizontal line.

In LEFM stress solutions, replacing σ_{yy} (Table 2.1) with the strength, it is seen that σ_N is inversely proportional to $D^{1/2}$. The representation of LEFM on the log (σ_N) vs log (D) graph is a line with a slope of -1/2 (Bazant and Pfeifer, 1987) as seen in Figure 6.16. For LEFM-based fracture toughness tests, data points approaching that LEFM line shows the quality of tests to obtain size-independent fracture toughness.

With the equations and statistical approaches, size effect phenomena will be applied to the analysis of FBD test results. In order to investigate the size effect, it is necessary to carry out various experiments on samples having geometrically similar but different characteristic dimensions. In this study, the size effect, which was investigated in the previous studies for beam type samples with different notch dimensions, was analyzed for molded shotcrete FBD samples.

Based on the size effect studies conducted by Bazant, size effect plots were created according to the linear regression analysis. In Bazant's size effect analysis, sample diameters were taken as the characteristic dimension of the sample (*D*). Since the *ft* value indicates the tensile strength of the concrete sample, the average value obtained by indirect tensile strength (Brazilian) test was taken as 4.0 MPa (Table 4.4). The size effect related equations (Bazant and Kazemi, 1991) proposed by Bazant can be arranged with regression analysis (Bazant and Planas, 1998). With the help of this regression analysis, the unknown empirical constants *B* and D_o can be found. By using the two linear regression formulas (Linear Formula I and Linear Formula II) given in Equations 6.2-6.5, the size effect graphs can be drawn.

Y=AX+C (Linear Formula I)   Y'=A'X'+C' (Linear Formula II)
Where:

$$X = D \qquad\qquad X' = \frac{1}{D} \qquad\qquad (6.2)$$

$$Y = \left(\frac{1}{\sigma_N}\right)^2 \qquad\qquad Y' = \left(\frac{1}{\sigma_N D}\right)^2 \qquad\qquad (6.3)$$

$$C = \left(\frac{1}{B f_t}\right)^2 \qquad\qquad C' = \frac{A'}{D_O} \qquad\qquad (6.4)$$

$$A = \frac{C}{D_0} \qquad\qquad A' = \left(\frac{1}{B f_t}\right)^2 \qquad\qquad (6.5)$$

For FBD geometries, every time the loading angle is changed, a new specimen geometry emerges. So, for this particular geometry, Bazant size effect constant *B* and coefficient D_o should be calculated. Calculation process involves a regression analysis (Bazant and Planas, 1998). As discussed before, more reliable K_{Ic} results, which suffers minimum from the size and boundary influence issues, are found for a geometry with large diameters and a loading angle around 22°. That's why, Bazant size effect analysis is conducted only for a data set with loading angle of 22° and varying diameters.

Slopes are *A* in Linear Formula I and *A'* in Linear Formula II, whereas intercept point is *C* and *C'* for Linear Formula I and Linear Formula II, respectively. First intercept points are found by using linear regression analysis. From the intercept points, constant *B* of a particular FBD geometry with a particular loading angle (e.g. 22º) is calculated. Slope *A* is found from regression analysis again. Then, using the slope *A* and the intercept point *C* computed above, coefficient D_o is calculated.

For σ_N values, tensile strength of each FBD samples were calculated based on the formula proposed by Keleş and Tutluoğlu (2011).

$$\sigma_N = \left[\frac{2P}{\pi Dt}\right] x[0.83\ cos\alpha + 0.15] \qquad (6.6)$$

The average σ_N values were calculated for five valid test data and given for 16 different molds in Table 6.4.

Table 6.4 Averages of calculated σ_N values of each sample

Sample Code	σ_N (MPa)
C75-24	3.45
C75-30	3.94
C100-22	3.06
C100-28	3.62
C120-22	2.90
C120-28	3.27
C140-22	2.93
C140-26	3.28
C140-28	3.34
C160-22	2.86
C160-24	2.99
C160-28	3.30
C180-22	2.78
C180-28	3.21
C200-20	2.52
C200-22	2.67

Linear regression analysis was performed with Minitab 17 Statistical Software program (Minitab 17 Support, 2019) to find the constants B and C in the equation of size effect law. Linear regression I analysis was conducted with $X \& Y$ data set values, whereas linear regression II analysis were conducted with $X' \& Y'$ values. Data set involved the varying diameter D in X-horizontal axis and $\sigma_N/(Bf_t)$ as in vertical Y-axis for the particular loading angle of 22°. The summary table of size effect parameters for a data set with loading angle of 22° and varying diameters is given in Table 6.5 below.

Table 6.5 Size effect parameters for samples with 22° loading angle and varying diameter

Parameter	Linear Regression I	Linear Regression II
A	0.0004	0.0014
C	0.065	- 3.93 x 10-6
D_o (m)	0.170	- 0.365
Bft (MPa)	3.93	26.38
B	0.98	6.60
R-square	74.5	96.3

The R-square value of linear regression II was higher, but D_o value calculated from the second equation (Linear regression II) was negative. Therefore, linear regression I was chosen, although it had a comparatively lower R-square value. Based on the size effect studies conducted by Bazant, size effect plots were created according to the linear regression analysis. The results of the experiments were arranged as size effect plots and the size effect parameters were obtained. The size effect plot, which is *log (σ_N/Bft)* vs. *log (β)* graph, created from the FBD test results of samples with 22° loading angle and varying diameter was prepared. Constant B and the coefficient D_o calculated from linear regression I analysis can be seen in Figure 6.17 where β means D/D_o.
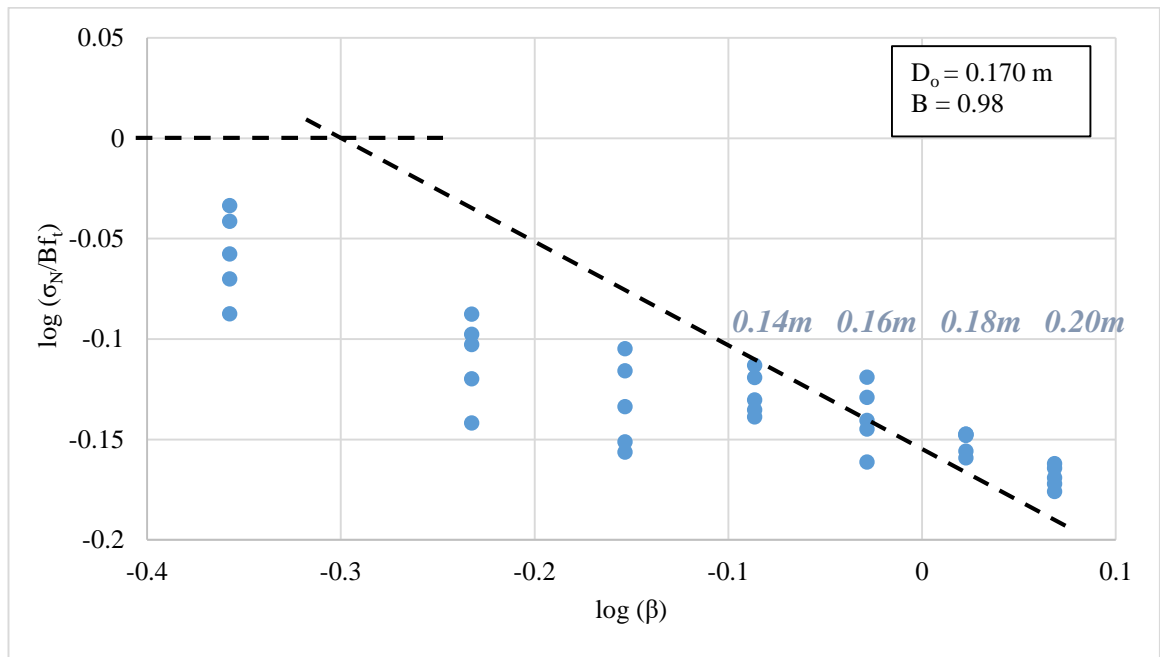
Figure 6.17 Size effect plot of samples having loading angle of 22º

According to Figure 6.17, the geometry of samples with 160 mm diameter is found as the most appropriate geometry as it falls perfectly on the LEFM line.

The dashed horizontal line indicates the strength criterion. In the strength criterion, the strength of the sample remains constant despite the varying size. The dashed line with a slope of -1/2 indicates LEFM. LEFM has a strong size effect. In fact, the nominal strength of concrete is between these two ideal situations. As the element sizes increase and the brittleness increases, LEFM is approached (Bazant and Pfeiffer, 1987).

According to the linear regression analysis conducted D_o value and B value were found as 0.170 m (170 mm) and 0.98, respectively. As seen in Figure 6.17, the test results of samples with 160 mm and higher diameter seem to approach to the LEFM line.

Linear Elastic Fracture Mechanic (LEFM) line of Bazant's proposed size effect plot is first intersected first by 160 mm diameter sample results. 180 mm and 200 mm test results stayed well on and around the LEFM line range.

Since the geometry and failure mode were the same in all samples, the size effect equations were easily implemented. The data obtained from the experimental results are consistent with the results of Bazant's size effect. The most appropriate geometries for measuring the nominal tensile strength without suffering from the size effect for FBD shotcrete samples have diameters 160 mm and larger.

6.3. Comparison of BDT and FBD Test Results

BDT tests were conducted on core samples without jaws. K_{Ic} values were calculated with Equation 5.2 similar to the FBD samples. The shotcrete core samples were around 30 mm in thickness and around 53-54 mm in diameter.

According to the Equation 5.3, the calculated critical crack length a_{cn} is the same as the sample diameter. The situation of complete splitting along the diametric path is also observed during the BDT testing without jaws.

The details of the analysis are given in Table 6.6. To compute K_{Ic} for samples of zero loading angle ($2\alpha=0$), Y_{Imax} was computed as 5.418

Table 6.6 P$_{min}$ and K$_{Ic}$ values of shotcrete BDT samples

ID	P_{min} (kN)	K_{Ic} (MPa $\sqrt{m}$)
C-BR-s1	9.97	10.66
C-BR-s2	13.36	12.74
C-BR-s3	11.81	11.15
C-BR-s4	11.34	12.49
Avg. ± Std. Dev.	*11.62±1.40*	*11.76±1.01*

It was observed that the initial crack length was equal to the sample diameter. In other words, when the experiment was carried out, the first crack opening was directly dividing the sample into two parts. Even with very slow loading speed, the initial crack opening occurred suddenly and the sample was divided into two parts instantly. In addition, in the load-vertical displacement graphs of samples with BDT sample, no local minimum load and second load rise was observed.

The aim of this BDT and FBD comparison analysis is to check the applicability of regular BDT test without curved platens to estimate K_{Ic} at zero loading angle. The average K_{Ic} value obtained at 0° loading angle was found as 11.76 MPa $\sqrt{m}$, although the maximum K_{Ic} value obtained at varying loading angles from 30° to 20° was 1.50 MPa $\sqrt{m}$. This showed that loading angle range of 2-50 is a bit too extreme. In fact, suggested loading angle range was reported to be around 23º (Keleş and Tutluoğlu, 2011). Practical applicability of FBD test is to be limited with loading angles between 20-30 due to the theoretical background restrictions. Using jaws is causing an artificially induced loading angle; if Y_{Imax} for zero angle is used this may not be the right approach and K_{Ic} results are computed as too high.

CHAPTER 7

CONCLUSIONS AND RECOMMENDATIONS

Fracture mechanics has not yet fully achieved the importance it deserves related to shotcrete in various engineering fields. Studies related to cracks in shotcrete should become widespread and these studies should keep pace with new contemporary technology. One of the innovative technologies, 3D printer technology is combined with the subject of fracture mechanics in this thesis. In the fracture mechanics experiments performed in the laboratory, the sample preparation part, which is the most challenging stage of the experiments, was easily handled with the help of 3D printer technology.

As a short summary of this study, before starting experiments, the materials to be used in the shotcrete mixture were selected and decided whether they were suitable or not. The shotcrete mixing procedure was established and the shotcrete mix design was validated with the help of *UCS* and *BDT*. After the validation tests were completed, the samples were prepared based on the determined shotcrete mix design. Due to the problems encountered during the sample preparation stage, sample molds having different dimensions were produced with a 3D printer and samples were prepared with these molds. 80 valid *FBD* tests were carried out on samples that were extracted from 16 molds with diameter varying between 75-200 mm and loading angles between 20°-30°. These test results were assessed for measures such as loading angle, diameter change, and size effect.

Using one of the latest technologies, 3D printer technology, the fracture properties of the shotcrete and the size effect were investigated and consistent results were obtained in this study. With the help of the mold the geometries of the samples are nearly perfect so the number of the valid tests are considerably higher than other studies. Another feature that distinguishes this study from other studies is that *FBD* tests are preferred

instead of 3-point bending method for the fracture mechanics experiments. 3D printing technology has been proven that it can be easily applied in the experiments related with mechanic issues due its practical and time-saving nature. Summary of the study, conclusion and the possible future studies are presented in this chapter.

7.1. Conclusions

The conclusions of this study can be summarized as;

- Sample preparation with regular coring, grinding and polishing caused damage and irregularities in the specimen sections. 3D printing technology was the solution. The importance of sample preparation is crucial for the FBD tests. One of the criteria required for the qualification of the tests to be valid/successful is that the crack should start from the center of the sample and proceed on that line. Number of invalid tests were low, since 3D printed molds had smooth parallel ends and boundaries.

- As the diameter of the sample increased from 75 mm to 200 mm, the success rate of the experiments increased and the number of invalid tests decreased significantly.

- The most obvious assessment is that Mode I fracture toughness increases 56.3% (from 0.96 MPa$\sqrt{m}$ to 1.50 MPa$\sqrt{m}$) as the specimen diameter increases from 75 mm to 200 mm. Crack find an easy path to propagate into the binder on small size samples. On the other hand, for large samples both grain aggregate and binding material are intersected evenly.

- The difference between computed (a_{cn}) and measured (a_{ce}) critical crack lengths is decreasing, while the diameter of sample is increasing because the load can be more uniformly distributed on the larger flattened area. Similarly, the absolute difference between a_{cn}/R and a_{ce}/R values decreases around 87.5% (from 0.099 to 0.012), while specimen diameter increases from 75 mm to 200 mm.

- The size effect ratio defined as $K_{Ic,max}/K_{Ic,min}$ increases with decreasing loading angle. As the loading angle is increased, the loaded flattened area gets larger,

leading to a more uniform stress distribution around the crack and the sample itself. However, the loading angle range of 20-25° is concluded to represent K_{Ic} measurements better since the free and loaded boundaries are sufficiently far from the crack tip for small loading angles.

- Smaller loading angle range (20-25°) samples give more accurate K_{Ic} measurement than larger angle range (26-30°) results.

- K_{Ic} values were lower for higher loading angles (higher sinα=L/R) for the sample with the same diameter.

- The deviation in individual K_{Ic} results decreases for larger diameter samples. In fact, the smallest deviation is observed for tests on samples having the largest diameter (200 mm).

- Based on the size effect studies conducted by Bazant, a size effect plot was created with the linear regression analysis. In size effect analysis, varying FBD sample diameters were taken as the characteristic dimension of the sample. For testing on shotcrete with 22° loading angle FBD geometry, the size effect coefficients resulting from the size effect equations is identified as $D_o = 0.170$ m (170 mm) and $B = 0.98$.

- For Bazant's size effect analysis, the most appropriate geometries for measuring the nominal tensile strength without suffering from the size effect for FBD shotcrete samples have diameters 160 mm and larger.

- In this study, shotcrete samples with FBD geometries having the largest diameter used in fracture toughness tests have been analyzed.

- Summing up, the size- and boundary influence-independent fracture toughness of shotcrete is measured as 1.50 MPa$\sqrt{m}$ for FBD samples of 200 mm diameter and 20° loading angle.

- As a conclusion, the optimum specimen geometry for Mode I fracture toughness of shotcrete with FBD method starts with 160 mm diameter; preferable it should be around 200 mm diameter having 20-25° loading angle.

This conclusion is reached based on the size effect, boundary influence and initial crack length investigations.

7.2. Future Study and Recommendations

In order to evaluate the entire fracture behavior of shotcrete, different tests can be conducted by changing the water / cement ratio, adjusting the maximum aggregate size according to the sample size, using different types of cements, using the same mix design but different testing method such as 3-point bending method or modified ring testing method. As for the different mix design case, fiber can be used as an ingredient of the mixture. However, carbon fiber should be used, because in the first stages of the thesis study, steel fibers were used in the mix design and could not be distributed evenly and homogeneously in the mixture due to the rather heavy weight of steel fibers. Due to the density of fiber, they segregated and accumulated at the bottom of the mold. So, carbon fibers are lighter and carbon fiber can be tried as an alternative ingredient.

Another possible future study can be digitizing the cracks on the close shot photos taken during experiment and investigate the variation of distance of cracks from the center/middle line.

As a recommendation, in the future studies the molds can be prepared with a rather durable material, because at some stages of this study the molds were broken during the removal process. New molds had to be rebuilt. As the mold removal process is very labor intensive, a better solution can be taken into consideration when making new molds.

REFERENCES

(2019, September). Retrieved from Poligon Mühendislik: https://www.poligonmuhendislik.com

(2019, January). Retrieved from Minitab 17 Support: https://support.minitab.com/en-us/minitab/17/

Akkaya, Y., Bayramov, F., & Taşdemir, M. (2003). Betonun Kırılma Mekaniği: Tasarımda Kullanılan Mekanik Özellikler ile Kırılma Parametreleri Arasındaki Bağıntılar. *Türkiye Mühendislik Haberleri Vol. 426*.

Aliha, M., Sistaninia, M., Smith, D., Pavier, M., & Ayatollahi, M. (2012). Geometry Effects and Statistical Analysis of Mode I Fracture In Guiting. *International Journal of Rock Mechanics and Mineral Sciences, 51*, 128-135.

Alkılıçgil, Ç. (2010). *Development of Specimen Geometries For Mode I Fracture Toughness Testing with Disc Type Rock Specimen.* Ankara: Ph.D. Thesis, METU.

Anderson, T. L. (2005). *Fracture Mechanics: Fundamentals and Applications.* CRC Press.

Arrea, M., & Ingraffea, A. (1982). *Mixed Mode Crack Propagation in Mortar and Concrete, rEPORT nO. 81-13.* Cornell University.

ASTM. (2008). ASTM D3967-08 Standard test method for splitting tensile strength of intact rock core specimens.

Austrian Concrete Society. (n.d.). Code of Practice for Sprayed Concrete.

Backers, T. (2005). *Fracture toughness determination and micromechanics of rock under mode I and Mode II loading.* Postdam: University of Potsdam.

Barrenblatt, G. I. (1962). The Mathematical Theory of Equilibrium Cracks In Brittle Materials. *Advances In Applied Mechanics, Vol. 7*, 55-129.

Bazant, Z. (1983). Fracture in Concrete and Reinforced Concrete. *Mechanics of Geomaterials, Rocks Concretes, Soils, Preprints, IUTAM Prager Symposium* (pp. 281-317). Northwestern University.

Bazant, Z. (1984). Size effect in blunt fracture:concrete, rock, metal. *Journal of Engineering Mechanics, 110*, 518-535.

Bazant, Z. P., & Oh, B. H. (1983). Crack band theory for fracture of concrete. *Materials and structures, 16*, 155-177.

Bazant, Z., & Kazemi, M. (1990). Determination of fracture energy, process zone length, and brittleness number from size effect with application to rock and concrete. *International Journal of Fracture Vol 44(2)*, 111-131.

Bazant, Z., & Kazemi, M. (1990a). Size effect of fracture in ceramics and its use to determine fracture energy and effective process zone length. *Journal of american ceramic society, 77*, 1841-1853.

Bazant, Z., & Kazemi, M. (1990b). Size effect on diagonal shear failure of beams without stirrups. *ACI Structural Journal, 88* , 268-276.

Bazant, Z., & Oh, B. (1983). Crack band theory for fracture concrete. *Materials & Structures (RILEM) Vol 16 (93)*, 155-157.

Bazant, Z., & Pfeiffer, P. (1986). Shear Fracture Tests of Concrete . *Materials and Structures, 19*, 111-121.

Bazant, Z., & Pfeiffer, P. (1987). Determination of Fracture Energy from Size Effect and Brittleness Number. *ACI Materials Journal*, 463-480.

Bazant, Z., & Planas, J. (1998). *Fracture and size effect in concrete and other quasibrittle materials.* Boca Raton: CRC Press.

Bazant, Z., Daniel, I., & Li, Z. (1995). *Size effect and fracture characteristics of fiber-composite laminates.* Evanson: Civil Engineering Northwestern University.

Chong, K., & Kuruppu, M. (1984). New specimen for fracture toughness determination of rock and other materials. *International Journal of Fracture*, 59-62.

Cotterell, B. (2002). The past, present, and future of fracture mechanics. *Engineering Fracture Mechanics 69*, 533-553.

da Vinci, L. (1894). Codex Atlanticus 1504 Milano. In M. Pinati, *Bibilioteca Ambrosiana.*

Docherty, J. G. (1932). Bending tests on geometrically similar notched bar specimens. *Engineering*, 133-645.

Drover, C., & Villaescusa, E. (2015). Performance of Shotcrete Surface Support Following dynamic loading of mining excavations. *Shotcrete for Underground Support XII* . ECI Symposium Series.

Eligehausen, R., & Ozbolt, J. (n.d.). *Size Effect in Concrete Structures.* 2018.

(n.d.). *EN 206:2013+A1 Concrete - Specification, performance, production and conformity standard.*

(n.d.). *EN 933-9 Tests for geometrical properties of aggregates - Part 9: Assessment of fines - Methylene blue test.*

Erarslan, N., & Williams, D. (2012). Experimental, numerical and analytical studies on tensile strength of rocks. *International Journal of Rock Mechnaic a& Mineral Sciences, 49*, 21-30.

Erarslan, N., Liang, Z., & Williams, D. (2012). Experimental and numerical studies on determination of indirect tensile strength of rocks. *International Journal of Rock Mechanics and Mining Sciences, 45*, 739-751.

Erdoğan, T. (2003). *Beton.* Ankara: ODTÜ Yayıncılık.

Galilei, G. (1638). *Dialogues concerning two new sciences.* Evanston: University of Illinois Press.

Galilei, G. (1936). *Dialogues concerning two new sciences.* Evanston: University of Illinois Press.

Gao, X., Liu, C., Tan, Y., Yang, N., Qiao, Y., Hu, Y., & Chazallon, C. (2019). Determination of fracture properties of concrete using size and boundary effect models. *Applied Sciences (Switerland), 9*, 1-20.

Ghasemi, Y. (2017). *Aggregates in Concrete Mix Design.* Luleå: Luleå University of Technology.

Griffith, A. A. (1920). The phenomenon of rupture and flow in solids. *Philosophical Transactions of the Royal Society of London A221*, 163-198.

Griffith, A. A. (1924). The theory of rupture. *Proceedings of the first International Congress for Applied Mechanics* (pp. 55-63). Delft: Technische Boekhandel en Drukkerij.

Guo, H., Aziz, N., & Schmidt, L. (1993). Rock Fracture-Toughness Determination by the Brazilian Test. *Engineering Geology*, 177-188.

Gutiérrez-Moizant, R., Ramírez-Berasategui, M., Santos-Cuadros, S., & García-Fernández, C. (2018). Computational Verification of the Optimum Boundary Condition of the Brazilian Tensile Test. *Rock Mechanics and Rock Engineering*, 3505-3519.

(2017). *Hazır Beton Komitesi Yıllık Faliyet Raporu.* Ankara: Türkiye Çimento Müstahsilleri Birliği .

Heere, R., & Morgan, D. R. (2002, Spring). Determination of Early-Age Compressive Strength of Shotcrete. *Shotcrete*, pp. 28-31.

Hillerborg, A., Modéer, M., & & Petersson, P. E. (1976). Analysis of crack formation and crack growth in concrete by means of fracture mechanics and finite elements. *Cement and concrete research, 6*, 773-781.

Hondros, G. (1959). The evaluation of Poisson's ratio and modulus of materials of a low tensile resistance by the Brazilian (indirect tensile) test with particular reference to concrete. *Journal of Applied Sciences*, 243-268.

Irwin, G. (1958). Fracture. In *Handbuch der Physik* (pp. 551-590). Berlin: Springer.

ISRM. (1979). Suggested Methods for Determining the Uniaxial Compressive Strength. *Int. J. Rock Mech. Min. Sci. & Geomech*, 135-140.

ISRM. (1988). Suggested methods for determining the fracture toughness of rock. *International Journal of Rock Mechanics and Mining Sciences & Geomechanics Abstracts, 25*, 71-96.

ISRM. (2007). Suggested Method for Determining Tensile Strength of Rock Materials. In R. Ulusay, & J. Hudson, *The Complete ISRM Suggested Methods for Rock Characterization, Testing and Monitoring: 1974-2006* (pp. 181-183). Ankara: Kozan Ofset.

Jenq, Y., & Shah, S. (1985). A two-parameter model for concrete. *Journal of Enginnering Mechnaics-ASCE Vol.111*, 1227-1241.

Kanninen, M., & Popelar, C. (1985). *Advanced Fracture Mechancis.* Oxford University Press.

Kaplan, M. (1961). Crack propagation and the fracture of concrete. *Journal of ACI Vol.58*, 591-610.

Kazemi, M., Fazileh, F., & Ebrahiminezhad, M. (2007). Cohesive crack model and fracture energy of steel-fiber-reinforced concrete notched cylindrical specimens. *Journal of Materials in Civil Engineering, 19*, 884-890.

Keleş, Ç., & Tutluoğlu, L. (2011). Investigation of proper specimen geometry for mode I fracture toughness testing with flattened Brazilian disc method. *International Journal of Fracture, 169*, 61-75.

Kesler, C., Naus, D., & Lott, J. (1971). Fracture mechanics its applicability to concrete. *The Society of Material Science Vol.4*, 113-124.

Kirkaldy, D. (1864). *Results of an experimental inquiry into the tensile strength and other prperties of various kinds of wrought-iron and steel.* Glasgow: Private publication.

Komurlu, E., & Kesimal, A. (2015). Evaluation of indirect tensile strength of rocks using different types of jaws. *Rock Mechanics and Rock Engineering*, 1723-1730.

Komurlu, E., Kesimal, A., & Demir, S. (2016). Experimental and numerical analyses on determination of indirect (splitting) tensile strength of cemented paste backfill materials under different loading apparatus. *The Geomechanics and Engineering, 10*, 775-791.

Kosmatka, S. H., Kerkhoff, B., & Panarese, W. C. (2003). *Design and Control of Concrete Mixtures.* Skokie, Illinois, USA: Portland Cement Association.

Kourkoulis, S. K., Markides, C. F., & Chatzistergos, P. (2013). The standardized Brazilian disc test as a contact problem. *International Journal of Rock Mechanics & Mining Sciences, 57*, 132-141.

Kuleli, Ö. (2010). *Çimento Mühendisliği El Kitabı.* Ankara: TÇMB/AR-GE.

Kumar, S., & Barai, S. (2012). Size effect of fracture parameters for rack propagation in concrete: a comparative study. *Computers and Concrete, 9*, 1-19.

Lackner, R., & Mang, H. (2001). Cracking in shotcrete tunnel shells. *Fracture Mechanics of Concrete Structures* (pp. 857-870). Lisse: Swets & Zeitlinger.

Lemay, J.-D., Jolin, M., & Gagne, R. (2014). Ultra rapid strength development in dry-mix shotcrete for ultra rapid support in challenging mining conditions. In M. Hudyma, & Y. Potvin, *Proceedings of the Seventh ınternational Conference on Deep and High Stress Mining* (pp. 271-279). Perth: Australian Centre for Geomechanics.

Long, N., & Marian, R. (2008). Investigation of fracture properties of steel fiber reinforced cocnrete. *3rd ACF International Conference, ACF/VCA*, (pp. 854-861).

Lu, A., Wang, S., & Cai, H. (2018). Closed-Form Solution for the Stresses in Brazilian Disc Tests Under Vertical Uniform Loads. *Rock Mechanics and Rock Engineering* , 3489–3503 .

Mindess, S., Young, J. F., & Darwin, D. (2003). *Concrete.* NJ: Prentice Hall, Pearson Education, Inc.

Nallathambi, P., & Karihaloo, B. (1986). Determination of the specimen size independent fracture toughness of plain concrete. *Magazine of Concrete Research Vol. 38*, 67-76.

Ouchterlony, F. (2007). Suggested methods for determining the fracture toughness of rock. In R. Ulusay, & J. Hudson, *The complete ISRM suggested methods for rock characterization, testing and monitoring: 1974-2006* (pp. 231-258). Ankara, Turkey: ISRM Turkish National Group.

Özdoğan, C. (2017). Pure tensile fracture modelling and toughness measurements on brazilian discs of andesite and marble. Unpublished thesis, Ankara.

Parton, V. Z. (1992). *Fracture Mechanics: From Theory to Practice.* CRC Press.

Perez, N. (2004). *Fracture mechanics.* Boston: Springer.

Pillai, S. U., Erki, M. A., & Kirk, D. W. (1999). *Reinforced Concrete Design.* McGraw-Hill Ryerson.

RILEM. (1991). Size-effect method for determining fracture energy and process zone size of concrete. *Materials and Structures, 23*, 461-465.

RILEM. (2004). Quasibrittle fracture scaling and size effect - Final report. *Materials and Structures, 37*, 547-568 .

Satoh, Y. (1986). Position and load of failure in Brazilian test; a numerical analysis by Griffith criterion. *Journal of the Society of Materials Science Japan*, 1219-1224.

SIKA. (2001). *SIKA ViscoCrete Hi-Tech* .

SpaceClaim Support. (2018, November). Retrieved from Ansys SpaceClaim Web Site: http://www.spaceclaim.com/en/Support/

Sun, C., & Jin, Z. (2012). *Fracture Mechanics.* United States: Academic Press, Elsevier.

Tang, T., Ouyang, C., & Shah, S. (1996). A simple method for determining material fracture parameters from peak loads. *ACI Materials Journal*, 147-157.

Tang, T., Yang, S., & Zollinger, D. (1999). Determination of fracture energy and process zone length using variable-notch one-size specimens. *ACI Material Journal, 96*, 3-10.

Tokyay, M. (2016). *Cement and Concrete Mineral Admixtures.* CRC Press.

Ulusay, R., & Hudson, J. A. (2007). *The Complete ISRM Suggested Methods for Rock Characterization, Testing and Monitoring: 1974-2006.* Ankara.

US Army Corps of Engineers. (1993). *EM 1110-2-2005 Standard Practice for Shotcrete.* Washington, DC.

Vinci, L. d. (1894). Codex Atlanticus 1504 Milano. In M. Pinati, *Bibilioteca Ambrosiana.*

Wang, Q. Z., & Xing, L. (1999). Determination of fracture toughness KIc by ussing the flattened Brazilian dics specimen for rocks. *Engineering Fracture Mechanics (64)*, 193-201.

Wang, Q., Jia, X., & Kou, S. Z.-A. (2004). The flattened Brazilian disc specimen used for testing elastic modulus, tensile strength and fracture toughness of brittle

rocks: analytical and numerical results. *International Journal of Rock Mechanics & Mining Sciences, 41*, 245-253.

Westergaard, H. (1934). Stresses at a crack, size of the crack and the bending of reinforced concrete. *Prov. American Concrete Institute, Vol. 30*, 93-102.

Widijanto, E., Setiawan, E., Ramirez, M., & Napitupulu, D. (2010). Shotcrete application and optimization at PT Freeport Indonesia's Deep Ore Zone Mine . In S. Bernard, *Shotcrete: Elements of a System* (pp. 283-289). London: Taylor & Francis Group.

Williams, M. (1957). On The Stress Distribution at The base of A Stationary Crack. *Journal of Applied Mechanics*, 109-114.

Yalçın, H., & Gürü, M. (2006). *Çimento ve Beton.* Ankara: Palme Yayıncılık.

Yayla, P. (2007). *Kırılma Mekaniği.* İstanbul: Çağlayan Kitabevi.

Yu, Y., Zhang, J., & Zhang, J. (2009). A modified Brazilian disc tension test. *Internation Journal of Rock Mechanics & Mineral Sciences*, 421-425.

APPENDICES

A. PARTICLE SIZE DISTRIBUTION OF CEMENT – CEM I 42.5 R

d(0.1): 1.207 um   d(0.5): 12.662 um   d(0.9): 37.869 um

Particle Size Distribution

— 8181578

Size (µm)	Vol Over %	Size (µm)	Vol Over %	Size (µm)	Vol Over %	Size (µm)	Vol Over %	Size (µm)	Vol Over %	Size (µm)	Vol Over %
0.020	100.00	0.800	92.95	15.000	44.70	40.000	8.33	75.000	0.00	300.000	0.00
0.125	100.00	0.900	92.09	16.000	42.53	45.000	5.21	90.000	0.00	350.000	0.00
0.200	99.99	1.000	91.34	20.000	34.39	50.000	3.02	100.000	0.00	400.000	0.00
0.300	99.24	2.000	85.76	25.000	25.55	55.000	1.54	120.000	0.00	500.000	0.00
0.400	97.94	4.000	76.16	27.000	22.45	60.000	0.62	125.000	0.00	600.000	0.00
0.500	96.47	5.000	72.09	30.000	18.30	63.000	0.30	150.000	0.00	900.000	0.00
0.600	95.11	8.000	62.07	32.000	15.84	64.000	0.22	200.000	0.00	1000.000	0.00
0.700	93.94	10.000	56.56	35.000	12.62	65.000	0.16	250.000	0.00	1500.000	0.00

Figure A.1. Particle size distribution graph of Cement – CEM I 42.5 R

B. 3D DRAWINGS OF SHOTCRETE MOLDS

C7524

C7530

C10022

C10028

Figure B.2. 3D Drawings of shotcrete molds of C7524, C7530, C10022, C10028
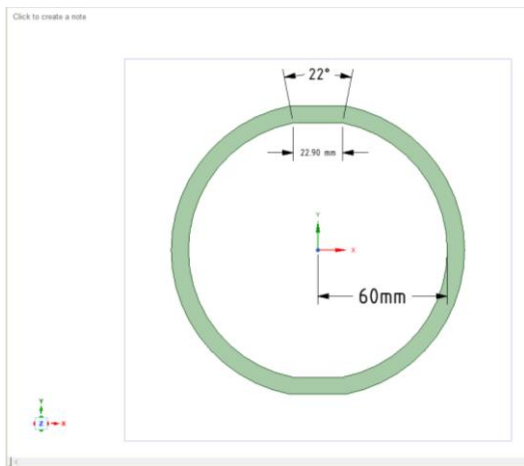
C12022
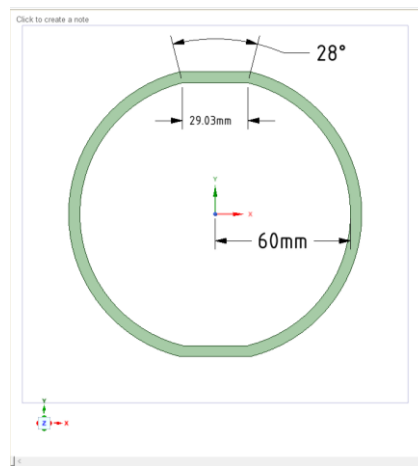
C12028
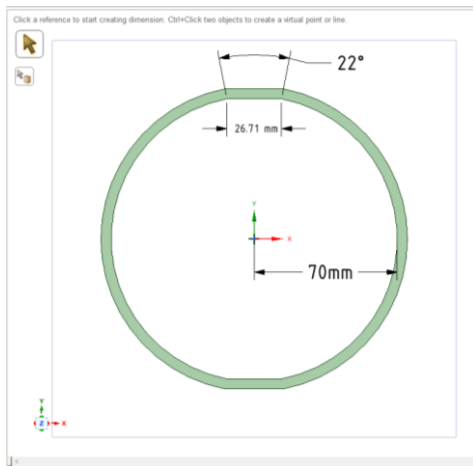
C14022
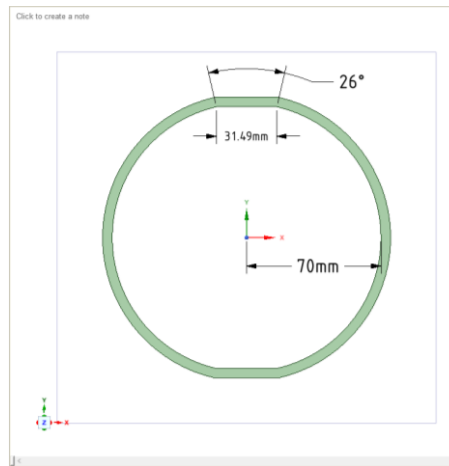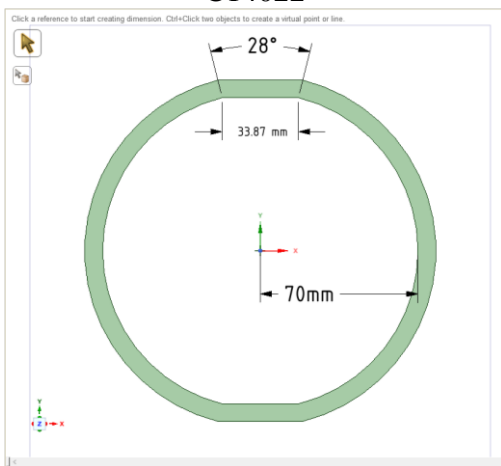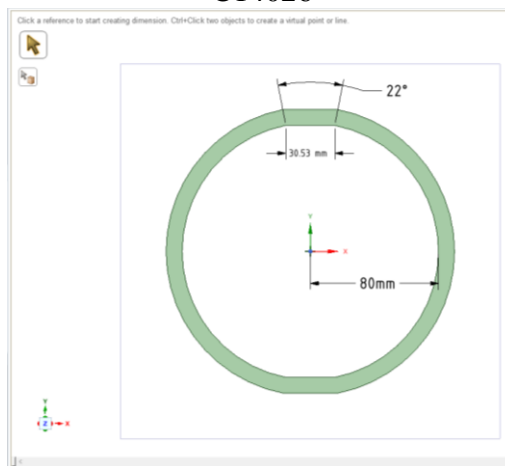
C14026

C14028

C16022

Figure B.3. 3D Drawings of shotcrete molds of C12022, C12028, C14022, C14026, C14028, C16022
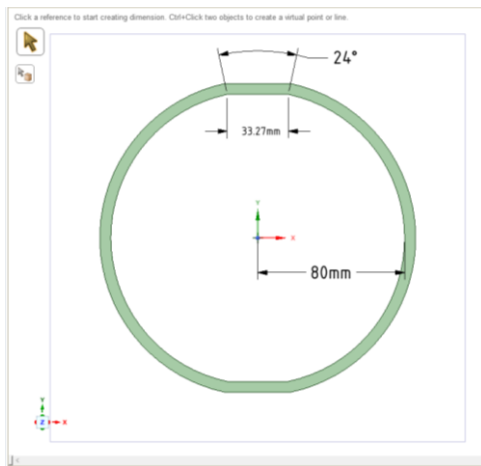
C16024
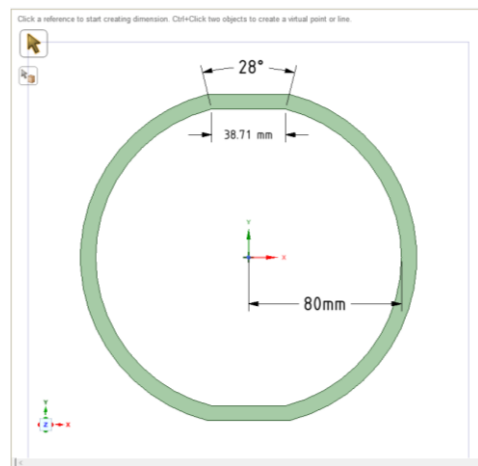
C16028
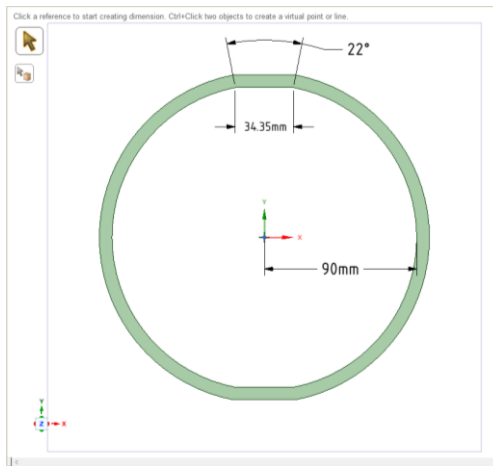
C18022
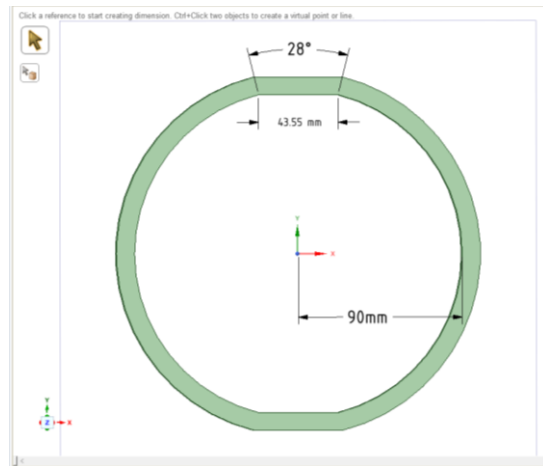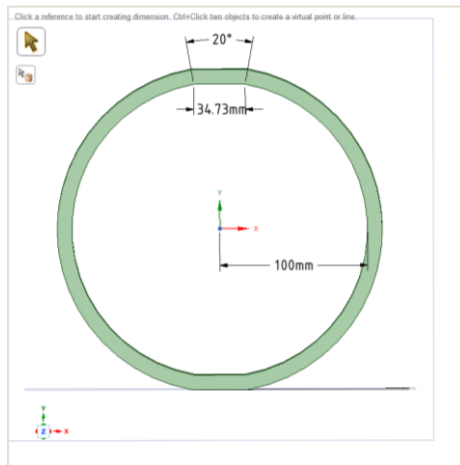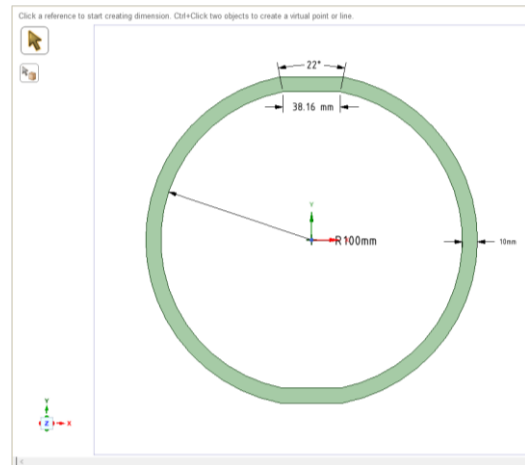
C18028

C20020

C20022

Figure B.4. 3D Drawings of shotcrete molds of C16024, C16028, C18022, C18028 C20020, C2002

C. DEFORMABILITY TEST PHOTOS

Figure C.5. Example of the deformability test photos during the test

(a)

(b)

Figure C.6. Example of the deformability test photos (a) before and (b) after the test

(a)

(b)

(c)

Figure C.7. Example photos of the Brazilian test (a) before, (b) during and (c) after the test

D. DETAILS OF FBD TESTS

(a) before test   (b) during test   (c) after test
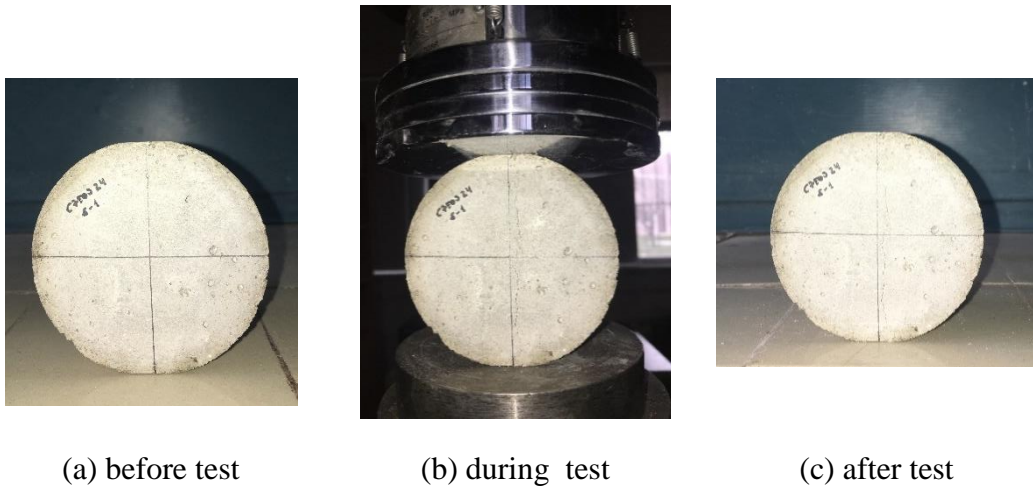
Figure D.8. C75-24 coded - FBD sample before, during, and after the test

Table D.1. Pmin and KIc values of C75-24 coded shotcrete FBD samples

ID	P_{min} (kN)	K_{Ic} (MPa $\sqrt{m}$)
C75-24_s1	19.4	1.10
C75-24_s2	17.1	0.95
C75-24_s3	18.3	1.04
C75-24_s4	17.6	0.98
C75-24_s5	17.9	1.04
Avg. ± Std. Dev.	*18.1±0.9*	*1.02±0.06*
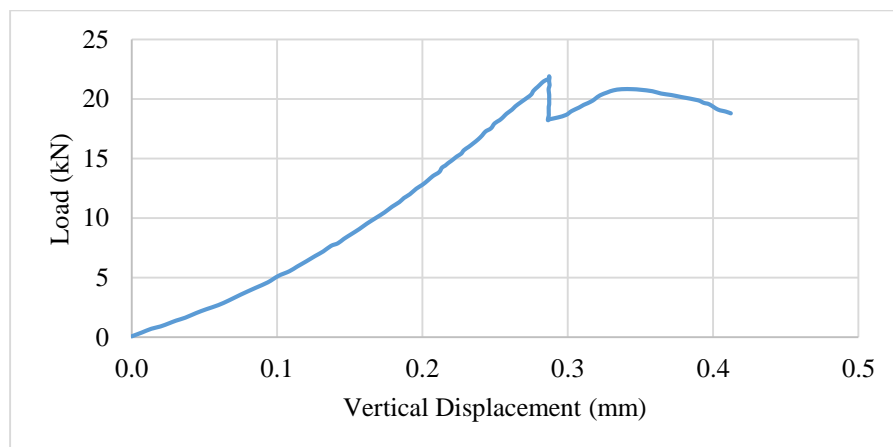
Figure D.9. Load-vertical displacement graph of C75-24_s3

Table D.2. Comparison of measured and calculated crack length of C75-24 coded-FBD samples

ID	a_{ce} (mm)	a_{ce}/R	$|a_{ce}-a_{cn}|$ (mm)	$|a_{ce}/R-a_{cn}/R|$
C75-24_s1	23.11	0.616	3.15	0.084
C75-24_s2	22.61	0.603	3.65	0.097
C75-24_s3	23.56	0.628	2.70	0.072
C75-24_s4	22.39	0.597	3.87	0.103
C75-24_s5	21.95	0.585	4.31	0.115
Avg. ± Std. Dev.	*22.72±0.63*	*0.606±0.017*	*3.54±0.63*	*0.094±0.017*

(a) before test   (b) during test   (c) after test

Figure D.10. C75-30 coded - FBD sample before, during and after the test

Table D.3. P_{min} and K_{Ic} values of C75-30 coded shotcrete FBD samples

ID	P_{min} (kN)	K_{Ic} (MPa $\sqrt{m}$)
C75-30_s1	21.9	1.01
C75-30_s2	19.3	0.87
C75-30_s3	20.1	0.92
C75-30_s4	22.1	1.00
C75-30_s5	21.2	0.99
Avg. ± Std. Dev.	*20.9±1.2*	*0.96±0.06*
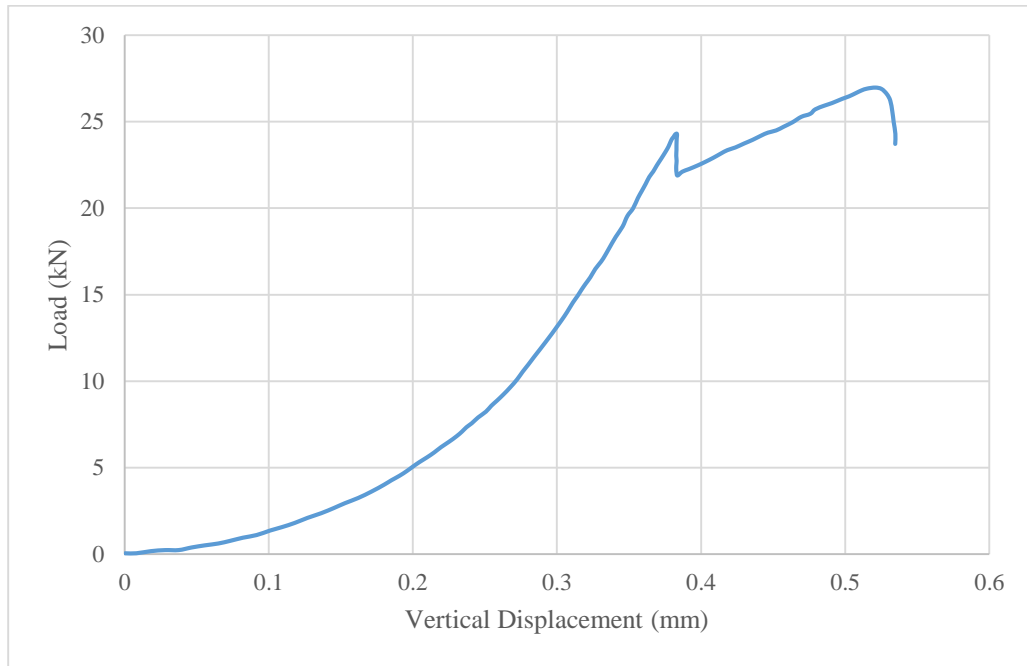
Figure D.11. Load-vertical displacement graph of C75-30_s4

Table D.4. Comparison of measured and calculated crack length of C75-30 coded- FBD sample

ID	a_{ce} (mm)	a_{ce}/R	$|a_{ce}-a_{cn}|$ (mm)	$|a_{ce}/R-a_{cn}/R|$
C75-30_s1	21.03	0.561	3.01	0.080
C75-30_s2	20.03	0.534	4.01	0.107
C75-30_s3	20.80	0.555	3.24	0.086
C75-30_s4	20.68	0.551	3.36	0.090
C75-30_s5	19.02	0.507	5.02	0.134
Avg. ± Std. Dev.	*20.31±0.81*	*0.542±0.022*	*3.73±0.81*	*0.099±0.022*

| (a) before test | (b) during test | (c) after test |
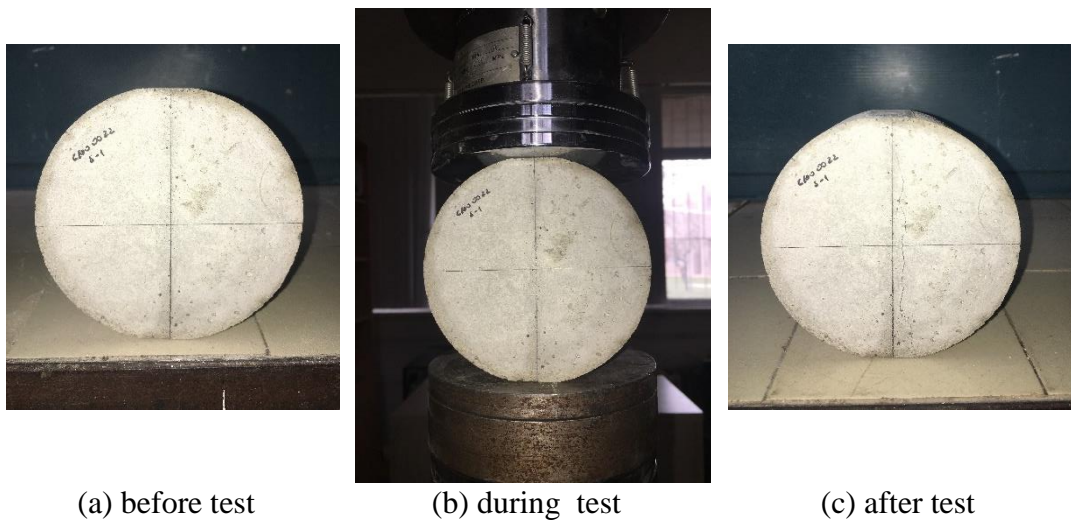
Figure D.12. C100-22 coded - FBD sample before, during and after the test

Table D.5. P_{min} and K_{Ic} values of C100-22 coded shotcrete FBD samples

ID	P_{min} (kN)	K_{Ic} (MPa $\sqrt{m}$)
C100-22_s1	30.1	1.21
C100-22_s2	29.6	1.19
C100-22_s3	27.1	1.09
C100-22_s4	27.8	1.12
C100-22_s5	28.6	1.15
Avg. ± Std. Dev.	*28.6±1.2*	*1.15±0.05*
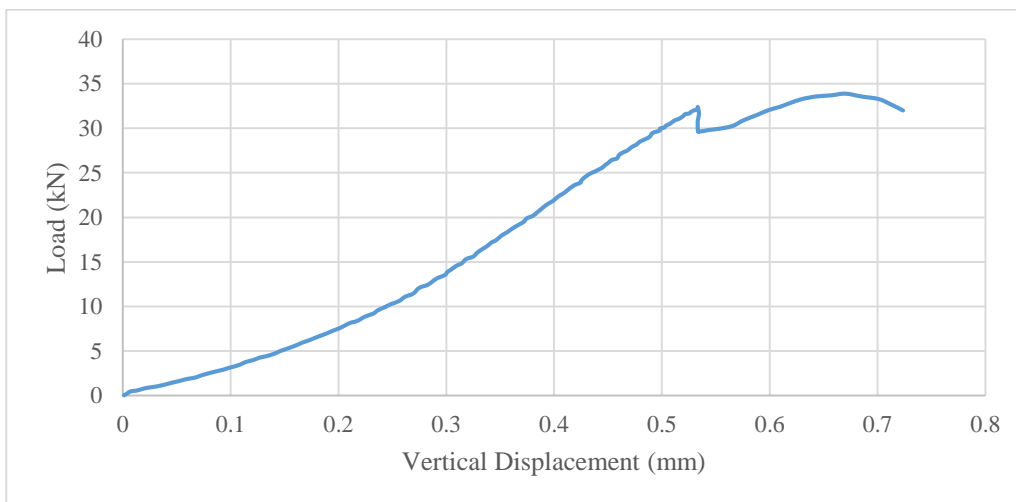
Figure D.13. Load-vertical displacement graph of C100-22_s2

Table D.6. Comparison of measured and calculated crack length of C100-22 coded- FBD sample

ID	a_{ce} (mm)	a_{ce}/R	$\|a_{ce}-a_{cn}\|$ (mm)	$\|a_{ce}/R-a_{cn}/R\|$
C100-22_s1	39.51	0.790	3.44	0.069
C100-22_s2	40.20	0.804	4.13	0.083
C100-22_s3	38.29	0.766	2.22	0.044
C100-22_s4	38.03	0.761	1.96	0.039
C100-22_s5	39.40	0.788	3.33	0.067
Avg. ± Std. Dev.	*39.09±0.90*	*0.782±0.018*	*3.02±0.90*	*0.060±0.018*

(a) before test	(b) during test	(c) after test
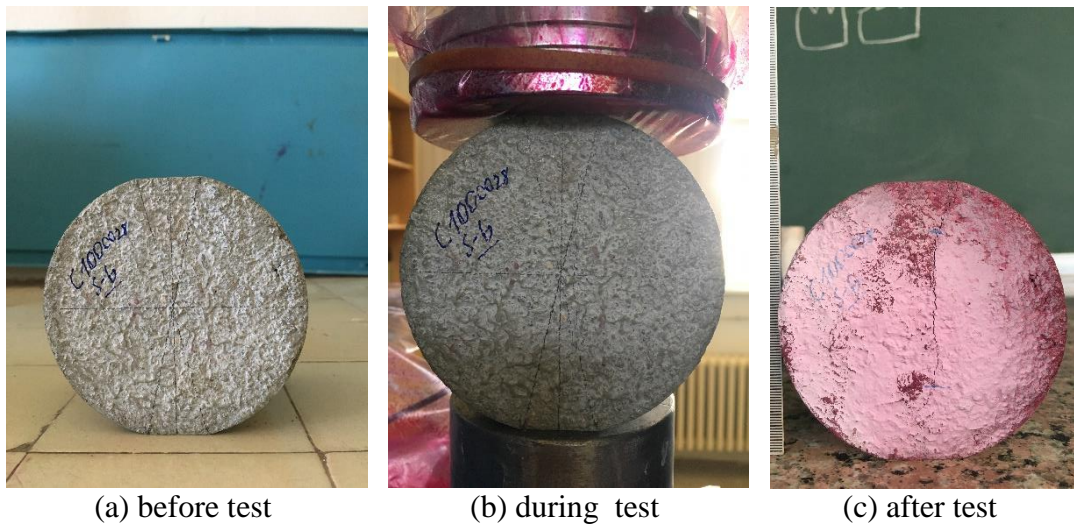
Figure D.14. C100-28 coded - FBD sample before, during and after the test

Table D.7. P_{min} and K_{Ic} values of C100-28 coded shotcrete FBD samples

ID	P_{min} (kN)	K_{Ic} (MPa $\sqrt{m}$)
C100-28_s1	32.2	1.05
C100-28_s2	33.6	1.09
C100-28_s3	36.9	1.20
C100-28_s4	34.1	1.11
C100-28_s5	34.5	1.12
Avg. ± Std. Dev.	*34.3±1.7*	*1.11±0.06*
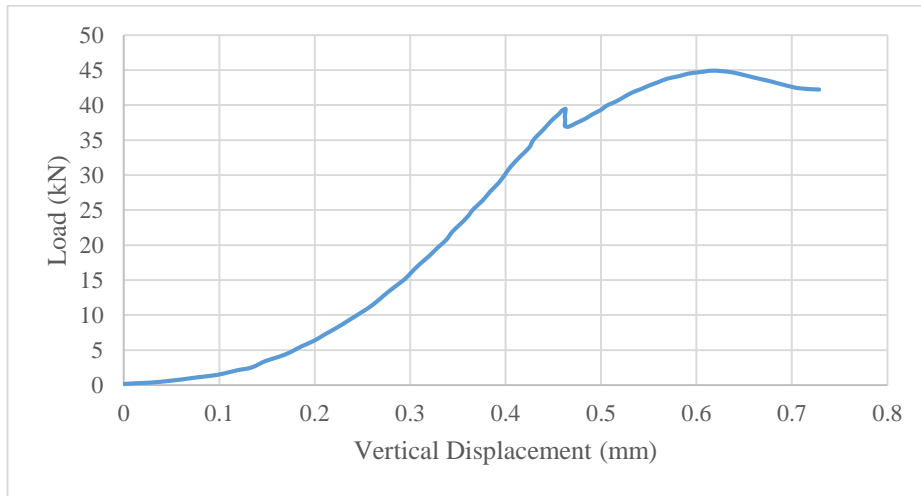
Figure D.15. Load-vertical displacement graph of C100-28_s3

Table D.8. Comparison of measured and calculated crack length of C100-28 coded- FBD sample

ID	a_{ce} (mm)	a_{ce}/R	$\|a_{ce}-a_{cn}\|$	$\|a_{ce}/R-a_{cn}/R\|$
C100-28_s1	30.31	0.606	2.71	0.054
C100-28_s2	28.94	0.579	4.08	0.082
C100-28_s3	29.77	0.595	3.25	0.065
C100-28_s4	29.17	0.583	3.85	0.077
C100-28_s5	31.09	0.622	1.93	0.039
Avg. ± Std. Dev.	*29.86±0.87*	*0.597±0.017*	*3.16±0.87*	*0.063±0.017*

(a) before test   (b) during test   (c) after test
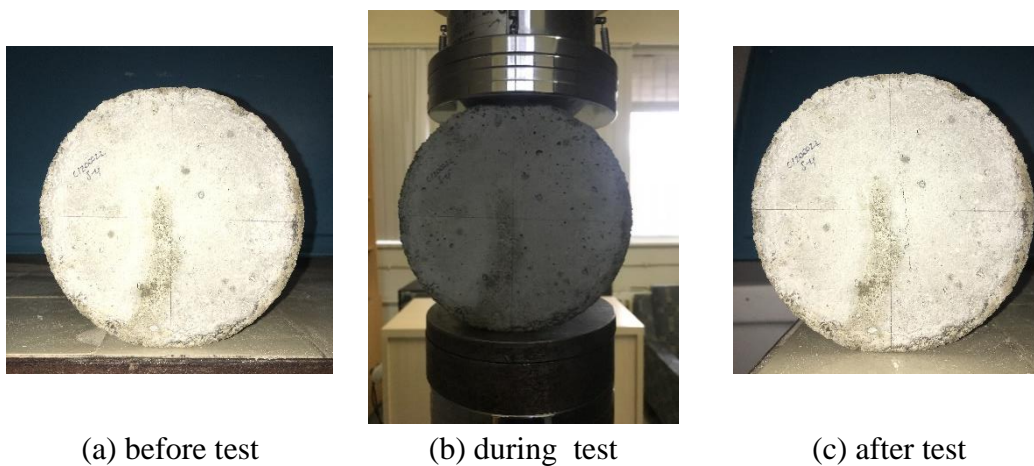
Figure D.16. C120-22 coded - FBD sample before, during and after the test

Table D.9. P_{min} and K_{Ic} values of C120-22 coded shotcrete FBD samples

ID	P_{min} (kN)	K_{Ic} (MPa $\sqrt{m}$)
C120-22_s1	39.2	1.18
C120-22_s2	41.2	1.25
C120-22_s3	38.6	1.17
C120-22_s4	42.1	1.27
C120-22_s5	41.4	1.28
Avg. ± Std. Dev.	*40.5±1.5*	*1.23±0.05*
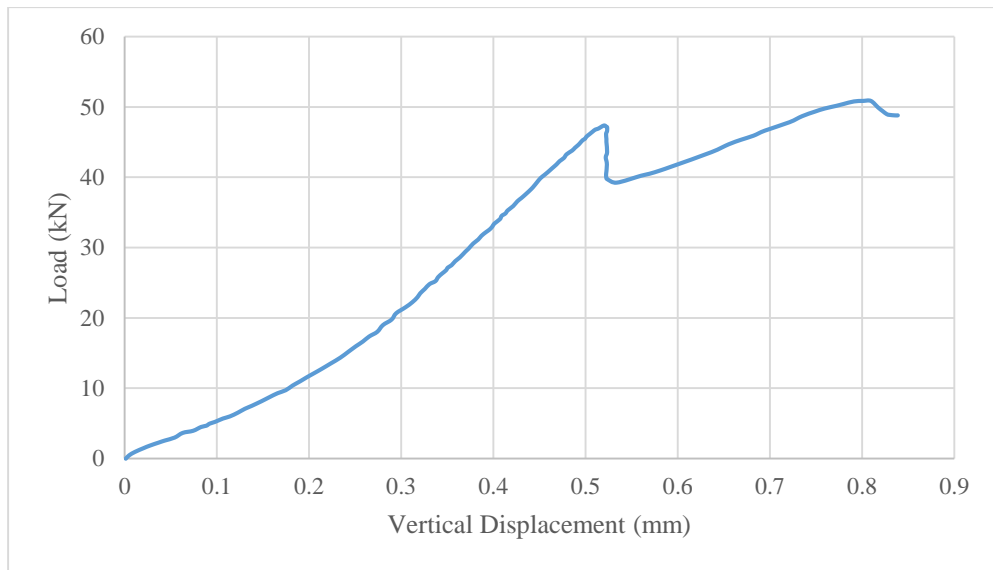
Figure D.17. Load-vertical displacement graph of C120-22_s1

Table D.10. Comparison of measured and calculated crack length of C120-22 coded- FBD sample

ID	a_{ce} (mm)	a_{ce}/R	$\|a_{ce}\text{-}a_{cn}\|$ (mm)	$\|a_{ce}/R\text{-}a_{cn}/R\|$
C120-22_s1	47.42	0.790	4.14	0.069
C120-22_s2	43.25	0.721	0.03	0.000
C120-22_s3	45.02	0.750	1.74	0.029
C120-22_s4	47.09	0.785	3.81	0.064
C120-22_s5	46.27	0.771	2.99	0.050
Avg. ± Std. Dev.	*45.81±1.70*	*0.764±0.028*	*2.54±1.68*	*0.042±0.028*

| (a) before test | (b) during test | (c) after test |
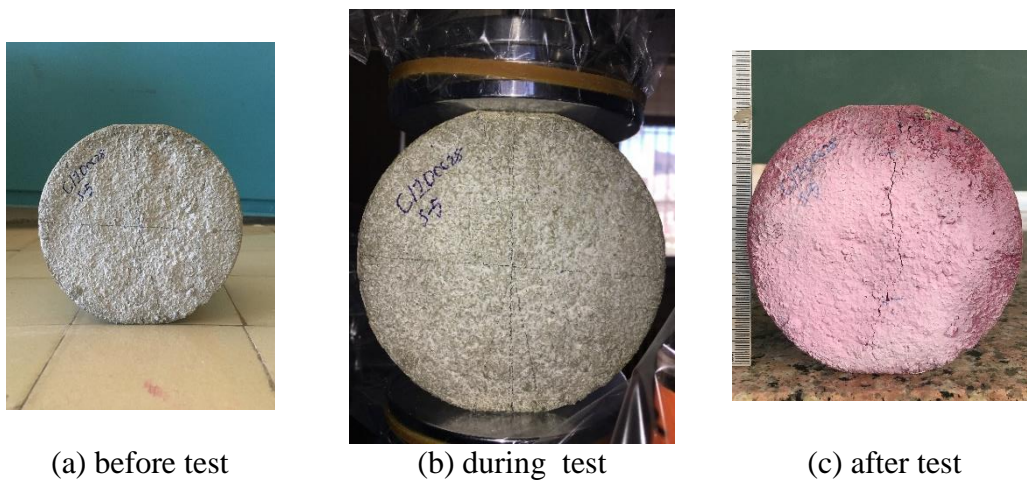
Figure D.18. C120-28 coded - FBD sample before, during and after the test

Table D.11. P_{min} and K_{Ic} values of C120-28 coded shotcrete FBD samples

ID	P_{min} (kN)	K_{Ic} (MPa $\sqrt{m}$)
C120-28_s1	48.8	1.24
C120-28_s2	44.7	1.18
C120-28_s3	45.2	1.20
C120-28_s4	47.2	1.20
C120-28_s5	43.5	1.15
Avg. ± Std. Dev.	*45.9±2.1*	*1.20±0.03*
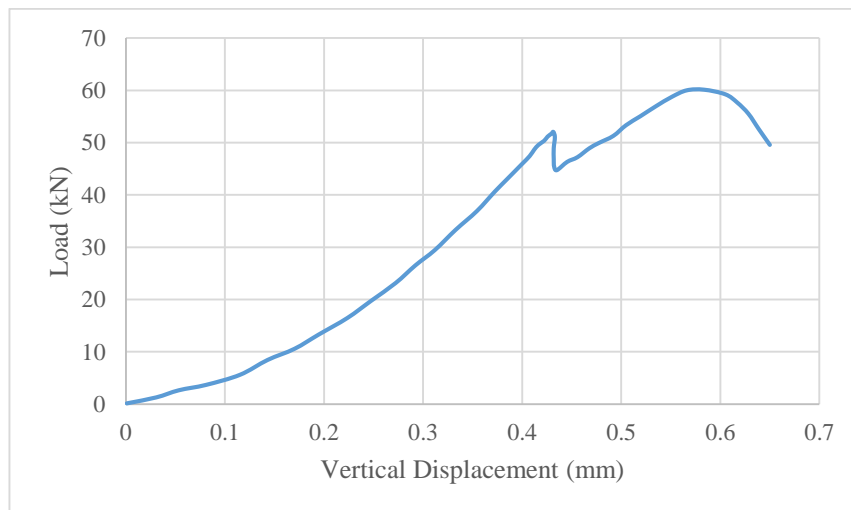
Figure D.19. Load-vertical displacement graph of C12028-s2

Table D.12. Comparison of measured and calculated crack length of 120-28 coded- FBD sample

ID	a_{ce} (mm)	a_{ce}/R	$|a_{ce}-a_{cn}|$ (mm)	$|a_{ce}/R-a_{cn}/R|$
C120-28_s1	36.47	0.608	3.15	0.052
C120-28_s2	37.66	0.628	1.96	0.033
C120-28_s3	36.14	0.602	3.48	0.058
C120-28_s4	38.11	0.635	1.51	0.025
C120-28_s5	40.89	0.682	1.27	0.021
Avg. ± Std. Dev.	*37.85±1.88*	*0.631±0.031*	*2.27±0.99*	*0.038±0.016*

(a) before test   (b) during test   (c) after test
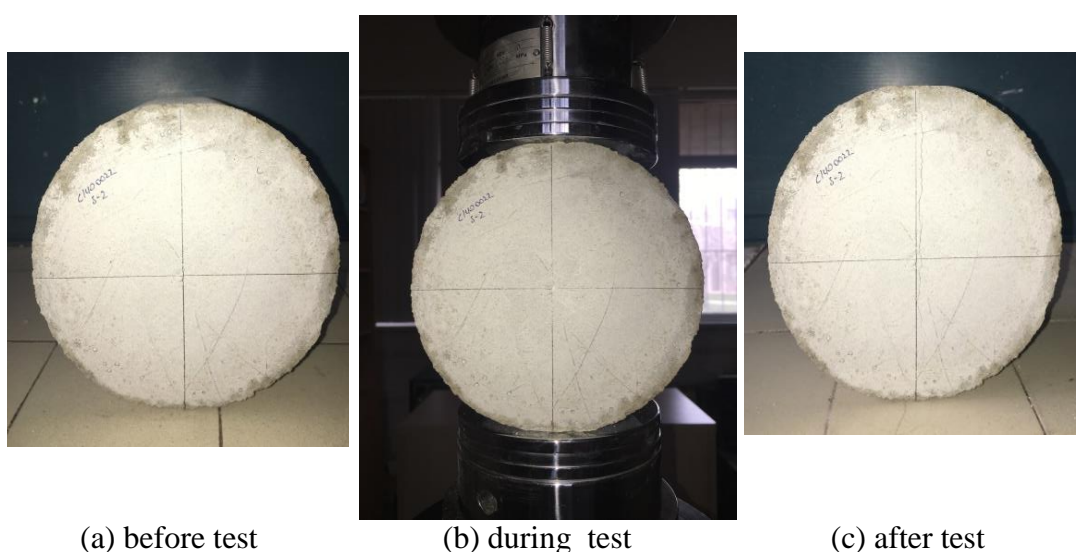
Figure D.20. C140-22 coded - FBD sample before, during and after the test

Table D.13 P_{min} and K_{Ic} values of C140-22 coded shotcrete FBD samples

ID	P_{min} (kN)	K_{Ic} (MPa $\sqrt{m}$)
C140-22_s1	54.2	1.30
C140-22_s2	57.4	1.38
C140-22_s3	53.3	1.27
C140-22_s4	55.0	1.33
C140-22_s5	58.1	1.41
Avg. ± Std. Dev.	*55.6±2.1*	*1.34±0.06*
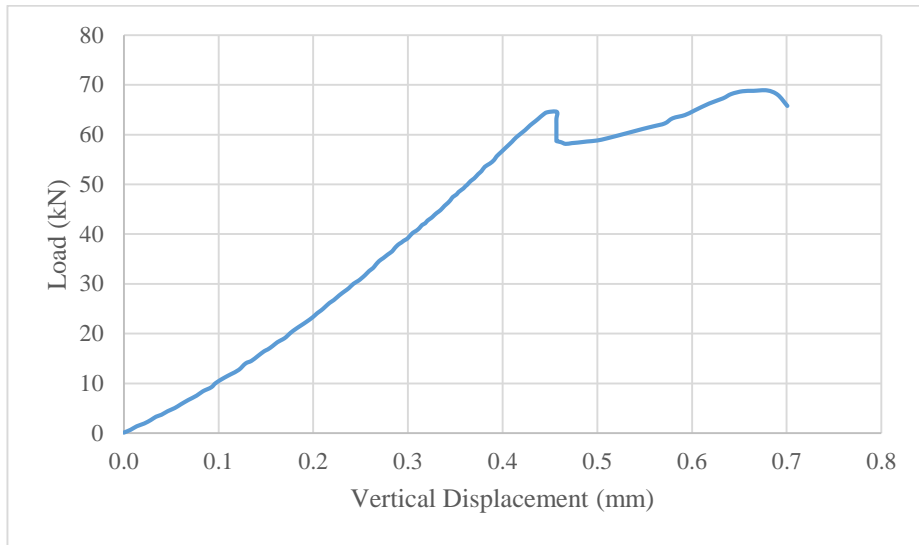
Figure D.21 Load-vertical displacement graph of C140-22_s5

Table D.14 Comparison of measured and calculated crack length of C140-22 coded- FBD sample

ID	a_{ce} (mm)	a_{ce}/R	$|a_{ce}-a_{cn}|$ (mm)	$|a_{ce}/R-a_{cn}/R|$
C140-22_s1	51.74	0.739	1.25	0.018
C140-22_s2	52.95	0.756	2.46	0.035
C140-22_s3	53.69	0.767	3.20	0.046
C140-22_s4	51.27	0.732	0.78	0.011
C140-22_s5	52.26	0.747	1.77	0.025
Avg. ± Std. Dev.	*52.38±0.96*	*0.748±0.014*	*1.89±0.96*	*0.027±0.014*

(a) before test   (b) during test   (c) after test

Figure D.22 C140-26 coded - FBD sample before, during and after the test

Table D.15 P_{min} and K_{Ic} values of C140-26 coded shotcrete FBD samples

ID	P_{min} (kN)	K_{Ic} (MPa $\sqrt{m}$)
C140-26_s1	63.8	1.33
C140-26_s2	59.8	1.24
C140-26_s3	61.2	1.26
C140-26_s4	65.8	1.38
C140-26_s5	64.7	1.36
Avg. ± Std. Dev.	*63.1±2.5*	*1.31±0.06*
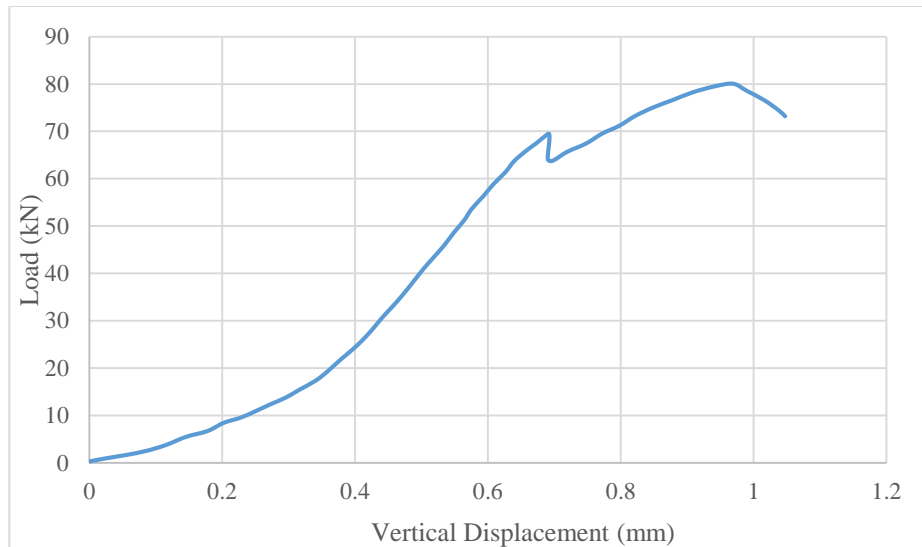
Figure D.23 Load-vertical displacement graph of C140-26_s1

Table D.16 Comparison of measured and calculated crack length of C140-26 coded- FBD sample

ID	a_{ce} (mm)	a_{ce}/R	$\lvert a_{ce}-a_{cn}\rvert$ (mm)	$\lvert a_{ce}/R-a_{cn}/R\rvert$
C140-26_s1	44.94	0.642	2.66	0.038
C140-26_s2	44.06	0.629	3.54	0.051
C140-26_s3	45.21	0.646	2.39	0.034
C140-26_s4	46.76	0.668	0.84	0.012
C140-26_s5	48.01	0.686	0.41	0.006
Avg. ± Std. Dev.	*45.80±1.57*	*0.654±0.022*	*1.97±1.31*	*0.028±0.019*

(a) before test   (b) during test   (c) after test
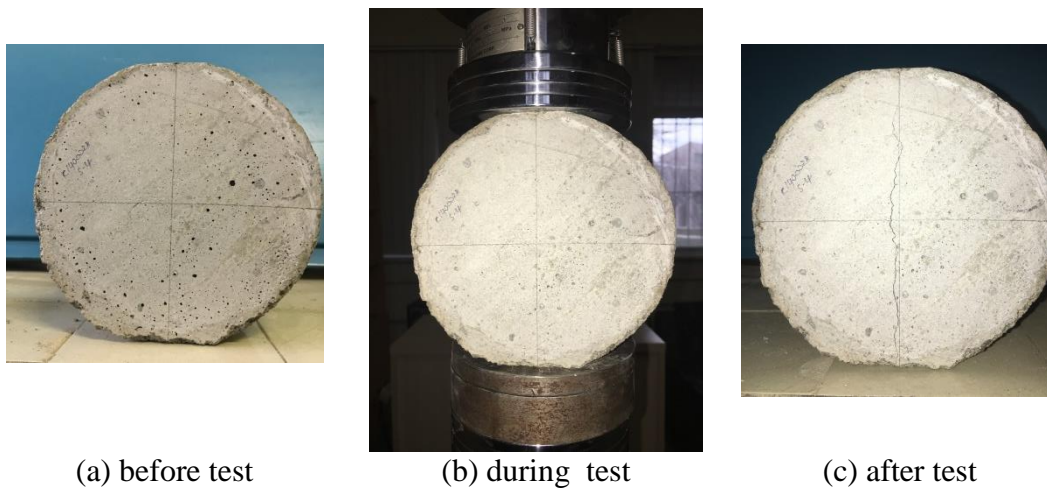
Figure D.24 C140-28 coded - FBD sample before, during and after the test

Table D.17 P_{min} *and* K_{Ic} *values of C140-28 coded shotcrete FBD samples*

ID	P_{min} (kN)	K_{Ic} (MPa $\sqrt{m}$)
C140-28_s1	65.2	1.26
C140-28_s2	63.4	1.23
C140-28_s3	63.8	1.22
C140-28_s4	61.4	1.20
C140-28_s5	64.7	1.27
Avg. ± Std. Dev.	*63.7±1.5*	*1.24±0.03*
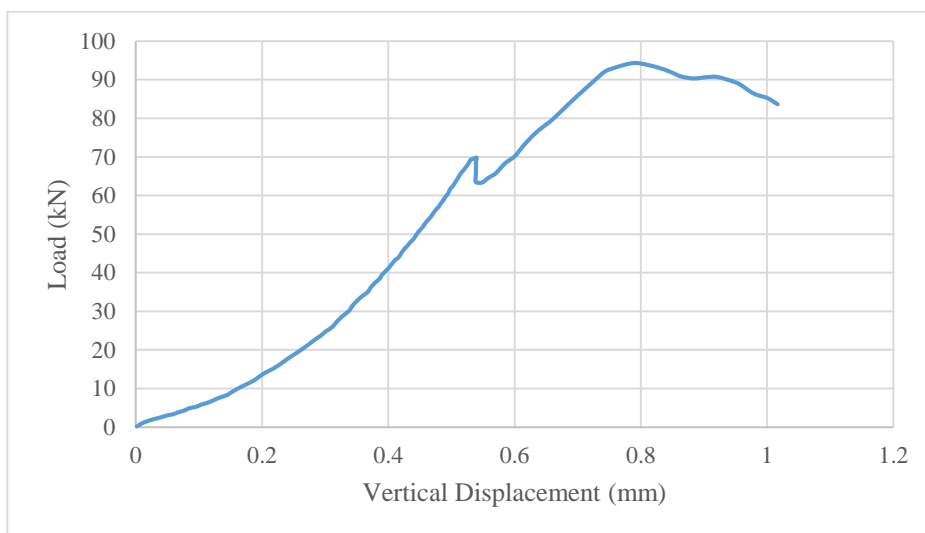
Figure D.25 Load-vertical displacement graph of **C140-28_s2**

Table D.18 Comparison of measured and calculated crack length of C140-28 coded- FBD sample

ID	a_{ce} (mm)	a_{ce}/R	$|a_{ce}-a_{cn}|$ (mm)	$|a_{ce}/R-a_{cn}/R|$
C140-28_s1	49.49	0.707	3.27	0.047
C140-28_s2	48.27	0.690	2.05	0.029
C140-28_s3	46.19	0.660	0.03	0.000
C140-28_s4	47.92	0.685	1.70	0.024
C140-28_s5	49.79	0.711	3.57	0.051
Avg. ± Std. Dev.	*48.33±1.43*	*0.690±0.020*	*2.12±1.41*	*0.030±0.020*

(a) before test (b) during test (c) after test
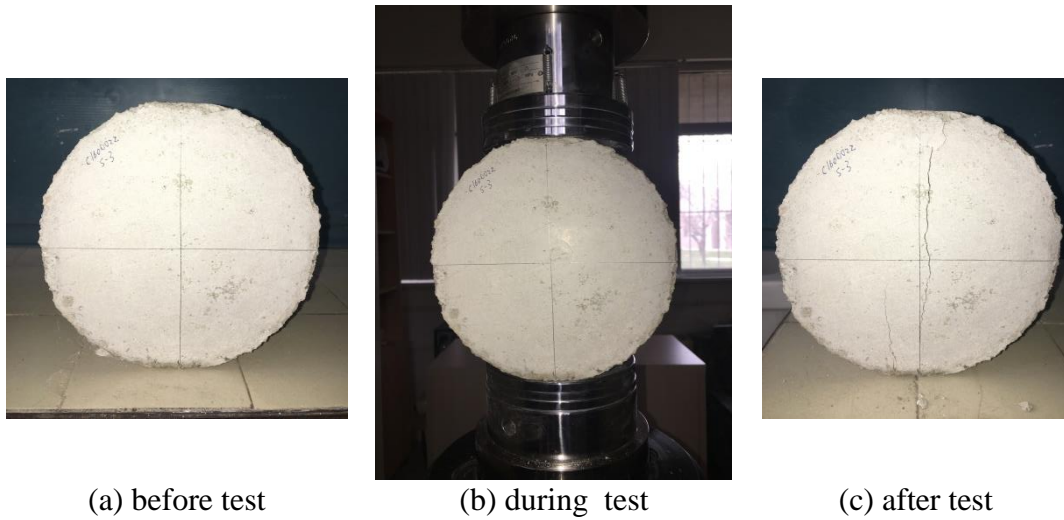
Figure D.26 C160-22 coded - FBD sample before, during and after the test

Table D.19 P_{min} and K_{Ic} values of C160-22 coded shotcrete FBD samples

ID	P_{min} (kN)	K_{Ic} (MPa $\sqrt{m}$)
C160-22_s1	68.4	1.40
C160-22_s2	70.8	1.44
C160-22_s3	67.1	1.36
C160-22_s4	69.3	1.41
C160-22_s5	72.1	1.47
Avg. ± Std. Dev.	*69.5±2.0*	*1.42±0.04*
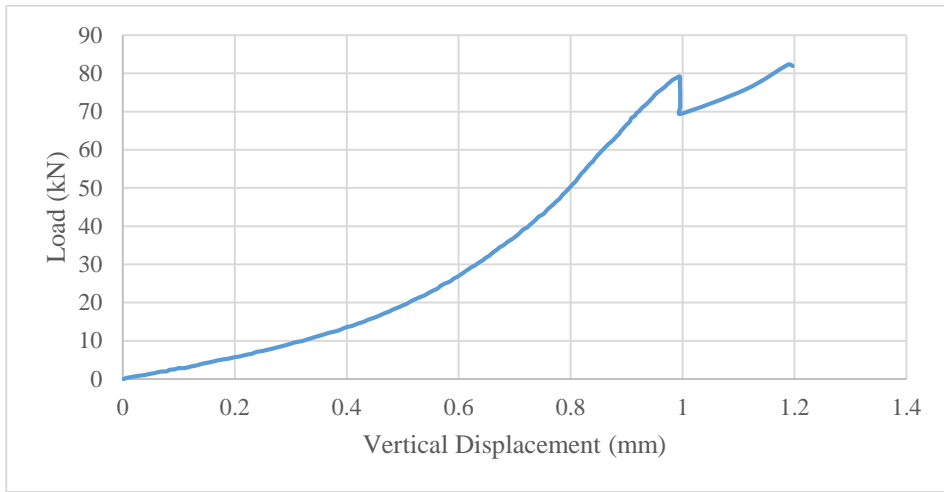
Figure D.27 Load-vertical displacement graph of C160-22_s4

Table D.20 Comparison of measured and calculated crack length of C160-22 coded- FBD sample

ID	a_{ce} (mm)	a_{ce}/R	$\|a_{ce}-a_{cn}\|$ (mm)	$\|a_{ce}/R-a_{cn}/R\|$
C160-22_s1	60.25	0.753	2.54	0.032
C160-22_s2	58.03	0.725	0.32	0.004
C160-22_s3	60.12	0.752	2.41	0.030
C160-22_s4	58.99	0.737	1.28	0.016
C160-22_s5	59.37	0.742	1.66	0.021
Avg. ± Std. Dev.	*59.35±0.90*	*0.742±0.011*	*1.65±0.90*	*0.021±0.011*

(a) before test   (b) during test   (c) after test

Figure D.28 C160-24 coded - FBD sample before, during, and after the test

Table D.21 P_{min} *and* K_{Ic} *values of C160-24 coded shotcrete FBD samples*

ID	P_{min} (kN)	K_{Ic} (MPa $\sqrt{m}$)
C160-24_s1	69.1	1.32
C160-24_s2	73.4	1.39
C160-24_s3	73.9	1.40
C160-24_s4	71.3	1.35
C160-24_s5	76.2	1.44
Avg. ± Std. Dev.	*72.8±2.7*	*1.38±0.05*
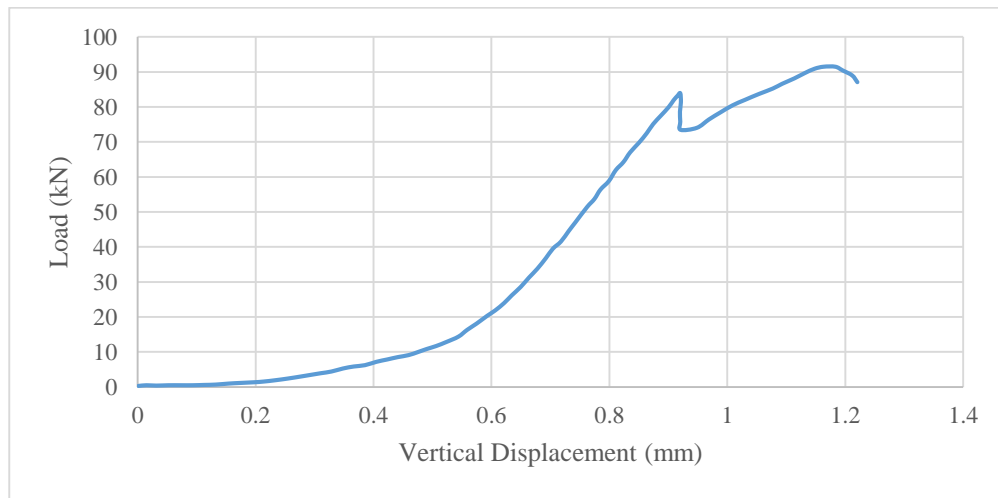
Figure D.29 Force-displacement graph of **C160-24_s2**

Table D.22 Comparison of measured and calculated crack length of C160-24 coded- FBD sample

ID	a_{ce} (mm)	a_{ce}/R	$|a_{ce}-a_{cn}|$ (mm)	$|a_{ce}/R-a_{cn}/R|$
C160-24_s1	53.56	0.670	2.47	0.031
C160-24_s2	54.19	0.677	1.84	0.023
C160-24_s3	54.44	0.681	1.59	0.020
C160-24_s4	57.85	0.723	1.82	0.023
C160-24_s5	55.12	0.689	0.91	0.011
Avg. ± Std. Dev.	*55.03±1.67*	*0.688±0.021*	*1.73±0.56*	*0.022±0.007*

(a) before test (b) during test (c) after test
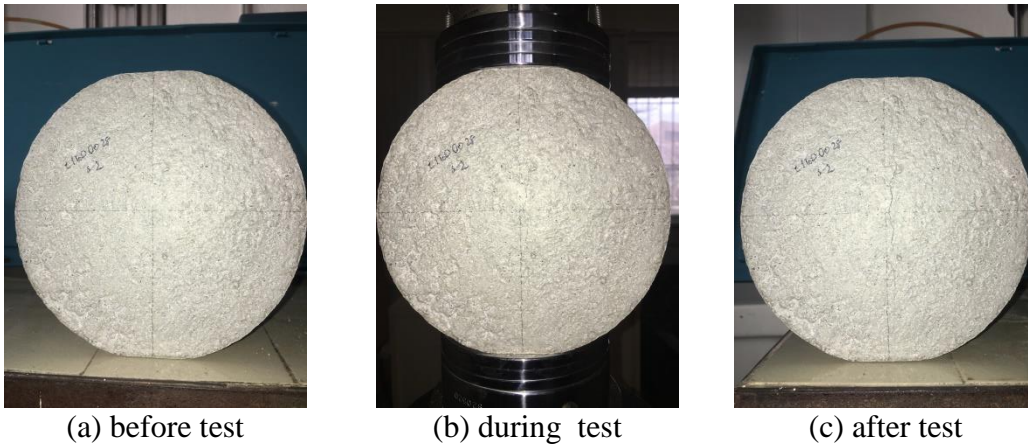
Figure D.30 C160-28 coded - FBD sample before, during and after the test

Table D.23 P_{min} *and* K_{Ic} *values of C160-28 coded shotcrete FBD samples*

ID	P_{min} (kN)	K_{Ic} (MPa $\sqrt{m}$)
C160-28_s1	80.9	1.31
C160-28_s2	82.3	1.35
C160-28_s3	81.5	1.31
C160-28_s4	79.4	1.28
C160-28_s5	83.1	1.34
Avg. ± Std. Dev.	*81.4±1.4*	*1.32±0.03*
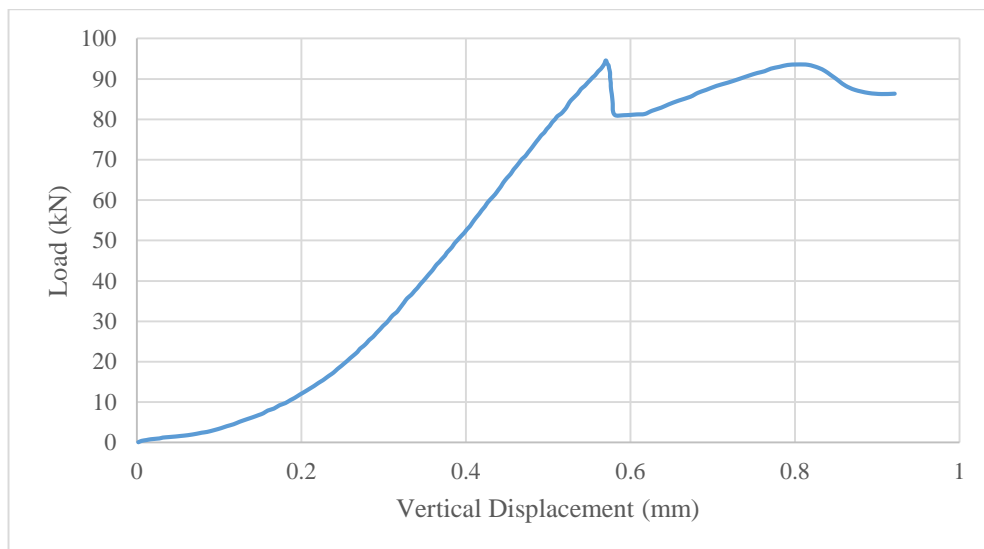
Figure D.31 Load-vertical displacement graph of C160-28_s1

150

Table D.24 Comparison of measured and calculated crack length of C160-28 coded- FBD sample

ID	a_{ce} (mm)	a_{ce}/R	$|a_{ce}-a_{cn}|$ (mm)	$|a_{ce}/R-a_{cn}/R|$
C160-28_s1	55.96	0.700	3.14	0.039
C160-28_s2	52.21	0.653	0.61	0.008
C160-28_s3	54.08	0.676	1.26	0.016
C160-28_s4	53.68	0.671	0.86	0.011
C160-28_s5	56.24	0.703	3.42	0.043
Avg. ± Std. Dev.	*54.43±1.68*	*0.680±0.021*	*1.86±1.32*	*0.023±0.017*

(a) before test   (b) during test   (c) after test
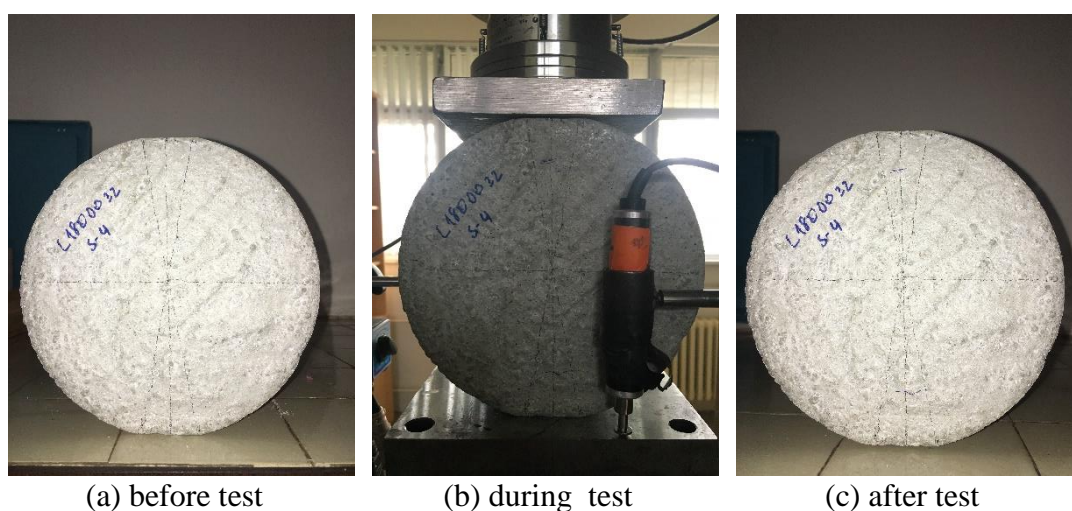
Figure D.32 C180-22 coded - FBD sample before, during and after the test

Table D.25 P_{min} and K_{Ic} values of C180-22 coded shotcrete FBD samples

ID	P_{min} (kN)	K_{Ic} (MPa $\sqrt{m}$)
C180-22_s1	84.2	1.41
C180-22_s2	86.8	1.46
C180-22_s3	87.6	1.47
C180-22_s4	91.5	1.53
C180-22_s5	84.3	1.41
Avg. ± Std. Dev.	*86.9±3.0*	*1.46±0.05*
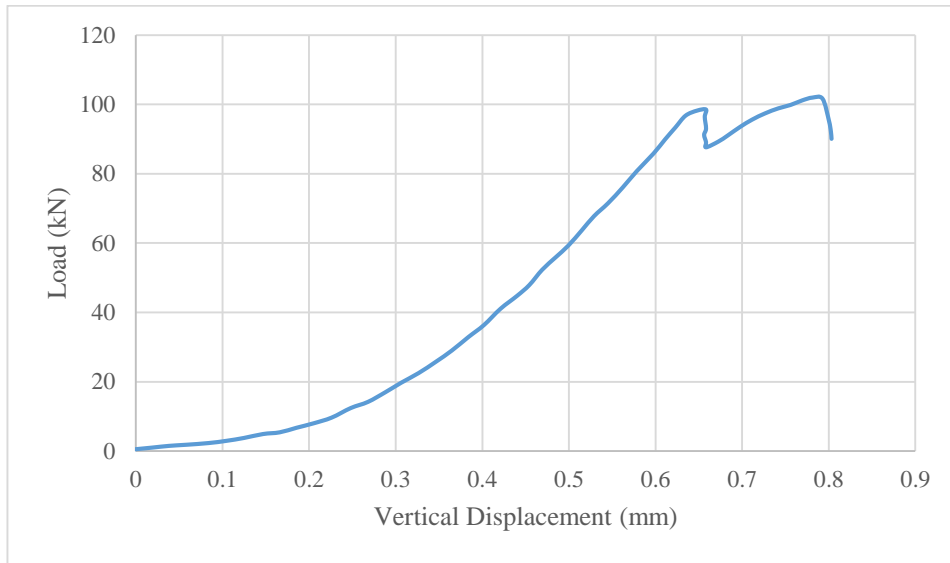
Figure D.33 Load-vertical displacement graph of C180-22_s3

Table D.26 Comparison of measured and calculated crack length of C180-22 coded- FBD sample

ID	a_{ce} (mm)	a_{ce}/R	$\|a_{ce}\text{-}a_{cn}\|$ (mm)	$\|a_{ce}/R\text{-}a_{cn}/R\|$
C180-22_s1	64.72	0.719	0.20	0.002
C180-22_s2	64.60	0.718	0.32	0.004
C180-22_s3	6473	0.719	0.19	0.002
C180-22_s4	67.65	0.752	2.73	0.030
C180-22_s5	68.50	0.761	3.58	0.040
Avg. ± Std. Dev.	*66.04±1.88*	*0.734±0.021*	*1.40±1.63*	*0.016±0.018*

(a) before test   (b) during test   (c) after test

Figure D.34 C180-28 coded - FBD sample before, during, and after the test

Table D.27 P$_{min}$ *and* K$_{Ic}$ *values of C180-28 coded shotcrete FBD samples*

ID	P_{min} (kN)	K_{Ic} (MPa $\sqrt{m}$)
C180-28_s1	102.3	1.38
C180-28_s2	100.9	1.36
C180-28_s3	101.5	1.37
C180-28_s4	100.7	1.36
C180-28_s5	102.9	1.39
Avg. ± Std. Dev.	*101.7±0.9*	*1.37±0.01*
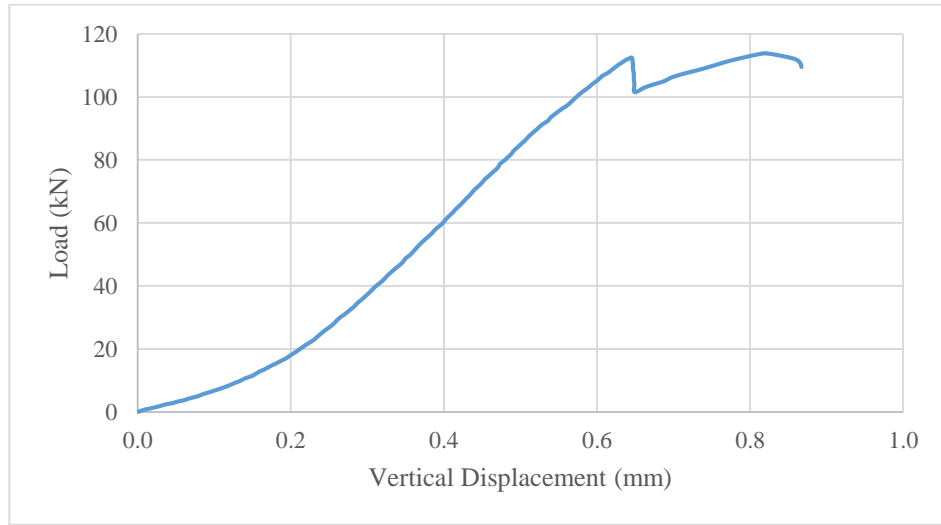
Figure D.35 Load-vertical displacement graph of C180-28_s3

Table D.28 Comparison of measured and calculated crack length of C180-28 coded- FBD sample

ID	a_{ce} (mm)	a_{ce}/R	$|a_{ce}\text{-}a_{cn}|$ (mm)	$|a_{ce}/R\text{-}a_{cn}/R|$
C180-28_s1	60.33	0.670	0.90	0.010
C180-28_s2	62.98	0.700	3.55	0.039
C180-28_s3	61.47	0.683	2.04	0.023
C180-28_s4	60.08	0.668	0.65	0.007
C180-28_s5	60.33	0.670	0.90	0.010
Avg. ± Std. Dev.	*61.04±1.21*	*0.678±0.013*	*1.61±1.21*	*0.018±0.013*

(a) before test	(b) during test	(c) after test
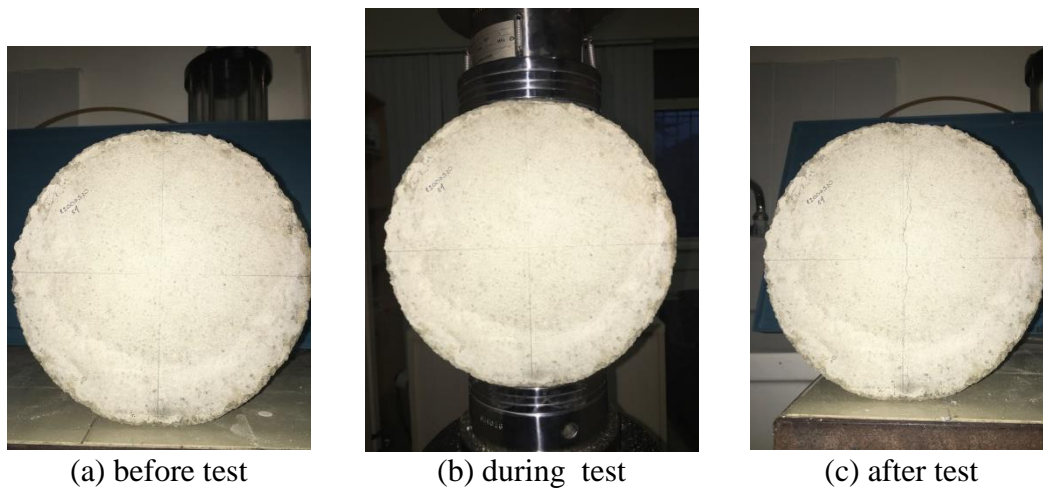
Figure D.36 C200-20 coded - FBD sample before, during, and after the test

Table D.29 P$_{min}$ and K$_{Ic}$ values of C200-20 coded shotcrete FBD samples

ID	P_{min} (kN)	K_{Ic} (MPa $\sqrt{m}$)
C200-20-s1	97.9	1.51
C200-20-s2	98.9	1.53
C200-20-s3	96.4	1.49
C200-20-s4	94.3	1.46
C200-20-s5	96.8	1.50
Avg. ± Std. Dev.	*96.9±1.7*	*1.50±0.03*
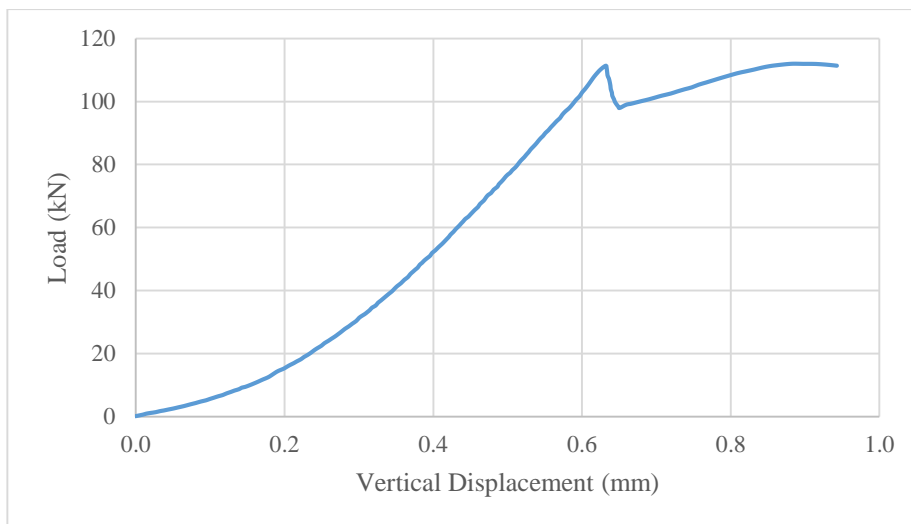
Figure D.37 Load-vertical displacement graph of C200-20_s1

154

Table D.30 Comparison of measured and calculated crack length of C200-20 coded- FBD sample

ID	a_{ce} (mm)	a_{ce}/R	$|a_{ce}-a_{cn}|$ (mm)	$|a_{ce}/R-a_{cn}/R|$
C200-20_s1	76.39	0.764	2.10	0.021
C200-20_s2	76.12	0.761	1.83	0.018
C200-20_s3	74.25	0.743	0.04	0.000
C200-20_s4	75.11	0.751	0.82	0.008
C200-20_s5	76.35	0.764	2.06	0.021
Avg. ± Std. Dev.	*75.64±0.94*	*0.756±0.009*	*1.37±0.91*	*0.014±0.009*

(a) before test   (b) during test   (c) after test
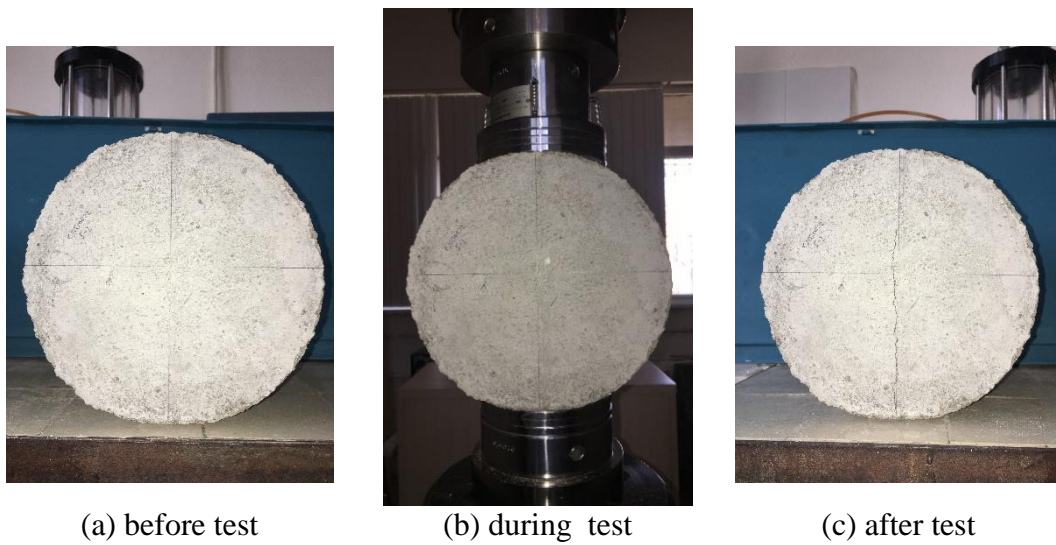
Figure D.38 C200-22 coded - FBD sample before, during and after the test

Table D.31 P_{min} *and* K_{Ic} *values of C200-22 coded shotcrete FBD samples*

ID	P_{min} (kN)	K_{Ic} (MPa $\sqrt{m}$)
C200-22_s1	104.7	1.50
C200-22_s2	105.4	1.51
C200-22_s3	102.1	1.47
C200-22_s4	101.5	1.46
C200-22_s5	102.8	1.48
Avg. ± Std. Dev.	*103.3±1.7*	*1.48±0.02*

Figure D.39 Load-vertical displacement graph of C200-22_s5

Table D.32 Comparison of measured and calculated crack length of C200-22 coded- FBD sample

ID	a_{ce} (mm)	a_{ce}/R	$\|a_{ce}-a_{cn}\|$ (mm)	$\|a_{ce}/R-a_{cn}/R\|$
C200-22_s1	72.16	0.722	0.03	0.000
C200-22_s2	74.25	0.743	2.12	0.021
C200-22_s3	73.02	0.730	0.89	0.009
C200-22_s4	74.59	0.746	2.46	0.025
C200-22_s5	72.81	0.728	0.68	0.007
Avg. ± Std. Dev.	**73.37±1.02**	**0.734±0.010**	**1.23±1.02**	**0.012±0.010**

156

E. FBD TEST PHOTOS

Figure E.40 Examples of the FBD samples with 75 mm diameter

Figure E.41 Examples of the FBD samples with 100 mm diameter

Figure E.42 Examples of the FBD samples with 120 mm diameter

Figure E.43 Examples of the FBD samples with 140 mm diameter

Figure E.44 Examples of the FBD samples with 160 mm diameter

Figure E.45 Examples of the FBD samples with 180 mm diameter
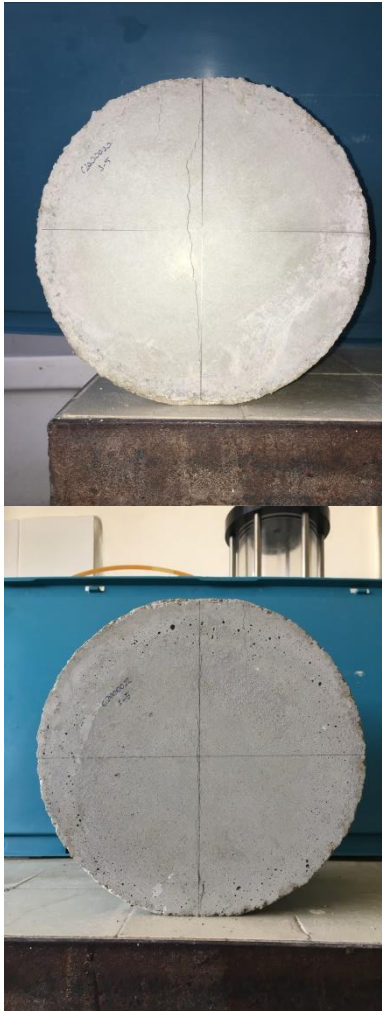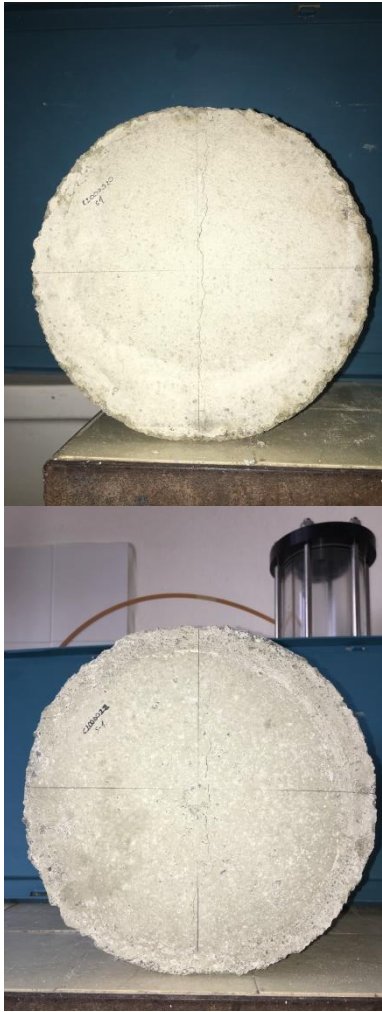
Figure E.46 Examples of the FBD samples with 200 mm diameter

Figure E.47 General view of the FBD test specimen

CURRICULUM VITAE

PERSONEL INFORMATION

Surname, Name: Yoncacı, Selin
Nationality: Turkish (TC)
Date and Place of Birth: 8 April 1983, Ankara
Phone: +90 537 588 39 07
e-mail: selinyon@gmail.com

EDUCATION

Degree	Institution	Year of Graduation
MS	METU, Mining Engineering	2009
BS	METU, Mining Engineering	2006
High School	Ankara Anadolu High School, Ankara	2001

WORK EXPERIENCE

Year	Place	Enrollment
2014-Present	Turkish Cement Manufacturers' Association	Head of the Physical and Mechanical Testing Laboratory
2008-2013	METU, Mining Engineering Department	Research Assistant

FOREIGN LANGUAGES

Advanced English, Basic German

PUBLICATIONS

1. Meral, Ç., Yoncacı, S., "Türkiye kömür yakıtlı termik santral uçucu külleri", 2019.

2. Yoncacı, S., "Assessment of the Compressive Strength Test Methods on Blended Cements", Cement & Concrete World, 23(131), 59-66 (2018).

3. Yoncacı, S., "Assessment of Water/Cement Ratio in the Compressive Strength Test on Blended Cements", Cement & Concrete World, 22(129), 86-93 (2017).

4. Yoncacı, S., Çetmeli M., Uysal, Ç., Türk, S., Şengün, E., " Eco-Efficient Cements: Potential, Economically Viable Solutions for a Low-CO2, Cement Based Materials Industry", Cement & Concrete World, 22(127), 81-89 (2017).

5. Yoncacı, S., "Recycling Construction Demolition Waste", Cement & Concrete World, 20(113), 85-90 (2015).

PARTICIPATED PROJECTS

1. Fostering Industrial Symbiosis for A Sustainable Resource Intensive Industry Across The Extended Construction Value Chain, European Union's Horizon 2020 research and innovation programme under grant agreement N° 642154, 2015-2020.

2. Metal Organic Frameworks for Carbon Dioxide Adsorption Processes In Power Production And Energy Intensive Industries, European Union's Horizon 2020 research and innovation programme under grant agreement N° 837975, 2019-2023.

3. Borlu Çimento Üretiminde Kolemanit Ara Ürünlerinin Kullanilabilirliğinin Araştirilmasi Ve Uygulanmasi, Eti Maden, 2019-2020.

4. Hümik Asitin Beton Kimyasal Katkısı Olarak Kullanılmasının Araştırılması, TKİ, 2018-2019.

5. Katkılı Çimentolarda Yapılan Basınç Dayanımı Deneyindeki Su/Çimento Oranının Değerlendirilmesi, Cyberpark Projesi: 00425_021, 2017-2018.

6. Kentsel Dönüşüm Atıklarının Yapı Malzemeleri Alanında Değerlendirilmesi, Cyberpark Projesi: 00425_025, 2019.

7. Silindirle Sıkıştırılmış Beton Yol Tasarım Çalışmalarında Agrega Gradasyonunun Etkisinin İncelenmesi, Cyberpark Projesi: 00425_028, 2019-2020.

8. Türkiye'de Kömür Yakıtlı Termik Santrallerden Elde Edilen Uçucu Küllerin Özellikleri ve Sınıflandırılması, Ankara, Türkiye, 2017

9. Türkiye'de Çimento Sektöründe Kullanılan Doğal Puzolanların Trasların Karakterizasyonu Genel Mineralojik Kompozisyonlarının ve Özelliklerinin Zeolit ve Feldispat Grubu Mineraller ile Camsı Faz İçeriklerinin Puzolanik Aktiviteyi Etkileyen Eşik Değerlerinin Belirlenmesi Bölüm 1 İç Anadolu Bölgesi Trasları, BAP NO: FUK-2015-6627, Ankara, Türkiye, 2015-2017

10. Adana Sivişli ve Şelale Yataklarının Ön Jeoteknik Parametrelerinin Belirlenmesi, Adana, Türkiye, Kasım 2011

11. Balıkesir- Kızıltepe Yatağı Projesi - Jeoteknik ve Sismik Aktivite Risk Raporu, Balıkesir, Türkiye, Mayıs 2011

12. ALKİM Beypazarı Yeraltı Soda İşletmesi Üretim Panolarının Duraylılığının Araştırılması, Aralık 2010

13. Konya İnlice Bölgesindeki Altın Madeni Arazisinde Yoğunluk Hesaplanması ve Arazideki Dağılımı Belirleme, Kasım 2010

14. Sanko Tekstil İşletmeleri Sanayi Ve Ticaret A.Ş' ye Ait Adı yaman Gölbaşı Linyit Sahası ile İlgili Fiziksel-Mekanik Deneyler ve Şev Stabilitesinin Araştırılması, Ağustos 2010

15. Kangal Etyemez Linyit Sahası İle İlgili Fiziksel-Mekanik Deneylerle, Kazı Şev Stabilitesi Analizlerinin Yapılarak Duraylılığının Araştırılması, Temmuz 2010

16. Afşin-Elbistan B Sahasında Akiferin Ocak Faaliyetlerine ve Şevlere Etkisinin ve Palplanş İstinat Yapısı Olanaklarının Araştırılması, Mart 2009

HOBBIES

Swimming, Pilates, Movies, Ice Skating